# Estimation of Code and Phase Biases in Satellite Navigation

Institute for Communications and Navigation

Technische Universität München

Prof. Dr. sc. nat. Christoph Günther

# Master Thesis

| | |
|---|---|
| Supervisor: | Dipl.-Ing. Patrick Henkel |
| Author: | Zhibo Wen |
| Started at: | 01.11.2009 |
| Completed at: | 03.05.2010 |

# Acknowledgement

First of all, I would like to thank my supervisor, Patrick Henkel, who gave me guidance and continuously support throughout the whole master thesis. It has been a great pleasure to work with Patrick, a knowledgeable, passionate and creative researcher. His serious attitudes towards scientific research and his hard working manner has set a wonderful model.

I would like to express my special thanks to Prof. Dr. Christoph Günther for giving me the opportunity to work on this project. His lectures on Satellite Navigation as well as Differential Navigation guided me into the area of navigation, which is very interesting and attractive, and I would like to continue working in this area after my thesis.

I would also like to thank the colleagues Kaspar Giger and Sebastian Knogl in the Institute for Communication and Navigation for the kind and helpful discussions. Kaspar also gave me precious suggestions and support on pre-processing of the raw data.

I would also like to thank my girlfriend Ke Jiang for her love, understanding and invaluable support in all respects. I am also grateful to all my friends for encouraging me during the thesis, especially Xiao Xu for providing me ideas on plotting ellipsoid.

Finally and most importantly, I would like to thank my parents Hongjuan Wang and Ganping Wen for their endless love and support.

# Contents

# 1 Introduction

Differential carrier phase positioning with double difference measurements over short base-lines strongly suppresses most error contributions, e.g. the ionospheric, tropospheric and orbital errors, as well as the biases of both receivers and satellites [1] [2] [3]. However, Zumberge et al. have shown in their paper on Precise Point Positioning [4] that the precise determination of the orbits and of the satellite clock offsets enabled a few millimeter daily precision in horizontal direction and a centimeter precision in vertical direction for the ground stations. Therefore, absolute carrier phase positioning has received a lot of attraction recently. Reliable integer ambiguity resolution and precise bias estimation are two challenges that are addressed in this work. These two estimation problems are coupled problems, i.e. the ambiguity resolution helps for the bias estimation and the bias estimation helps for the ambiguity resolution.

Henkel and Günther [5] proposed linear code carrier combinations that preserve the geometry, eliminate the ionospheric delays and maximize the ambiguity discrimination. In the case of Galileo E1, E5, E5a, E5b and E6 code and carrier phase measurements, a wavelength of 3.9 m and a noise level of a few centimeters for a carrier to noise power ratio of 45 dB/Hz was achieved. The model used for carrier and code phase measurements is given by

$$\begin{aligned}
\lambda_m \phi_{m,r}^k &= r_r^k + \delta r_r^k + c(\delta\tau_r - \delta\tau^k) - q_{1m}^2 I_r^k + T_r^k + \lambda_m N_{m,r}^k + b_{\phi_{m,r}^k} + \varepsilon_{m,r}^k, \\
\rho_{m,r}^k &= r_r^k + \delta r_r^k + c(\delta\tau_r - \delta\tau^k) + q_{1m}^2 I_r^k + T_r^k + b_{\rho_{m,r}^k} + \eta_{m,r}^k,
\end{aligned} \tag{1.1}$$

where $\lambda_m$ is the wavelength, $r_r^k$ denotes the user-satellite range, $\delta r_r^k$ denotes the projected orbital error, $c\delta\tau_r$ and $c\delta\tau^k$ are the user and satellite clock offsets, $I_r^k$ denotes the ionospheric delay on L1, $T_r^k$ denotes the tropospheric delay, $q_{1m}$ equals to the frequency ratio $f_1/f_m$, $N_{m,r}^k$ denotes the integer ambiguity, $b_{\phi_{m,r}^k}$ and $b_{\rho_{m,r}^k}$ represent the phase and code biases in units of meters, and $\varepsilon_{m,r}^k$, $\eta_{m,r}^k$ denote the phase and code noise for the $r$-th receiver, $k$-th satellite and $m$-th frequency.

The multi-frequency code carrier linear combination

$$\lambda\phi_r^k = \sum_{m=1}^{M}(\alpha_m\lambda_m\phi_{m,r}^k + \beta_m\rho_{m,r}^k), \tag{1.2}$$

can be chosen such that the geometry is preserved (GP), the ionosphere is eliminated (IF) and the integer ambiguities are preserved (NP), i.e.

$$\sum_{m=1}^{M}(\alpha_m + \beta_m) = 1,$$
$$\sum_{m=1}^{M}(\alpha_m - \beta_m)q_{1m}^2 = 0,$$
$$\alpha_m = \frac{j_m\lambda}{\lambda_m}, \quad \text{with} \quad j_m \in \mathbb{Z}, \quad \forall m, \tag{1.3}$$

which simplifies Eq. (1.2) to

$$\lambda\phi_r^k = r_r^k + \delta r_r^k + c(\delta\tau_r - \delta\tau^k) + \sum_{m=1}^{M}\alpha_m\lambda_m N_{m,r}^k + \sum_{m=1}^{M}\left(\alpha_m b_{\phi_{m,r}^k} + \beta_m b_{\rho_{m,r}^k}\right) +$$
$$+ \sum_{m=1}^{M}\left(\alpha_m\varepsilon_{m,r}^k + \beta_m\eta_{m,r}^k\right). \tag{1.4}$$

a fourth constraint is set on the combination to maximize the ambiguity discrimination:

$$D \triangleq \max_{\substack{\alpha_m, \forall m \\ \beta_m, \forall m}} \frac{\lambda(\alpha_1, \ldots, \alpha_M, \beta_1, \ldots, \beta_M)}{2\sigma_n(\alpha_1, \ldots, \alpha_M, \beta_1, \ldots, \beta_M)}, \quad \text{with} \ \sigma_n = \sqrt{\sum_{m=1}^{M}\alpha_m^2\sigma_{\phi_m}^2 + \sum_{m=1}^{M}\beta_m^2\sigma_{\rho_m}^2}.$$
$$\tag{1.5}$$

Thus, the coefficients $\alpha_m$ and $\beta_m$ can be determined uniquely for a given set of $j_m$. The bias in the combination of measurements has an upper bound:

$$\sum_{m=1}^{M}\left(\alpha_m b_{\phi_{m,r}^k} + \beta_m b_{\rho_{m,r}^k}\right) \leq \sum_{m=1}^{M}\left(|\alpha_m| \cdot |b_{\phi_{m,r}^k}| + |\beta_m| \cdot |b_{\rho_{m,r}^k}|\right). \tag{1.6}$$

Once the biases $b_{\phi_{m,r}^k}$ and $b_{\rho_{m,r}^k}$ are determined, the worst-case combination biases in the multi-frequency linear combination Eq. (1.2) can be substantially reduced.

In this work, the receiver and satellite biases on multiple frequencies are estimated with a Kalman filter. Chapter 2 introduces the general measurement model of the work, and performs a set of parameter mappings to remove the rank deficiency of the system of equations. Chapter 3 explains the principles of a Kalman filter, and its application for

the estimation of the receiver and satellite code and phase biases including the sequential resolution of the integer ambiguities with integer decorrelation. Some simulation results for Galileo are also presented in this chapter. Chapter 4 introduces two methods on how to estimate the grid ionospheric vertical delays and code biases, i.e. the interpolation of grid points and the least-squares fitting. Chapter 5 focuses on the analysis of the bias estimates from the GPS measurements. Two sets of real data are used in this work, the SAPOS data in Germany and the data from CORS in USA. The former is used to validate the phase bias estimates, while the latter is used to validate the grid ionospheric vertical delays and satellite code biases. It is noted that the estimation method does not depend on the data set that has been used, i.e. the data from CORS could also be used to estimate the phase biases and the SAPOS data for the estimation of the ionospheric grid and code biases.

# 2 Measurement Model and Parameter Mapping

## 2.1 Measurement Model

Reliable ambiguity resolution for absolute precise point positioning requires the precise estimation of phase and code biases on each frequency. These biases could be determined from measurements on multiple frequencies and a network of distributed reference stations. The most general model shall be used for measurements of undifferenced code and carrier phases on frequency $m$, receiver $r$, satellite $k$, and epoch $t_n$ (Henkel et al. [6] [7]):

$$
\begin{aligned}
\lambda_1 \phi_{1,r}^k(t_n) &= g_r^k(t_n) - I_{1,r}^k(t_n) + \lambda_1 N_{1,r}^k + \beta_{1,r} + \beta_1^k + p_1^k(t_n) + \varepsilon_{1,r}^k(t_n) \\
\lambda_2 \phi_{2,r}^k(t_n) &= g_r^k(t_n) - q_{12}^2 I_{1,r}^k(t_n) + \lambda_2 N_{2,r}^k + \beta_{2,r} + \beta_2^k + p_2^k(t_n) + \varepsilon_{2,r}^k(t_n) \\
\rho_{1,r}^k(t_n) &= g_r^k(t_n) + I_{1,r}^k(t_n) + b_{1,r} + b_1^k + \eta_{1,r}^k(t_n) \\
\rho_{2,r}^k(t_n) &= g_r^k(t_n) + q_{12}^2 I_{1,r}^k(t_n) + b_{2,r} + b_2^k + \eta_{2,r}^k(t_n),
\end{aligned} \tag{2.1}
$$

where:

| | |
|---|---|
| $\lambda_m \phi_{m,r}^k$: | carrier phase measurement, |
| $\rho_{m,r}^k$: | code measurement, |
| $g_r^k$: | range including clock errors and tropospheric zenith delays, |
| $I_{m,r}^k$: | ionospheric slant delay, |
| $N_{m,r}^k$: | integer ambiguity, |
| $\beta_{m,r}$: | receiver phase bias, |
| $\beta_m^k$: | satellite phase bias, |
| $b_{m,r}$: | receiver code bias, |
| $b_m^k$: | satellite code bias, |
| $p_m^k$: | satellite antenna phase center variation, |
| $\varepsilon_{m,r}^k$: | phase noise, |

$\eta_{m,r}^k$:          code noise,

and multipath errors are included in the phase and code noise.

A dynamic model is used for the range term $g_r^k(t_n)$, whose first order derivative over time has some process noise on top of a constant initial value. $g_r^k(t_n)$ can be further split into the range $r_r^k$, the clock offsets $c\delta\tau_r$ and $c\delta\tau^k$, and the tropospheric delay $T_r^k(t_n)$, i.e.

$$
\begin{aligned}
g_r^k(t_n) &= g_r^k(t_{n-1}) + \Delta t \cdot \dot{g}_r^k(t_{n-1}) + w_{g_r^k}(t_n) \\
&= r_r^k(t_n) + c \cdot (\delta\tau_r(t_n) - \delta\tau^k) + T_r^k(t_n),
\end{aligned} \tag{2.2}
$$

where $w_{g_r^k}(t_n)$ denotes the process noise to model accelerations.

The ionospheric slant delay $I_{1,r}^k$ is modeled as

$$
I_{1,r}^k(t_n) = m_{\mathrm{I}}(E_r^k(t_n)) \cdot I_{\mathrm{v},r}^k(t_n), \tag{2.3}
$$

where $m_{\mathrm{I}}(E_r^k(t_n))$ is the ionospheric mapping function between the slant and vertical delays. It depends on the elevation angle $E_r^k(t_n)$ from receiver $r$ to satellite $k$ at epoch $t_n$:

$$
m_{\mathrm{I}}(E_r^k(t_n)) = \frac{1}{\sqrt{1 - \frac{\cos^2(E_r^k(t_n))}{(1+h/R_{\mathrm{e}})^2}}}, \tag{2.4}
$$

with the radius $R_{\mathrm{e}}$ of the earth and the height $h$ of the ionospheric shell above the ground.

As shown in Eq. (2.1), the carrier phase measurements are affected by the time-variant satellite antenna phase center variations (PCVs) $p_m^k(t_n)$, which are caused by phase center offsets $l_{\mathrm{x},m}$ and $l_{\mathrm{y},m}$. To well explain the relationships between phase center variations and phase center offsets, we set up a satellite-fixed coordinate system with the y-axis corresponding to the rotation axis of the satellite solar panel, the z-axis pointing towards the center of the earth, and the x-axis completing the right-hand system (Schmid et al. [8]). Fig. 2.1 shows the three-dimensional coordinate system with the satellite antenna original phase center being the origin.

The satellite phase center variations consist of two components: azimuth-dependent PCVs and nadir-dependent PCVs, which are shown in Fig. 2.2.

The horizontal offsets $l_{\mathrm{xy},m}$, which also show up as azimuth-dependent PCVs, could be solved according to the right triangle $\Delta OAB$ in the left subfigure given the azimuth angle $\alpha$ of the projected receiver in xy plane and the azimuth angle $\alpha_{\Delta_m}$ of the shifted phase center

$$
l_{\mathrm{xy},m}(\alpha) = \sqrt{l_{\mathrm{x},m}^2 + l_{\mathrm{y},m}^2} \cdot \cos(\alpha_{\Delta_m} - \alpha), \tag{2.5}
$$
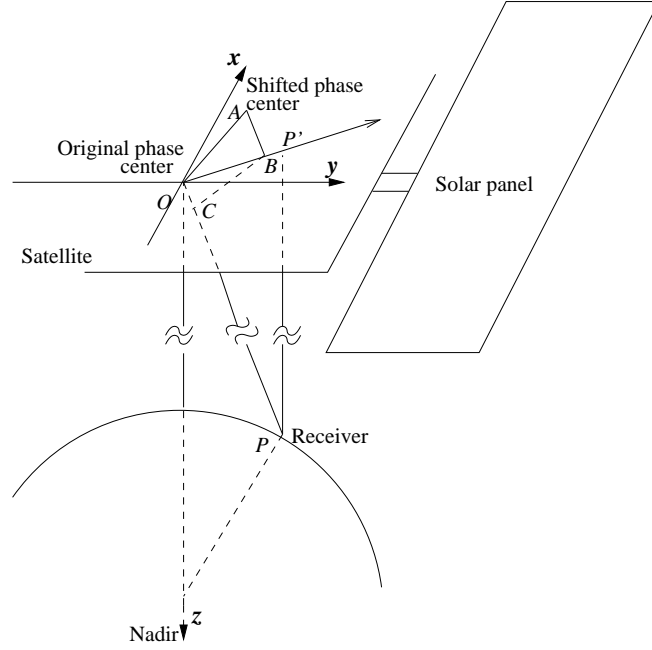
Fig. 2.1: The satellite-fixed coordinate system for expressing the satellite antenna phase center variation. For better view of xy plane, the satellite and the earth are not shown in the same scale.
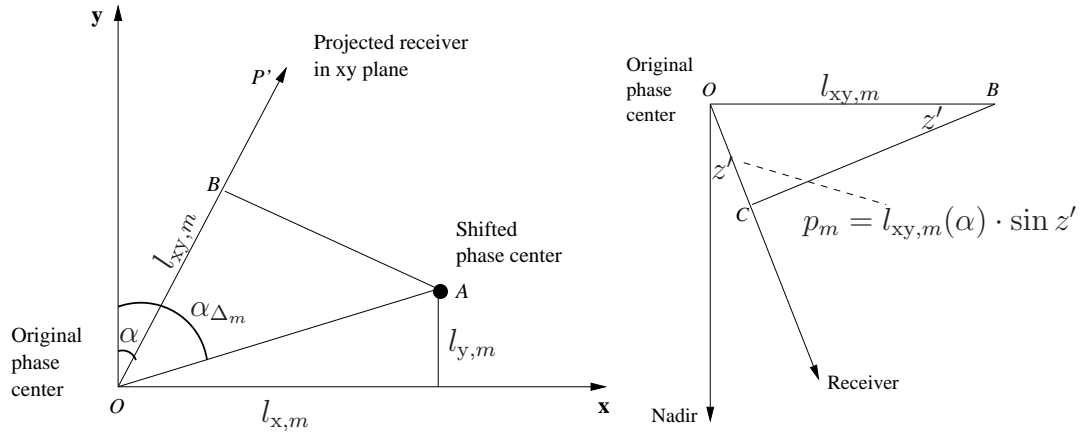


Fig. 2.2: Relationship between azimuth-dependent PCVs and nadir-dependent PCVs.

which has a maximum value when the shifted phase center is in the direction of the projected receiver, i.e. $\alpha_{\Delta_m} = \alpha$.

In the right subfigure the nadir-dependent PCVs is determined inside the right triangle $\triangle OBC$, and thus, the combined effect of phase center variations is given as follows:

$$p_m^k(z'(t_n), \alpha(t_n)) = \sqrt{l_{x,m}^2 + l_{y,m}^2} \cdot \sin z'(t_n) \cdot \cos\left(\arctan\frac{l_{x,m}}{l_{y,m}} - \alpha(t_n)\right), \qquad (2.6)$$

where the nadir angle $z'$ and the azimuth $\alpha$ are time-dependent as the geometry between the satellite and the receiver changes.

In order to get the horizontal offsets errors, Schmid et al. have suggested a fitting of the azimuth-dependent PCVs $p_m^k(z'_0, \alpha(t_n))$ for a fixed nadir angle $z'_0$ to the cosine function,

$$f(\alpha) = A_m \cdot \cos(\alpha_{\Delta_m} - \alpha), \tag{2.7}$$

with the amplitude $A_m$ and the phase shift $\alpha_{\Delta_m}$. Thus, the horizontal offsets to be compensated for with reversed sign are obtained from

$$
\begin{aligned}
l_{\mathrm{x},m} &= \frac{A_m}{\sin(z'_0)} \cdot \sin \alpha_{\Delta_m} \\
l_{\mathrm{y},m} &= \frac{A_m}{\sin(z'_0)} \cdot \cos \alpha_{\Delta_m}.
\end{aligned}
\tag{2.8}
$$

The satellite antenna phase center variations are observed to be in a few millimeter level (see e.g. Schmid et al. [8]), which is ignorable compared to the estimated bias term. Therefore, the phase center variations are not considered in the measurement model for estimation of biases in this work.

The phase and code noise is assumed to be zero mean white Gaussian distributed, with the standard deviation $\sigma_{\rho_{m,r}^k}$ of the code tracking error has been set to the Cramer Rao bound which is given by

$$\Gamma_m = \frac{c}{\sqrt{\frac{E_{\mathrm{s}}}{N_0} \cdot \frac{\int (2\pi f)^2 |S_m(f)|^2 df}{\int |S_m(f)|^2 df}}}, \tag{2.9}$$

with the speed of light c, the signal to noise power ratio $\frac{E_{\mathrm{s}}}{N_0}$, and the power spectral density $S_m(f)$ that has been derived by Betz [11] for binary offset carrier (BOC) modulated signals. Table 2.1 shows the Cramer Rao bound for the most important Galileo signals at a signal to noise power ratio of 45dB (Henkel et al. [12]). The standard deviation of the phase noise has been assumed to be 1 mm.

Table 2.1: Cramer Rao Bounds for $E_{\mathrm{s}}/N_0 = 45$dB

|      | Signal        | BW [MHz] | $\Gamma$ [cm] |
|------|---------------|----------|---------------|
| E1   | MBOC          | 20       | 11.14         |
| E5   | AltBOC(15,10) | 51       | 1.95          |
| E5a  | BPSK(10)      | 20       | 7.83          |
| E5b  | BPSK(10)      | 20       | 7.83          |

## 2.2   Estimation of Single Difference Phase Biases with Melbourne-Wübbena Combination

Ge et al. [9], and Gabor and Nerem [10] have proposed a method to estimate L1 and L2 satellite-satellite single difference (SD) phase biases. Two kinds of linear combinations of measurements have been used, and the derivation is briefly explained here. This approach has the disadvantage that the obtained bias estimates are only applicable to narrowlane ionosphere-free linear combination with a wavelength of at most 10.7 cm.

First, the geometry-free, ionosphere-free Melbourne-Wübbena combination [13] is introduced as

$$
\left( \frac{f_1}{f_1 - f_2} \lambda_1 \Delta \phi_{1,r}^{kl} - \frac{f_2}{f_1 - f_2} \lambda_2 \Delta \phi_{2,r}^{kl} \right) - \left( \frac{f_1}{f_1 + f_2} \Delta \rho_{1,r}^{kl} + \frac{f_2}{f_1 + f_2} \Delta \rho_{2,r}^{kl} \right) = \lambda_{\mathrm{w}} \Delta b_{\mathrm{w},r}^{kl} + \Delta \varepsilon_{\mathrm{w},r}^{kl},
$$

(2.10)

with

$$
\lambda_{\mathrm{w}} = \frac{1}{\frac{1}{\lambda_1} - \frac{1}{\lambda_2}} = \frac{f_1 \cdot \lambda_1}{f_1 - f_2},
$$

(2.11)

where $\lambda_m \Delta \phi_{m,r}^{kl}$ and $\Delta \rho_{m,r}^{kl}$ are the SD carrier phase and code measurements on frequency $f_m$, $m = \{1, 2\}$, $\lambda_{\mathrm{w}}$ is the widelane wavelength, $\Delta \varepsilon_{\mathrm{w},r}^{kl}$ denotes the combined phase and code noise. The combined integer ambiguity/bias term $\Delta b_{\mathrm{w},r}^{kl}$ is obtained from (2.10) as

$$
\Delta b_{\mathrm{w},r}^{kl} = \Delta N_{1,r}^{kl} - \Delta N_{2,r}^{kl} + \Delta \beta_1^{kl} - \Delta \beta_2^{kl} - \frac{f_1 - f_2}{f_1 + f_2} \cdot \frac{\Delta b_1^{kl}}{\lambda_1} - \frac{f_1 - f_2}{f_1 + f_2} \cdot \frac{\Delta b_2^{kl}}{\lambda_2}.
$$

(2.12)

In the next step, the geometry-preserving, ionosphere-free phase only combination is introduced as

$$
\frac{f_1^2}{f_1^2 - f_2^2} \lambda_1 \Delta \phi_{1,r}^{kl} - \frac{f_2^2}{f_1^2 - f_2^2} \lambda_2 \Delta \phi_{2,r}^{kl} = \Delta g_r^{kl} + \Delta b_{c,r}^{kl} + \Delta \varepsilon_{c,r}^{kl},
$$

(2.13)

with the combined ambiguity/bias term

$$
\Delta b_{c,r}^{kl} = \frac{f_1^2}{f_1^2 - f_2^2} \cdot \lambda_1 (\Delta N_{1,r}^{kl} + \Delta \beta_1^{kl}) - \frac{f_2^2}{f_1^2 - f_2^2} \cdot \lambda_2 (\Delta N_{2,r}^{kl} + \Delta \beta_2^{kl}).
$$

(2.14)

In order to get the ambiguities and phase biases on a single frequency, the above two combinations are combined with certain pre-factors, i.e.

$$
\begin{aligned}
\frac{f_1 + f_2}{c} \cdot \Delta b_{c,r}^{kl} - \frac{f_2}{f_1 - f_2} \cdot \Delta b_{\mathrm{w},r}^{kl} &= \Delta N_{1,r}^{kl} + \Delta \tilde{\beta}_1^{kl}, \\
\frac{f_1 + f_2}{c} \cdot \Delta b_{c,r}^{kl} - \frac{f_1}{f_1 - f_2} \cdot \Delta b_{\mathrm{w},r}^{kl} &= \Delta N_{2,r}^{kl} + \Delta \tilde{\beta}_2^{kl},
\end{aligned}
$$

(2.15)

with

$$
\begin{aligned}
\Delta\tilde{\beta}_1^{kl} &= \Delta\beta_1^{kl} + \frac{f_2}{f_1+f_2}\cdot\frac{\Delta b_1^{kl}}{\lambda_1} + \frac{f_2}{f_1+f_2}\cdot\frac{\Delta b_2^{kl}}{\lambda_2}, \\
\Delta\tilde{\beta}_2^{kl} &= \Delta\beta_2^{kl} + \frac{f_1}{f_1+f_2}\cdot\frac{\Delta b_1^{kl}}{\lambda_1} + \frac{f_1}{f_1+f_2}\cdot\frac{\Delta b_2^{kl}}{\lambda_2}.
\end{aligned} \tag{2.16}
$$

The transmission of the estimated combined phase and code biases $\Delta\tilde{\beta}_1^{kl}$ and $\Delta\tilde{\beta}_2^{kl}$ enables unbiased SD integer ambiguity resolution. However, these biases can only be applied to linear combination of the form

$$
\alpha_1\cdot\left(\lambda_1\Delta\phi_1^{kl} + \frac{f_2}{f_1+f_2}\Delta\rho_1^{kl} + \frac{f_2\lambda_1}{f_1+f_2}\frac{\Delta\rho_2^{kl}}{\lambda_2}\right) + \alpha_2\cdot\left(\lambda_2\Delta\phi_2^{kl} + \frac{f_1\lambda_2}{f_1+f_2}\frac{\Delta\rho_1^{kl}}{\lambda_1} + \frac{f_1}{f_1+f_2}\Delta\rho_2^{kl}\right),
$$

which is ionosphere-free no matter which value $\alpha_1$ and $\alpha_2$ have. Typically, geometry-preserving and integer-preserving constraints are imposed for positioning, i.e.

$$
\alpha_1\frac{f_1+f_2}{f_1} + \alpha_2\frac{f_1+f_2}{f_2} = 1, \tag{2.17}
$$

$$
\alpha_1 = \frac{j_1\lambda}{\lambda_1} \quad\text{and}\quad \alpha_2 = \frac{j_2\lambda}{\lambda_2} \quad\text{with}\quad \{j_1,j_2\} \stackrel{!}{\in} \mathbb{Z}. \tag{2.18}
$$

Therefore, the wavelength of this linear combination follows as

$$
\lambda = \frac{1}{j_1+j_2}\frac{c}{f_1+f_2} \leq \frac{f_1}{f_1+f_2}\lambda_1, \tag{2.19}
$$

which means the bias terms of (2.16) and (2.16) are only applicable to a certain form of linear combination, i.e. combinations with a narrowlane wavelength of at most 10.7 cm.

The next subsection will focus on how to map some parameters together, in order to solve the system of equations (2.1) so that the previous shortcomings can be overcome and undifferenced phase and code biases can be estimated.

## 2.3   Parameter Mapping

The estimation of ambiguities and all biases in Eq. (2.1) is not feasible but also not required as some biases can not be separated from the remaining parameters. Therefore, some biases are absorbed by other parameters, which are then estimated jointly. Additionally, the parameter mapping provides also a large benefit for the integer ambiguity resolution.

In a first step, the receiver and satellite code biases on two frequencies are mapped to the ranges and ionospheric delays as follows:

$$
\begin{aligned}
\rho_{1,r}^k(t_n) &= g_r^k(t_n) + q_{11}^2 I_r^k(t_n) + b_{1,r} + b_1^k + \eta_{1,r}^k(t_n) \\
&= \underbrace{\left(g_r^k(t_n) + b_{g_r} + b_{g^k}\right)}_{\tilde{g}_r^k(t_n)} + q_{11}^2 \underbrace{\left(I_r^k(t_n) + b_{I_r} + b_{I^k}\right)}_{\tilde{I}_r^k(t_n)} + \eta_{1,r}^k(t_n),
\end{aligned}
\tag{2.20}
$$

and

$$
\begin{aligned}
\rho_{2,r}^k(t_n) &= g_r^k(t_n) + q_{12}^2 I_r^k(t_n) + b_{2,r} + b_2^k + \eta_{2,r}^k(t_n) \\
&= \underbrace{\left(g_r^k(t_n) + b_{g_r} + b_{g^k}\right)}_{\tilde{g}_r^k(t_n)} + q_{12}^2 \underbrace{\left(I_r^k(t_n) + b_{I_r} + b_{I^k}\right)}_{\tilde{I}_r^k(t_n)} + \eta_{2,r}^k(t_n),
\end{aligned}
\tag{2.21}
$$

with $q_{11}^2 = 1$.

If measurements on an additional third frequency are included, the biases of the code measurements have to be estimated as the ranges and ionospheric delays already absorbed the code biases on the first two frequencies. The biases $b_{g_r}$ and $b_{I_r}$ are the receiver code biases which are, respectively, mapped to ranges and ionospheric delays. Similarly, the satellite code biases are split into $b_{g^k}$ and $b_{I^k}$.

$$
\begin{aligned}
b_{g_r} + q_{11}^2 b_{I_r} &= b_{1,r} \\
b_{g_r} + q_{12}^2 b_{I_r} &= b_{2,r} \\
b_{g^k} + q_{11}^2 b_{I^k} &= b_{1,k} \\
b_{g^k} + q_{12}^2 b_{I^k} &= b_{2,k},
\end{aligned}
\tag{2.22}
$$

which could be solved for the combined biases, i.e.

$$
\begin{aligned}
b_{g_r} &= -\frac{b_{2,r} - q_{12}^2 b_{1,r}}{q_{12}^2 - 1}, & b_{I_r} &= -\frac{b_{1,r} - b_{2,r}}{q_{12}^2 - 1} \\
b_{g^k} &= -\frac{b_2^k - q_{12}^2 b_1^k}{q_{12}^2 - 1}, & b_{I^k} &= -\frac{b_1^k - b_2^k}{q_{12}^2 - 1}.
\end{aligned}
\tag{2.23}
$$

The mapping of code biases also affects the carrier phase measurements, so the phase biases are changed correspondingly in order to compensate for the additional term combined in ranges and ionospheric delays, i.e.

$$
\begin{aligned}
\lambda_1 \phi_{1,r}^k(t_n) &= \tilde{g}_r^k(t_n) - q_{11}^2 \tilde{I}_{1,r}^k(t_n) + \lambda_1 N_{1,r}^k + \tilde{\beta}_{1,r} + \tilde{\beta}_1^k + \varepsilon_{1,r}^k(t_n) \\
\lambda_2 \phi_{2,r}^k(t_n) &= \tilde{g}_r^k(t_n) - q_{12}^2 \tilde{I}_{1,r}^k(t_n) + \lambda_2 N_{2,r}^k + \tilde{\beta}_{2,r} + \tilde{\beta}_2^k + \varepsilon_{2,r}^k(t_n),
\end{aligned}
\tag{2.24}
$$

with

$$
\begin{aligned}
\tilde{\beta}_{1,r} &= \beta_{1,r} - b_{g_r} + q_{11}^2 b_{I_r}, &\quad \tilde{\beta}_1^k &= \beta_1^k - b_{g^k} + q_{11}^2 b_{I^k} \\
\tilde{\beta}_{2,r} &= \beta_{2,r} - b_{g_r} + q_{12}^2 b_{I_r}, &\quad \tilde{\beta}_2^k &= \beta_2^k - b_{g^k} + q_{12}^2 b_{I^k}.
\end{aligned}
\tag{2.25}
$$

Secondly, the satellite phase biases of one satellite can be absorbed by the receiver phase biases. Assume that the phase biases of the first satellite are mapped to the receiver biases, one obtains

$$
\begin{aligned}
\tilde{\tilde{\beta}}_{1,r} &= \tilde{\beta}_{1,r} + \tilde{\beta}_1^1, &\quad \tilde{\tilde{\beta}}_1^k &= \tilde{\beta}_1^k - \tilde{\beta}_1^1 \\
\tilde{\tilde{\beta}}_{2,r} &= \tilde{\beta}_{2,r} + \tilde{\beta}_2^1, &\quad \tilde{\tilde{\beta}}_2^k &= \tilde{\beta}_2^k - \tilde{\beta}_2^1,
\end{aligned}
\tag{2.26}
$$

which results in $R + K - 1$ remaining phase biases on each frequency. These phase biases are estimated from a global network of reference stations, e.g. the 37 GSS Sensor Stations and the two control centers at Oberpfaffenhofen and Fucino which are shown in Fig. 2.3.
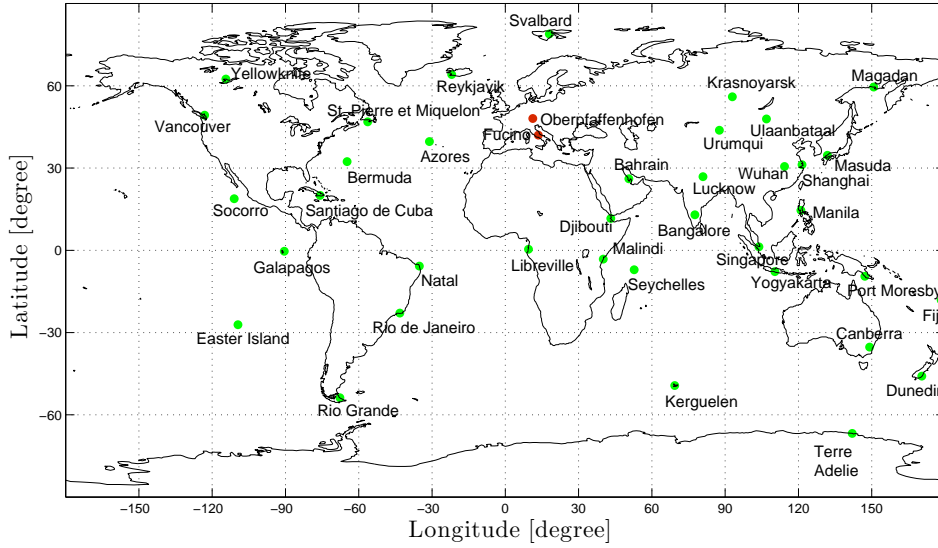


Fig. 2.3: Bias estimation with global network of 37 Galileo Sensor Stations, and the two control centers at Oberpfaffenhofen and Fucino.

Last but not least, the phase biases of (2.26) can not be separated from the integer ambiguities, and thus, $R + K - 1$ ambiguities on each frequency are mapped into phase biases. Fig. 2.4 shows the set of $K_r$ visible satellites for the 39 stations, where each point in the figure denotes an integer ambiguity for the link between a reference station and a visible satellite. As the number of ambiguities $s = \sum_{r=1}^{R} K_r$ exceeds the number

of remaining phase biases, the ambiguities are subdivided into two subsets: One subset which includes float valued ambiguities being mapped to phase biases, and another subset including integer valued ambiguities. Later the simulation results will show that, after resolving a large amount of integer ambiguities, the bias estimation can become much more accurate. It is noted that finding a subset of $R + K - 1$ ambiguities on each frequency offers some additional degrees of freedom. In this thesis, the choice of the subset of integer ambiguities comes from Gaussian Elimination, which is shortly explained in the following context.
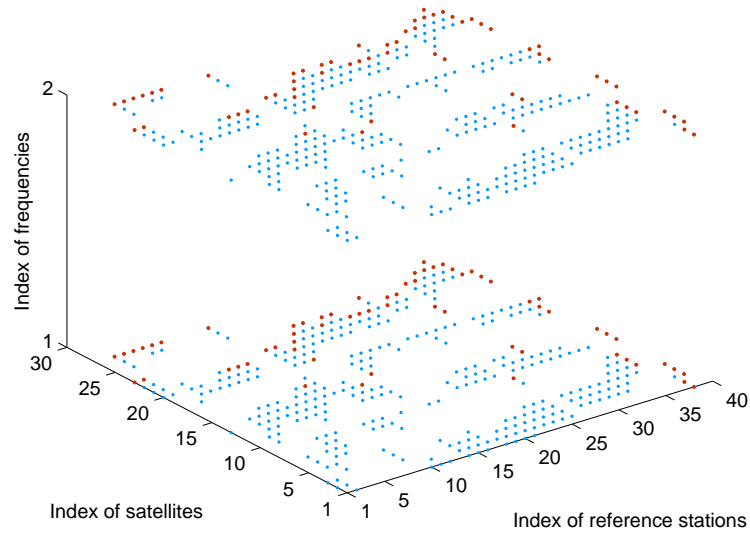


Fig. 2.4: Integer ambiguities for the network of 37 Galileo Sensor Stations and the two control centers for a snapshot 27 Galileo satellites: The blue dots refer to ambiguities that have to be estimated while the red ones are absorbed in the biases. The set of red dots are determined by Gaussian Elimination. The red dots include the ambiguities with the largest satellite index for each reference station as well as the largest reference station index for each visible satellite. As 5 ambiguities fulfill both criteria, four additional ambiguities have to be removed for a full rank measurement generation matrix.

Equation (2.27) generalizes the measurement model for illustrating the integer ambiguity mapping:

$$\boldsymbol{y} = \boldsymbol{A}\boldsymbol{x_1} + \boldsymbol{B}\boldsymbol{x_2} + \boldsymbol{\nu}, \tag{2.27}$$

where $\boldsymbol{y}$ denotes the measurement vector, $\boldsymbol{x_1}$ is the state vector for biases and integer ambiguities, $\boldsymbol{x_2}$ is the state vector for the left unknown parameters, $\boldsymbol{A}$ represents the

generation matrix of $\boldsymbol{x_1}$, which is a rank-deficient matrix, $\boldsymbol{B}$ denotes the generation matrix of $\boldsymbol{x_2}$, and $\boldsymbol{\nu}$ is the noise vector.

The process of Gaussian elimination has two parts [14]. The first part reduces the given matrix $\boldsymbol{A}$ to row echelon form. This step is accomplished through the use of elementary row operations, and gives the result of a matrix in row echelon form, which has the following properties: All non-zero rows (rows with at least one non-zero element) are above any rows of all zero rows, and the leading coefficient (the first non-zero element from the left, also called pivot) of a non-zero row is always strictly to the right of the leading coefficient of the row above it. The second part reduces it further into reduced row echelon form, which has the property besides what a normal row echelon form has: Every leading coefficient is 1 and is the only non-zero element in its column. The process is shown in Tab. (2.2), while $\boldsymbol{A}[i,j]$ represents the element in row $i$, column $j$ in the given $m \times n$ matrix $\boldsymbol{A}$.

Table 2.2: Algorithm for Gaussian elimination

**Initialize:** $i \Leftarrow 1$, $j \Leftarrow 1$

**while** $i \leq m$ && $j \leq n$ **do**

    Find pivot in column $j$ from row $i$ to row $m$, whose row index is saved as $i_{\max}$.

    **if** $\boldsymbol{A}[i_{\max}, j] \neq 0$ **then**

        Swap row $i$ and row $i_{\max}$: $\boldsymbol{A}[i,:] \leftrightarrows \boldsymbol{A}[i_{\max},:]$

        $\boldsymbol{A}[i,:] \Leftarrow \boldsymbol{A}[i,j] * \boldsymbol{A}[i,:]$

        **for** $u = i+1, \ldots, m$ **do**

            $\boldsymbol{A}[u,:] \Leftarrow \boldsymbol{A}[u,:] - \boldsymbol{A}[u,j] * \boldsymbol{A}[i,:]$

        **end for**

        $i \Leftarrow i+1$

    **end if**

    $j \Leftarrow j+1$

**end while**

The algorithm for Gaussian elimination can be also described as a set of matrix multiplications on the original generation matrix, i.e.

$$\left( \prod_{i=1}^{N} \boldsymbol{P}_i \right) \boldsymbol{A}\boldsymbol{x}_1 = \left( \prod_{i=1}^{N} \boldsymbol{P}_i \right) \begin{bmatrix} \boldsymbol{H}_{\tilde{\tilde{\beta}}_R} & \boldsymbol{H}_{\tilde{\tilde{\beta}}^S} & \boldsymbol{H}_N \end{bmatrix} \begin{bmatrix} \tilde{\tilde{\boldsymbol{\beta}}}_R \\ \tilde{\tilde{\boldsymbol{\beta}}}^S \\ \boldsymbol{N} \end{bmatrix} \triangleq \boldsymbol{C} \begin{bmatrix} \tilde{\tilde{\boldsymbol{\beta}}}_R \\ \tilde{\tilde{\boldsymbol{\beta}}}^S \\ \boldsymbol{N} \end{bmatrix}, \qquad (2.28)$$

where each $\boldsymbol{P}_i$ represents a step of the Gaussian elimination, $N$ denotes the total number of steps, and $\boldsymbol{C}$ is the coefficient matrix in reduced row echelon form.

Example: An example below with $R = 3$ receiver stations, $K = 3$ satellites and $s = \sum_{r=1}^{R} K_r = 9$ integer ambiguities shows the Gaussian elimination and ambiguity mapping. The subset of state vector writes

$$\begin{bmatrix} \tilde{\tilde{\boldsymbol{\beta}}}_R \\ \tilde{\tilde{\boldsymbol{\beta}}}^S \\ \boldsymbol{N} \end{bmatrix} = \begin{bmatrix} \tilde{\tilde{\beta}}_{m,1}, \tilde{\tilde{\beta}}_{m,2}, \tilde{\tilde{\beta}}_{m,3}, \tilde{\tilde{\beta}}_m^2, \tilde{\tilde{\beta}}_m^3, N_{m,1}^1, N_{m,1}^2, N_{m,1}^3, \dots, N_{m,3}^3 \end{bmatrix}^{\mathrm{T}}, \qquad (2.29)$$

while the corresponding generation matrix writes

$$\begin{bmatrix} \boldsymbol{H}_{\tilde{\tilde{\beta}}_R} & \boldsymbol{H}_{\tilde{\tilde{\beta}}^S} & \boldsymbol{H}_N \end{bmatrix} = \left[ \begin{array}{ccc|cc|ccccccccc} 1 & 0 & 0 & 0 & 0 & \lambda_m & 0 & 0 & 0 & 0 & 0 & 0 & 0 & 0 \\ 1 & 0 & 0 & 1 & 0 & 0 & \lambda_m & 0 & 0 & 0 & 0 & 0 & 0 & 0 \\ 1 & 0 & 0 & 0 & 1 & 0 & 0 & \lambda_m & 0 & 0 & 0 & 0 & 0 & 0 \\ 0 & 1 & 0 & 0 & 0 & 0 & 0 & 0 & \lambda_m & 0 & 0 & 0 & 0 & 0 \\ 0 & 1 & 0 & 1 & 0 & 0 & 0 & 0 & 0 & \lambda_m & 0 & 0 & 0 & 0 \\ 0 & 1 & 0 & 0 & 1 & 0 & 0 & 0 & 0 & 0 & \lambda_m & 0 & 0 & 0 \\ 0 & 0 & 1 & 0 & 0 & 0 & 0 & 0 & 0 & 0 & 0 & \lambda_m & 0 & 0 \\ 0 & 0 & 1 & 1 & 0 & 0 & 0 & 0 & 0 & 0 & 0 & 0 & \lambda_m & 0 \\ 0 & 0 & 1 & 0 & 1 & 0 & 0 & 0 & 0 & 0 & 0 & 0 & 0 & \lambda_m \end{array} \right].$$

$$(2.30)$$

After the Gaussian elimination, the coefficient matrix $\boldsymbol{C}$ in reduced row echelon form

$$\boldsymbol{C} = \left[ \begin{array}{ccc|cc|ccccccccc} 1 & 0 & 0 & 0 & 0 & 0 & 0 & * & 0 & 0 & * & * & * & * \\ 0 & 1 & 0 & 0 & 0 & 0 & 0 & * & 0 & 0 & * & * & * & * \\ 0 & 0 & 1 & 0 & 0 & 0 & 0 & * & 0 & 0 & * & * & * & * \\ 0 & 0 & 0 & 1 & 0 & 0 & 0 & * & 0 & 0 & * & * & * & * \\ 0 & 0 & 0 & 0 & 1 & 0 & 0 & * & 0 & 0 & * & * & * & * \\ \hline 0 & 0 & 0 & 0 & 0 & 1 & 0 & * & 0 & 0 & * & * & * & * \\ 0 & 0 & 0 & 0 & 0 & 0 & 1 & * & 0 & 0 & * & * & * & * \\ 0 & 0 & 0 & 0 & 0 & 0 & 0 & 0 & 1 & 0 & * & * & * & * \\ 0 & 0 & 0 & 0 & 0 & 0 & 0 & 0 & 0 & 1 & * & * & * & * \end{array} \right], \qquad (2.31)$$

where the columns with elements $*$, which could be any real value, are linear dependent on the columns before them. Thus, the mapping of ambiguities to receiver and satellite biases is given by

$$\tilde{\tilde{\beta}}_{m,r} = \tilde{\tilde{\beta}}_{m,r} + \sum_{r'=1}^{R} \sum_{k=1}^{K_{r'}} \boldsymbol{C}_{r,R+K-1+\sum_{r''=1}^{r'-1} K_{r''}+k} \cdot N_{m,r}^k, \quad \forall r \in \{1, \dots, R\}, \qquad (2.32)$$

$$\tilde{\tilde{\beta}}_m^k = \tilde{\beta}_m^k + \sum_{r=1}^{R}\sum_{k'=1}^{K_r} \boldsymbol{C}_{R+k,R+K-1+\sum_{r'=1}^{r-1} K_{r'}+k'} \cdot N_{m,r}^{k'}, \quad \forall k \in \{1,\dots,K-1\}, \qquad (2.33)$$

and the mapping of ambiguities to ambiguities is given by

$$\tilde{N}_{m,r_\mu(l)}^{k_\mu(l)} = N_{m,r_\mu(l)}^{k_\mu(l)} + \sum_{r=r_\mu(l)}^{R}\sum_{k=k_\mu(l)}^{K_r} \boldsymbol{C}_{R+k-1+l,R+K-1+\sum_{r'=1}^{r-1} K_{r'}+k} \cdot N_{m,r}^{k}, \qquad (2.34)$$

where $N_{m,r_\mu(l)}^{k_\mu(l)}$ denotes the ambiguity of the $r_\mu(l)$-th receiver and the $k_\mu(l)$-th satellite. The pivot elements for ambiguities, which are marked in red, are in the $(R+K-1+l)$-th row of matrix $\boldsymbol{C}$, with $l \in \{1,\dots,s-(R+K-1)\}$.

Therefore, the Gaussian Elimination method helps to transfer the problem of determining which ambiguities should be mapped away into the problem of which columns in the generation matrix can be written as the linear combinations of other columns. The columns that do not have a leading coefficient 1 for one particular row, corresponds to the ambiguities that have to be mapped into the phase biases and other ambiguities.

## 2.4 Conclusion: Measurement Model after Mapping

After a few steps of parameter mapping, the system of equations (2.1) turns into the following equation and also becomes solvable, i.e.

$$
\begin{aligned}
\lambda_1 \phi_{1,r}^k(t_n) &= \tilde{g}_r^k(t_n) - q_{11}^2 \tilde{I}_{1,r}^k(t_n) + \lambda_1 \tilde{N}_{1,r}^k + \tilde{\tilde{\beta}}_{1,r} + \tilde{\tilde{\beta}}_1^k + \varepsilon_{1,r}^k(t_n) \\
\lambda_2 \phi_{2,r}^k(t_n) &= \tilde{g}_r^k(t_n) - q_{12}^2 \tilde{I}_{1,r}^k(t_n) + \lambda_2 \tilde{N}_{2,r}^k + \tilde{\tilde{\beta}}_{2,r} + \tilde{\tilde{\beta}}_2^k + \varepsilon_{2,r}^k(t_n) \\
\lambda_3 \phi_{3,r}^k(t_n) &= \tilde{g}_r^k(t_n) - q_{13}^2 \tilde{I}_{1,r}^k(t_n) + \lambda_3 \tilde{N}_{3,r}^k + \tilde{\tilde{\beta}}_{3,r} + \tilde{\tilde{\beta}}_3^k + \varepsilon_{3,r}^k(t_n) \\
\rho_{1,r}^k(t_n) &= \tilde{g}_r^k(t_n) + q_{11}^2 \tilde{I}_{1,r}^k(t_n) + \eta_{1,r}^k(t_n) \\
\rho_{2,r}^k(t_n) &= \tilde{g}_r^k(t_n) + q_{12}^2 \tilde{I}_{1,r}^k(t_n) + \eta_{2,r}^k(t_n) \\
\rho_{3,r}^k(t_n) &= \tilde{g}_r^k(t_n) + q_{13}^2 \tilde{I}_{1,r}^k(t_n) + \tilde{b}_{3,r} + \tilde{b}_3^k + \eta_{3,r}^k(t_n),
\end{aligned}
\qquad (2.35)
$$

with $\tilde{g}_r^k$, $\tilde{I}_{1,r}^k$, $\tilde{\tilde{\beta}}_{1,r}$, $\tilde{\tilde{\beta}}_1^k$, $\tilde{\tilde{\beta}}_{2,r}$ and $\tilde{\tilde{\beta}}_2^k$ described in Eq.(2.20), (2.21), (2.25), (2.26), (2.32) and (2.33), and $\tilde{N}_{1,r}^k$, $\tilde{N}_{2,r}^k$ from Eq. (2.34) shown in Fig. 2.4. The phase biases and ambiguities on the third frequency can be obtained similarly with the ones on the other two frequencies, while the code biases on the third frequency can not be mapped to ranges and ionospheric delays, and the first satellite code bias is mapped to receiver code biases.

# 3 Estimation of Code and Carrier Phase Biases

## 3.1 Fundamentals of Kalman Filtering

The precise estimation of receiver and satellite biases requires a global network and a few hundred epochs which motivate a recursive state estimation, e.g. a Kalman filter (Brown and Hwang [15]). This section focuses on the principles of a Kalman filter, including the predict and update equations of state vectors.

A Kalman filter is based on a linear discrete-time dynamical system. At each discrete time increment, a linear operator is applied to the state to generate the new state, with some noise mixed in. The knowledge of the system dynamics is used to generate a linear discrete-time state space model, which contains a random process. The state space model of the linear system can be written as

$$\boldsymbol{x}_n = \boldsymbol{\Phi}_{n-1}\boldsymbol{x}_{n-1} + \boldsymbol{w}_n, \tag{3.1}$$

where $\boldsymbol{x}_n$ denotes the true state vector, $\boldsymbol{\Phi}_n$ indicates the state transition matrix, and $\boldsymbol{w}_n$ is the process noise vector at epoch $n$. The process noise vector follows a zero mean white Gaussian distribution with a noise covariance matrix $\boldsymbol{\Sigma}_Q$, i.e. $\boldsymbol{w} \sim \mathcal{N}(0, \boldsymbol{\Sigma}_Q)$.

At epoch $n$, measurement vector $\boldsymbol{z}_n$ of the true state vector $\boldsymbol{x}_n$ is produced according to

$$\boldsymbol{z}_n = \boldsymbol{H}_n\boldsymbol{x}_n + \boldsymbol{v}_n, \tag{3.2}$$

where $\boldsymbol{v}_n$ is the measurement noise which is assumed to be zero mean white Gaussian noise with covariance $\boldsymbol{\Sigma}_R$.

The estimation of state vector $\boldsymbol{x}_n$ based on a Kalman filter includes two distinct phases: prediction and update. The a priori state estimate $\hat{\boldsymbol{x}}_{n+1}^-$ at epoch $n+1$ is obtained from the $n$-th epoch a posteriori state estimate $\hat{\boldsymbol{x}}_n^+$, i.e.

$$\hat{\boldsymbol{x}}_{n+1}^- = \boldsymbol{\Phi}\hat{\boldsymbol{x}}_n^+. \tag{3.3}$$

The covariance matrix of the predicted state estimate follows as

$$\boldsymbol{P}_{\hat{\boldsymbol{x}}_{n+1}^-} = \boldsymbol{\Phi}\boldsymbol{P}_{\hat{\boldsymbol{x}}_n^+}\boldsymbol{\Phi}^{\mathrm{T}} + \boldsymbol{\Sigma}_{\mathrm{Q}}. \tag{3.4}$$

According to the measurements of the next epoch, the predicted state is then updated, i.e. the a posteriori state estimate is obtained from

$$\hat{\boldsymbol{x}}_n^+ = \hat{\boldsymbol{x}}_n^- + \boldsymbol{K}_n(\boldsymbol{z}_n - \boldsymbol{H}_n\hat{\boldsymbol{x}}_n^-), \tag{3.5}$$

where $\boldsymbol{z}_n - \boldsymbol{H}_n\hat{\boldsymbol{x}}_n^-$ indicates the measurement residual and $\boldsymbol{K}_n$ is the Kalman gain, which is chosen such that

$$\min_{\boldsymbol{K}_n} \mathrm{E}\{\|\hat{\boldsymbol{x}}_n^+ - \boldsymbol{x}_n\|^2\} = \min_{\boldsymbol{K}_n} \mathrm{tr}(\boldsymbol{P}_{\hat{\boldsymbol{x}}_n^+}), \tag{3.6}$$

where $\boldsymbol{P}_{\hat{\boldsymbol{x}}_n^+}$ denotes the a posteriori state covariance matrix that is obtained from Eq. (3.5):

$$
\begin{aligned}
\boldsymbol{P}_{\hat{\boldsymbol{x}}_n^+} &= \mathrm{E}\{(\hat{\boldsymbol{x}}_n^+ - \boldsymbol{x}_n)(\hat{\boldsymbol{x}}_n^+ - \boldsymbol{x}_n)^{\mathrm{T}}\} \\
&= \mathrm{E}\{(\hat{\boldsymbol{x}}_n^- + \boldsymbol{K}_n(\boldsymbol{z}_n - \boldsymbol{H}_n\hat{\boldsymbol{x}}_n^-) - \boldsymbol{x}_n)(\hat{\boldsymbol{x}}_n^- + \boldsymbol{K}_n(\boldsymbol{z}_n - \boldsymbol{H}_n\hat{\boldsymbol{x}}_n^-) - \boldsymbol{x}_n)^{\mathrm{T}}\} \\
&= \mathrm{E}\{(\hat{\boldsymbol{x}}_n^- + \boldsymbol{K}_n(\boldsymbol{H}_n\boldsymbol{x}_n + \boldsymbol{v}_n - \boldsymbol{H}_n\hat{\boldsymbol{x}}_n^-) - \boldsymbol{x}_n)(\hat{\boldsymbol{x}}_n^- + \boldsymbol{K}_n(\boldsymbol{H}_n\boldsymbol{x}_n + \boldsymbol{v}_n - \boldsymbol{H}_n\hat{\boldsymbol{x}}_n^-) - \boldsymbol{x}_n)^{\mathrm{T}}\} \\
&= \mathrm{E}\{((\mathbf{1} - \boldsymbol{K}_n\boldsymbol{H}_n)(\hat{\boldsymbol{x}}_n^- - \boldsymbol{x}_n) + \boldsymbol{K}_n\boldsymbol{v}_n)((\mathbf{1} - \boldsymbol{K}_n\boldsymbol{H}_n)(\hat{\boldsymbol{x}}_n^- - \boldsymbol{x}_n) + \boldsymbol{K}_n\boldsymbol{v}_n)^{\mathrm{T}}\}.
\end{aligned} \tag{3.7}
$$

Since the measurement noise vector $\boldsymbol{v}_n$ is uncorrelated with other terms, $\boldsymbol{P}_{\hat{\boldsymbol{x}}_n^+}$ can be further derived as

$$
\begin{aligned}
\boldsymbol{P}_{\hat{\boldsymbol{x}}_n^+} &= (\mathbf{1} - \boldsymbol{K}_n\boldsymbol{H}_n)\mathrm{E}\{(\hat{\boldsymbol{x}}_n^- - \boldsymbol{x}_n)(\hat{\boldsymbol{x}}_n^- - \boldsymbol{x}_n)^{\mathrm{T}}\}(\mathbf{1} - \boldsymbol{K}_n\boldsymbol{H}_n)^{\mathrm{T}} + \boldsymbol{K}_n\mathrm{E}\{\boldsymbol{v}_n\boldsymbol{v}_n^{\mathrm{T}}\}\boldsymbol{K}_n^{\mathrm{T}} \\
&= (\mathbf{1} - \boldsymbol{K}_n\boldsymbol{H}_n)\boldsymbol{P}_{\hat{\boldsymbol{x}}_n^-}(\mathbf{1} - \boldsymbol{K}_n\boldsymbol{H}_n)^{\mathrm{T}} + \boldsymbol{K}_n\boldsymbol{\Sigma}_{\mathrm{R}}\boldsymbol{K}_n^{\mathrm{T}} \\
&= \boldsymbol{P}_{\hat{\boldsymbol{x}}_n^-} - \boldsymbol{P}_{\hat{\boldsymbol{x}}_n^-}\boldsymbol{H}_n^{\mathrm{T}}\boldsymbol{K}_n^{\mathrm{T}} - \boldsymbol{K}_n\boldsymbol{H}_n\boldsymbol{P}_{\hat{\boldsymbol{x}}_n^-} + \boldsymbol{K}_n(\boldsymbol{H}_n\boldsymbol{P}_{\hat{\boldsymbol{x}}_n^-}\boldsymbol{H}_n^{\mathrm{T}} + \boldsymbol{\Sigma}_{\mathrm{R}})\boldsymbol{K}_n^{\mathrm{T}}.
\end{aligned} \tag{3.8}
$$

Setting the matrix derivation $\partial\mathrm{tr}(\boldsymbol{P}_{\hat{\boldsymbol{x}}_n^+})/\partial\boldsymbol{K}_n = 0$ and solving for $\boldsymbol{K}_n$ yields the optimal Kalman gain

$$\boldsymbol{K}_n = \boldsymbol{P}_{\hat{\boldsymbol{x}}_n^-}\boldsymbol{H}_n(\boldsymbol{H}_n\boldsymbol{P}_{\hat{\boldsymbol{x}}_n^-}\boldsymbol{H}_n^{\mathrm{T}} + \boldsymbol{\Sigma}_{\mathrm{R}})^{-1}, \tag{3.9}$$

which is used in Eq. (3.5) to obtain an a posteriori MMSE estimator. Equation (3.8) can be simplified by replacing the optimal Kalman gain by Eq. (3.9), i.e.

$$\boldsymbol{P}_{\hat{\boldsymbol{x}}_n^+} = (\mathbf{1} - \boldsymbol{K}_n\boldsymbol{H}_n)\boldsymbol{P}_{\hat{\boldsymbol{x}}_n^-}. \tag{3.10}$$

Moreover, the a posteriori state estimate $\hat{\boldsymbol{x}}_n^+$ can be computed in an iterative way from the measurement vector $\boldsymbol{z}_n$ based on Eq. (3.3) and (3.5), i.e.

$$
\begin{aligned}
\hat{\boldsymbol{x}}_n^+ &= \hat{\boldsymbol{x}}_n^- + \boldsymbol{K}_n(\boldsymbol{z}_n - \boldsymbol{H}_n\hat{\boldsymbol{x}}_n^-) \\
&= (\mathbf{1} - \boldsymbol{K}_n\boldsymbol{H}_n)\hat{\boldsymbol{x}}_n^- + \boldsymbol{K}_n\boldsymbol{z}_n \\
&= (\mathbf{1} - \boldsymbol{K}_n\boldsymbol{H}_n)\boldsymbol{\Phi}\hat{\boldsymbol{x}}_{n-1}^+ + \boldsymbol{K}_n\boldsymbol{z}_n.
\end{aligned} \tag{3.11}
$$

Thus, the above iterative equation is equivalent to the non-recursive form

$$\hat{\boldsymbol{x}}_n^+ = \left[\prod_{l=1}^{n}(\mathbf{1} - \boldsymbol{K}_{n-l+1}\boldsymbol{H}_{n-l+1})\Phi\right]\Phi^{-1}\hat{\boldsymbol{x}}_0^- + \sum_{l=1}^{n}\left(\prod_{m=0}^{n-l-1}(\mathbf{1} - \boldsymbol{K}_{n-m}\boldsymbol{H}_{n-m})\Phi\right)\boldsymbol{K}_l\boldsymbol{z}_l,$$

(3.12)

where the first term represents the impact of the state initialization $\hat{\boldsymbol{x}}_1^-$ and the second term describes the impact of the measurement vector $\boldsymbol{z}_n$.

To conclude, Kalman filter benefits from the prior knowledge of the dynamical process model, and minimizes the mean square error between the a posteriori state estimate and the true state. During the estimation process, the predicted state of the next epoch is generated based on the a posteriori state of the last epoch, while the covariance of the predicted state is generated similarly based on the covariance of the a posteriori state. The state is then updated according to the state prediction and the measurement residual with a certain weighting, which is obtained from finding the optimum criterion to minimize the mean square error of the a posteriori state estimate.

## 3.2 Estimation of Receiver and Satellite Phase Biases

### 3.2.1 System Description

Estimating receiver and satellite phase biases in Eq. (2.35) with a Kalman filter, the state vector includes the ranges, range rates, ionospheric delays, receiver and satellite phase biases and ambiguities, i.e.

$$\boldsymbol{x}_n = \left[\tilde{\boldsymbol{g}}^{\mathrm{T}}(t_n),\ \dot{\tilde{\boldsymbol{g}}}^{\mathrm{T}}(t_n),\ \tilde{\boldsymbol{I}}^{\mathrm{T}}(t_n),\ \tilde{\tilde{\boldsymbol{\beta}}}_{\mathrm{R}}^{\mathrm{T}},\ \tilde{\tilde{\boldsymbol{\beta}}}_{\mathrm{S}}^{\mathrm{T}},\ \tilde{\boldsymbol{N}}\right]^{\mathrm{T}},$$

(3.13)

with

$$
\begin{aligned}
\tilde{\boldsymbol{g}}(t_n) &= \left[\tilde{g}_1^1(t_n),\ldots,\tilde{g}_1^{K_1}(t_n),\ldots,\tilde{g}_R^1(t_n),\ldots,\tilde{g}_R^{K_R}(t_n)\right]^{\mathrm{T}} \\
\dot{\tilde{g}}(t_n) &= \left[\dot{\tilde{g}}_1^1(t_n),\ldots,\dot{\tilde{g}}_1^{K_1}(t_n),\ldots,\dot{\tilde{g}}_R^1(t_n),\ldots,\dot{\tilde{g}}_R^{K_R}(t_n)\right]^{\mathrm{T}} \\
\tilde{\boldsymbol{I}}(t_n) &= \left[\tilde{I}_1^1(t_n),\ldots,\tilde{I}_1^{K_1}(t_n),\ldots,\tilde{I}_R^1(t_n),\ldots,\tilde{I}_R^{K_R}(t_n)\right]^{\mathrm{T}} \\
\tilde{\tilde{\boldsymbol{\beta}}}_R &= \left[\tilde{\tilde{\beta}}_{1,1},\ldots,\tilde{\tilde{\beta}}_{1,R},\tilde{\tilde{\beta}}_{2,1},\ldots,\tilde{\tilde{\beta}}_{2,R}\right]^{\mathrm{T}} \\
\tilde{\tilde{\boldsymbol{\beta}}}^S &= \left[\tilde{\tilde{\beta}}_1^2,\ldots,\tilde{\tilde{\beta}}_1^K,\tilde{\tilde{\beta}}_2^2,\ldots,\tilde{\tilde{\beta}}_2^K\right]^{\mathrm{T}},
\end{aligned}
$$

(3.14)

and the subset of integer valued ambiguities $\tilde{\boldsymbol{N}}$.

The vector $\boldsymbol{z}_n$ describes the phase and code measurements of Eq. (2.35), i.e.

$$\boldsymbol{z}_n = \left[\lambda_1 \phi_{1,1}^1(t_n), \ldots, \lambda_1 \phi_{1,R}^{K_R}(t_n), \ldots, \lambda_2 \phi_{2,R}^{K_R}(t_n), \ \rho_{1,1}^1(t_n), \ldots, \rho_{1,R}^{K_R}(t_n), \ldots, \rho_{2,R}^{K_R}(t_n)\right]^{\mathrm{T}}.$$
(3.15)

The generation matrix in Eq. (3.2) consists of the following components

$$\boldsymbol{H} = \begin{bmatrix} \boldsymbol{H}_{\tilde{g}} & \boldsymbol{H}_{\dot{\tilde{g}}} & \boldsymbol{H}_{\tilde{I}} & \boldsymbol{H}_{\tilde{\tilde{\beta}}_R} & \boldsymbol{H}_{\tilde{\tilde{\beta}}S} & \boldsymbol{H}_{\tilde{N}} \end{bmatrix},$$
(3.16)

with

$$\boldsymbol{H}_{\tilde{g}} = \mathbf{1}^{4 \times 1} \otimes \mathbf{1}^{s \times s}, \quad \boldsymbol{H}_{\dot{\tilde{g}}} = \mathbf{0}^{4s \times s},$$

$$\boldsymbol{H}_{\tilde{I}} = [-q_{11}^2 \quad -q_{12}^2 \quad q_{11}^2 \quad q_{12}^2]^{\mathrm{T}} \otimes \mathbf{1}^{s \times s},$$

$$\boldsymbol{H}_{\tilde{\tilde{\beta}}_R} = \begin{bmatrix} \mathbf{1}^{2 \times 2} \\ \mathbf{0}^{2 \times 2} \end{bmatrix} \otimes \begin{bmatrix} \mathbf{1}^{K_1 \times 1} & & & \\ & \mathbf{1}^{K_2 \times 1} & & \\ & & \ddots & \\ & & & \mathbf{1}^{K_R \times 1} \end{bmatrix},$$
(3.17)

where operator $\otimes$ denotes the tensor product, $\boldsymbol{H}_{\tilde{\tilde{\beta}}S}$ has the dimension of $4s \times 2(K-1)$ and mapping satellite biases to measurements, and $\boldsymbol{H}_{\tilde{\mathrm{N}}}$ represents the integer ambiguity mapping matrix of dimension $4s \times (2s - 2(R + K - 1))$, which comes from the following matrix $\boldsymbol{H}_N$ by reducing $2(R + K - 1)$ columns with Gaussian Elimination method to avoid $\boldsymbol{H}$ getting rank deficient, i.e.

$$\boldsymbol{H}_N = \begin{bmatrix} 1 \\ 0 \end{bmatrix} \otimes \begin{bmatrix} \lambda_1 & 0 \\ 0 & \lambda_2 \end{bmatrix} \otimes \mathbf{1}^{s \times s},$$
(3.18)

where $\lambda_1$ and $\lambda_2$ are the wavelengths, and $s$ denotes the number of available carrier phase measurements on one frequency, i.e.

$$s = \sum_{r=1}^{R} K_r.$$
(3.19)

The measurement noise in Eq. (3.2) is assumed to be uncorrelated between satellites and follows a zero mean white Gaussian distribution with the variances $\sigma_{\phi_{m,r}^k}^2$ and $\sigma_{\rho_{m,r}^k}^2$.

A linear dynamic model is used for the range term $\tilde{g}_r^k(t_n)$, i.e.

$$\tilde{g}_r^k(t_n) = \tilde{g}_r^k(t_{n-1}) + \Delta t \cdot \dot{\tilde{g}}_r^k(t_{n-1}) + w_{\tilde{g}_r^k}(t_n).$$
(3.20)

The state transition matrix in Eq. (3.1) is then obtained as

$$\mathbf{\Phi} = \begin{bmatrix} \mathbf{1}^{s \times s} & \Delta t \cdot \mathbf{1}^{s \times s} & \mathbf{0} \\ \mathbf{0} & \mathbf{1}^{s \times s} & \mathbf{0} \\ \mathbf{0} & \mathbf{0} & \mathbf{1}^{3s \times 3s} \end{bmatrix}, \tag{3.21}$$

where $\Delta t$ represents the interval between two measurement epochs. The noise covariance matrix $\mathbf{\Sigma}_Q$ in Eq. (3.1) was derived by Brown and Hwang [15] using the model in Fig. 3.1
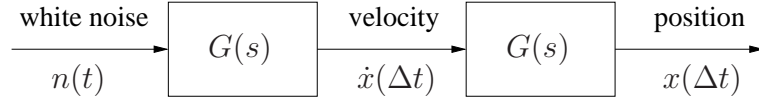


Fig. 3.1: Random walk model on range rate.

The transfer functions describe the integration, i.e.

$$\begin{aligned} G_1(s) &= G(s) = \frac{1}{s} \quad \xrightarrow{\mathfrak{L}^{-1}} \quad g_1(t) = u(t) \\ G_2(s) &= G(s)^2 = \frac{1}{s^2} \quad \xrightarrow{\mathfrak{L}^{-1}} \quad g_2(t) = t \cdot u(t). \end{aligned} \tag{3.22}$$

It is assumed that the white noise $n(t)$ is uncorrelated between different epochs. Thus, the noise variances and covariances on range and range rate can be calculated as

$$\begin{aligned} \mathrm{E}\{\dot{x}(\Delta t)\dot{x}(\Delta t)\} &= \mathrm{E}\{(n(t) * g_1(t)) \cdot (n(t) * g_1(t))\} \\ &= \mathrm{E}\left\{ \int_0^{\Delta t} n(w)dw \cdot \int_0^{\Delta t} n(v)dv \right\} \\ &= \mathrm{E}\left\{ \int_0^{\Delta t} \int_0^{\Delta t} n(w)n(v) \cdot \delta(w - v)dwdv \right\} \\ &= \int_0^{\Delta t} \int_0^{\Delta t} \mathrm{E}\{n^2(w)\} \cdot \delta(w - v)dwdv \\ &= \int_0^{\Delta t} \int_0^{\Delta t} S_p \cdot \delta(w - v)dwdv = S_p \cdot \Delta t, \end{aligned} \tag{3.23}$$

$$\begin{aligned} \mathrm{E}\{x(\Delta t)\dot{x}(\Delta t)\} &= \mathrm{E}\{(n(t) * g_2(t)) \cdot (n(t) * g_1(t))\} \\ &= \mathrm{E}\left\{ \int_0^{\Delta t} n(t - w)wdw \cdot \int_0^{\Delta t} n(\tau)d\tau \right\} \\ &= \mathrm{E}\left\{ \int_0^{\Delta t} \int_0^{\Delta t} n(t - w)n(\tau) \cdot w \cdot \delta(t - w - \tau)dwd\tau \right\} \\ &= \int_0^{\Delta t} \int_0^{\Delta t} \mathrm{E}\{n^2(w)\} \cdot w \cdot \delta(t - w - \tau)dwd\tau \\ &= \int_0^{\Delta t} \int_0^{\Delta t} S_p \cdot w \cdot \delta(w - v)dwdv = S_p \cdot \frac{\Delta t^2}{2}, \end{aligned} \tag{3.24}$$

$$
\begin{aligned}
\mathrm{E}\{x(\Delta t)x(\Delta t)\} &= \mathrm{E}\{(n(t)*g_2(t))\cdot(n(t)*g_2(t))\} \\
&= \mathrm{E}\left\{\int_0^{\Delta t} n(t-w)\cdot w\,dw \cdot \int_0^{\Delta t} n(t-v)\cdot v\,dv\right\} \\
&= \mathrm{E}\left\{\int_0^{\Delta t}\int_0^{\Delta t} n(t-w)n(t-v)\cdot w\cdot v\cdot \delta((t-w)-(t-v))dwdv\right\} \\
&= \int_0^{\Delta t}\int_0^{\Delta t} \mathrm{E}\{n^2(t-w)\}\cdot w\cdot v\cdot \delta(v-w)dwdv \\
&= \int_0^{\Delta t}\int_0^{\Delta t} S_p\cdot w\cdot v\cdot \delta(w-v)dwdv = S_p\cdot\frac{\Delta t^3}{3},
\end{aligned}
\tag{3.25}
$$

where $*$ denotes the convolution calculator. Thus, the state covariance matrix of range and range-rate related errors is given by

$$
\boldsymbol{\Sigma}_{\mathrm{Q},\tilde g\dot{\tilde g}} = S_p\cdot\Delta t\cdot
\begin{bmatrix}
\frac{\Delta t^2}{3} & \frac{\Delta t}{2} \\
\frac{\Delta t}{2} & 1
\end{bmatrix}
\otimes \mathbf{1}^{s\times s}.
\tag{3.26}
$$

The calculation of noise variances and covariances on a more accurate model, including the range accelerations, is similar with (3.23)-(3.25) and derived in Appendix 7.1, which gives the results as

$$
\begin{aligned}
\mathrm{E}\{\ddot x(\Delta t)\ddot x(\Delta t)\} &= \int_0^{\Delta t}\int_0^{\Delta t} S_p\cdot 1\cdot 1\cdot \delta(w-v)dwdv = S_p\cdot\Delta t \\
\mathrm{E}\{\dot x(\Delta t)\ddot x(\Delta t)\} &= \int_0^{\Delta t}\int_0^{\Delta t} S_p\cdot w\cdot 1\cdot \delta(w-v)dwdv = \frac{1}{2}S_p\cdot\Delta t^2 \\
\mathrm{E}\{x(\Delta t)\ddot x(\Delta t)\} &= \int_0^{\Delta t}\int_0^{\Delta t} S_p\cdot\frac{1}{2}w^2\cdot 1\cdot \delta(w-v)dwdv = \frac{1}{6}S_p\cdot\Delta t^3 \\
\mathrm{E}\{\dot x(\Delta t)\dot x(\Delta t)\} &= \int_0^{\Delta t}\int_0^{\Delta t} S_p\cdot w\cdot v\cdot \delta(w-v)dwdv = \frac{1}{3}S_p\cdot\Delta t^3 \\
\mathrm{E}\{x(\Delta t)\dot x(\Delta t)\} &= \int_0^{\Delta t}\int_0^{\Delta t} S_p\cdot\frac{1}{2}w^2\cdot v\cdot \delta(w-v)dwdv = \frac{1}{8}S_p\cdot\Delta t^4 \\
\mathrm{E}\{x(\Delta t)x(\Delta t)\} &= \int_0^{\Delta t}\int_0^{\Delta t} S_p\cdot\frac{1}{2}w^2\cdot\frac{1}{2}v^2\cdot \delta(w-v)dwdv = \frac{1}{20}S_p\cdot\Delta t^5,
\end{aligned}
\tag{3.27}
$$

and forms the covariance matrix for range, range rate, and the range accelerations, i.e.

$$
\boldsymbol{\Sigma}_{\mathrm{Q},\tilde g\dot{\tilde g}\ddot{\tilde g}} = S_p\cdot\Delta t\cdot
\begin{bmatrix}
\frac{1}{20}\Delta t^4 & \frac{1}{8}\Delta t^3 & \frac{1}{6}\Delta t^2 \\
\frac{1}{8}\Delta t^3 & \frac{1}{3}\Delta t^2 & \frac{1}{2}\Delta t \\
\frac{1}{6}\Delta t^2 & \frac{1}{2}\Delta t & 1
\end{bmatrix}
\otimes \mathbf{1}^{s\times s}.
\tag{3.28}
$$

The whole noise covariance matrix $\boldsymbol{\Sigma}_{\mathrm{Q}}$ is given by

$$
\boldsymbol{\Sigma}_{\mathrm{Q}} =
\begin{bmatrix}
\boldsymbol{\Sigma}_{\mathrm{Q},\tilde g\dot{\tilde g}} & \mathbf{0} & \mathbf{0} \\
\mathbf{0} & \boldsymbol{\Sigma}_{\mathrm{Q},\tilde I} & \mathbf{0} \\
\mathbf{0} & \mathbf{0} & \boldsymbol{\Sigma}_{\mathrm{Q},\tilde\beta,\tilde N}
\end{bmatrix},
\tag{3.29}
$$

with

$$\mathbf{\Sigma}_{Q,\tilde{I}} = \sigma_I^2 \cdot \mathbf{1}^{s \times s} \quad \text{and} \quad \mathbf{\Sigma}_{Q,\tilde{\tilde{\beta}},\tilde{N}} = \mathbf{0}^{2s \times 2s},$$ (3.30)

which means no process noise is assumed for the biases and integer ambiguities.

### 3.2.2 Least-squares Initialization

Up to now, the Kalman filter predict and update estimations have been set up. The initial estimate of the state vector and its covariance matrix for initializing the Kalman filter are determined by a simple least-squares estimation. Measurements of first two epochs are required as both the range and the range rate are estimated. The measurements for two epochs are modeled as

$$\begin{bmatrix} \boldsymbol{z}(t_n) \\ \boldsymbol{z}(t_{n+1}) \end{bmatrix} = \boldsymbol{H}_{\text{comb}} \cdot \begin{bmatrix} \boldsymbol{x}(t_n) \\ \boldsymbol{x}(t_{n+1}) \end{bmatrix} + \begin{bmatrix} \boldsymbol{v}(t_n) \\ \boldsymbol{v}(t_{n+1}) \end{bmatrix},$$ (3.31)

with

$$\boldsymbol{H}_{\text{comb}} = \begin{bmatrix} \boldsymbol{H}_{\tilde{g}} & \boldsymbol{0} & \boldsymbol{H}_{\tilde{I}} & \boldsymbol{0} & \boldsymbol{H}_{\tilde{\tilde{\beta}}_R} & \boldsymbol{H}_{\tilde{\tilde{\beta}}S} & \boldsymbol{H}_{\tilde{N}} \\ \boldsymbol{0} & \boldsymbol{H}_{\tilde{g}} & \boldsymbol{0} & \boldsymbol{H}_{\tilde{I}} & \boldsymbol{H}_{\tilde{\tilde{\beta}}_R} & \boldsymbol{H}_{\tilde{\tilde{\beta}}S} & \boldsymbol{H}_{\tilde{N}} \end{bmatrix}.$$ (3.32)

Thus, the least-squares estimation for $\boldsymbol{x}(t_n)$, $\boldsymbol{x}(t_{n+1})$ is given by

$$\begin{bmatrix} \hat{\boldsymbol{x}}(t_n) \\ \hat{\boldsymbol{x}}(t_{n+1}) \end{bmatrix} = (\boldsymbol{H}_{\text{comb}}^{\text{T}} \mathbf{\Sigma}_{\text{comb}}^{-1} \boldsymbol{H}_{\text{comb}})^{-1} \boldsymbol{H}_{\text{comb}}^{\text{T}} \mathbf{\Sigma}_{\text{comb}}^{-1} \cdot \begin{bmatrix} \boldsymbol{z}(t_n) \\ \boldsymbol{z}(t_{n+1}) \end{bmatrix},$$ (3.33)

with

$$\mathbf{\Sigma}_{\text{comb}} = \mathbf{1}^{2 \times 2} \otimes \mathbf{\Sigma}_{\text{R}},$$ (3.34)

and $\boldsymbol{x}(t_n)$ is the state vector of (3.13) excluding the range rate $\dot{\tilde{\boldsymbol{g}}}$, which will be estimated by differencing the state estimates $\hat{\boldsymbol{x}}_{\tilde{g}}(t_{n+1})$ and $\hat{\boldsymbol{x}}_{\tilde{g}}(t_n)$, i.e.

$$\dot{\hat{\tilde{\boldsymbol{g}}}}(t_n) = \frac{1}{\Delta t} \cdot (\hat{\boldsymbol{x}}_{\tilde{g}}(t_{n+1}) - \hat{\boldsymbol{x}}_{\tilde{g}}(t_n)).$$ (3.35)

The estimated noise variances and covariances of range and range rate can be derived from the covariances of the least-squares estimates as

$$\begin{aligned} \mathbf{\Sigma}'_{\hat{\tilde{g}}_n \hat{\tilde{g}}_n} &= \mathbf{\Sigma}_{\hat{\tilde{g}}_n \hat{\tilde{g}}_n} \\ \mathbf{\Sigma}'_{\hat{\tilde{g}}_n \hat{\dot{\tilde{g}}}_n} &= \frac{1}{\Delta t} \cdot (\mathbf{\Sigma}_{\hat{\tilde{g}}_n \hat{\tilde{g}}_{n+1}} - \mathbf{\Sigma}_{\hat{\tilde{g}}_n \hat{\tilde{g}}_n}) \\ \mathbf{\Sigma}'_{\hat{\dot{\tilde{g}}}_n \hat{\dot{\tilde{g}}}_n} &= \frac{1}{\Delta t^2} \cdot (\mathbf{\Sigma}_{\hat{\tilde{g}}_{n+1} \hat{\tilde{g}}_{n+1}} - 2\mathbf{\Sigma}_{\hat{\tilde{g}}_n \hat{\tilde{g}}_{n+1}} + \mathbf{\Sigma}_{\hat{\tilde{g}}_n \hat{\tilde{g}}_n}) \end{aligned}$$ (3.36)

A more accurate state space model includes the second derivative $\ddot{\hat{\boldsymbol{g}}}$ of the range, of which an initial estimate can be obtained with three epochs. The relationship between the range, range rate and the second derivative of the range is shown as

$$\dot{\hat{\boldsymbol{g}}}(t_n) = \frac{1}{2\Delta t} \cdot (\hat{\boldsymbol{g}}(t_{n+1}) - \hat{\boldsymbol{g}}(t_{n-1})) \tag{3.37}$$

$$\ddot{\hat{\boldsymbol{g}}}(t_n) = \frac{1}{\Delta t} \cdot \left( \frac{\hat{\boldsymbol{g}}(t_{n+1}) - \hat{\boldsymbol{g}}(t_n)}{\Delta t} - \frac{\hat{\boldsymbol{g}}(t_n) - \hat{\boldsymbol{g}}(t_{n-1})}{\Delta t} \right)$$

$$= \frac{1}{\Delta t^2} \cdot (\hat{\boldsymbol{g}}(t_{n+1}) - 2\hat{\boldsymbol{g}}(t_n) + \hat{\boldsymbol{g}}(t_{n-1})), \tag{3.38}$$

with the variances and covariances

$$\boldsymbol{\Sigma}'_{\hat{g}_n \hat{g}_n} = \boldsymbol{\Sigma}_{\hat{g}_n \hat{g}_n}$$

$$\boldsymbol{\Sigma}'_{\dot{\hat{g}}_n \hat{g}_n} = \frac{1}{2\Delta t} \cdot (\boldsymbol{\Sigma}_{\hat{g}_n \hat{g}_{n+1}} - \boldsymbol{\Sigma}_{\hat{g}_n \hat{g}_{n-1}})$$

$$\boldsymbol{\Sigma}'_{\ddot{\hat{g}}_n \hat{g}_n} = \frac{1}{\Delta t^2} \cdot (\boldsymbol{\Sigma}_{\hat{g}_n \hat{g}_{n+1}} - 2\boldsymbol{\Sigma}_{\hat{g}_n \hat{g}_n} + \boldsymbol{\Sigma}_{\hat{g}_n \hat{g}_{n-1}})$$

$$\boldsymbol{\Sigma}'_{\dot{\hat{g}}_n \dot{\hat{g}}_n} = \frac{1}{4\Delta t^2} \cdot (\boldsymbol{\Sigma}_{\hat{g}_{n+1} \hat{g}_{n+1}} - 2\boldsymbol{\Sigma}_{\hat{g}_{n+1} \hat{g}_{n-1}} + \boldsymbol{\Sigma}_{\hat{g}_{n-1} \hat{g}_{n-1}})$$

$$\boldsymbol{\Sigma}'_{\ddot{\hat{g}}_n \dot{\hat{g}}_n} = \frac{1}{2\Delta t^3} \cdot (\boldsymbol{\Sigma}_{\hat{g}_{n+1} \hat{g}_{n+1}} - 2\boldsymbol{\Sigma}_{\hat{g}_{n+1} \hat{g}_n} + 2\boldsymbol{\Sigma}_{\hat{g}_{n-1} \hat{g}_n} - \boldsymbol{\Sigma}_{\hat{g}_{n-1} \hat{g}_{n-1}})$$

$$\boldsymbol{\Sigma}'_{\ddot{\hat{g}}_n \ddot{\hat{g}}_n} = \frac{1}{\Delta t^4} \cdot (\boldsymbol{\Sigma}_{\hat{g}_{n+1} \hat{g}_{n+1}} - 4\boldsymbol{\Sigma}_{\hat{g}_{n+1} \hat{g}_n} + 2\boldsymbol{\Sigma}_{\hat{g}_{n+1} \hat{g}_{n-1}} + 4\boldsymbol{\Sigma}_{\hat{g}_n \hat{g}_n} - 4\boldsymbol{\Sigma}_{\hat{g}_n \hat{g}_{n-1}} + \boldsymbol{\Sigma}_{\hat{g}_{n-1} \hat{g}_{n-1}}), \tag{3.39}$$

which are used as a priori covariance matrices for the Kalman filter based state estimates.

### 3.2.3 Integer Ambiguity Resolution

While the state vector is updated in the Kalman filter epoch by epoch, the state estimate also includes an integer ambiguity resolution, which is done by first decorrelating the float ambiguity estimates, i.e.

$$\hat{\boldsymbol{N}}'^+ = \boldsymbol{Z}\hat{\boldsymbol{N}}^+, \tag{3.40}$$

and then sequentially fixing (bootstrapping) the decorrelated ones (see Henkel [1]). The integer ambiguity transformation $\boldsymbol{Z}$ of Teunissen [16] improves the reliability of bootstrapping. It is shown in a later section that the accuracy of phase bias estimation benefits a lot from having fixed the integer ambiguities.

The sequential ambiguity fixing was suggested by Blewitt in [17]. This conditional fixing takes the prior knowledge of the fixed ambiguities into account for the fixing of the remaining ambiguities, which are correlated for the difference between the fixed and float

estimates, i.e.

$$\hat{N}_{2|1} = \hat{N}_2 - \gamma \cdot \left( \hat{N}_1 - [\hat{N}_1] \right), \tag{3.41}$$

where $[\cdot]$ denotes the rounding, and $\gamma$ is chosen such that (see e.g. Teunissen [18])

$$\min_{\gamma} \sigma^2_{\hat{N}_{2|1}}. \tag{3.42}$$

By solving $\partial \sigma^2_{\hat{N}_{2|1}} / \partial \gamma = 0$, the optimal value of $\gamma$ is given by

$$\gamma_{\text{opt}} = \frac{\sigma_{\hat{N}_1 \hat{N}_2} - \sigma_{[\hat{N}_1] \hat{N}_2}}{\sigma^2_{\hat{N}_1} - 2\sigma_{\hat{N}_1 [\hat{N}_1]} + \sigma^2_{[\hat{N}_1]}}, \tag{3.43}$$

where the pseudo-covariances of the three discontinuous functions are traditionally approximated by zero, i.e. the terms $\sigma_{\hat{N}_1 [\hat{N}_1]}$, $\sigma^2_{[\hat{N}_1]}$ and $\sigma_{[\hat{N}_1] \hat{N}_2}$ are neglected, which will give the following equation:

$$\gamma = \sigma_{\hat{N}_2 \hat{N}_1} \sigma^{-2}_{\hat{N}_1}. \tag{3.44}$$

Replacing $\gamma$ in (3.41) by (3.44) yields in accordance with Teunissen [20]

$$\hat{N}_{2|1} = \hat{N}_2 - \sigma_{\hat{N}_2 \hat{N}_1} \sigma^{-2}_{\hat{N}_1} \cdot \left( \hat{N}_1 - [\hat{N}_1] \right), \tag{3.45}$$

which is uncorrelated to $\hat{N}_1$, i.e.

$$\sigma_{\hat{N}_1 \hat{N}_{2|1}} = 0. \tag{3.46}$$

The variance of $\hat{N}_{2|1}$ is obtained from (3.45):

$$\sigma^2_{\hat{N}_{2|1}} = \sigma^2_{\hat{N}_2} - \sigma^2_{\hat{N}_2 \hat{N}_1} \sigma^{-2}_{\hat{N}_1}. \tag{3.47}$$

Once the second ambiguity is conditionally fixed based on (3.45), the third one can be fixed similarly, i.e.

$$\hat{N}_{3|1,2} = \hat{N}_3 - \sigma_{\hat{N}_3 \hat{N}_1} \sigma^{-2}_{\hat{N}_1} \cdot \left( \hat{N}_1 - [\hat{N}_1] \right) - \sigma_{\hat{N}_3 \hat{N}_{2|1}} \sigma^{-2}_{\hat{N}_{2|1}} \cdot \left( \hat{N}_{2|1} - [\hat{N}_{2|1}] \right), \tag{3.48}$$

with the variance

$$\sigma^2_{\hat{N}_{3|1,2}} = \sigma^2_{\hat{N}_3} - \sigma^2_{\hat{N}_3 \hat{N}_1} \sigma^{-2}_{\hat{N}_1} - \sigma^2_{\hat{N}_3 \hat{N}_{2|1}} \sigma^{-2}_{\hat{N}_{2|1}}, \tag{3.49}$$

and the covariance between $\hat{N}_3$ and $\hat{N}_{2|1}$ being

$$\sigma_{\hat{N}_3 \hat{N}_{2|1}} = \sigma_{\hat{N}_3 \hat{N}_2} - \sigma_{\hat{N}_2 \hat{N}_1} \sigma^{-2}_{\hat{N}_1} \sigma_{\hat{N}_3 \hat{N}_1}. \tag{3.50}$$

Similarly, the covariances between the fourth ambiguity $\hat{N}_4$ and the previous conditional ones are calculated as

$$\sigma_{\hat{N}_4 \hat{N}_{2|1}} = \sigma_{\hat{N}_4 \hat{N}_2} - \sigma_{\hat{N}_2 \hat{N}_1} \sigma^{-2}_{\hat{N}_1} \sigma_{\hat{N}_4 \hat{N}_1}, \tag{3.51}$$

and

$$\sigma_{\hat{N}_4\hat{N}_{3|1,2}} = \sigma_{\hat{N}_4\hat{N}_3} - \sigma_{\hat{N}_3\hat{N}_1}\sigma_{\hat{N}_1}^{-2}\sigma_{\hat{N}_4\hat{N}_1} - \sigma_{\hat{N}_3\hat{N}_{2|1}}\sigma_{\hat{N}_{2|1}}^{-2}\sigma_{\hat{N}_4\hat{N}_{2|1}}. \tag{3.52}$$

In general, the $k$-th conditional ambiguity is given by

$$\hat{N}_{k|1,\dots,k-1} = \hat{N}_k - \sum_{j=1}^{k-1}\sigma_{\hat{N}_k\hat{N}_{j|1,\dots,j-1}}\sigma_{\hat{N}_{j|1,\dots,j-1}}^{-2}\left(\hat{N}_{j|1,\dots,j-1} - [\hat{N}_{j|1,\dots,j-1}]\right), \tag{3.53}$$

with the conditional variance

$$\sigma_{\hat{N}_{k|1,\dots,k-1}}^2 = \sigma_{\hat{N}_k}^2 - \sum_{j=1}^{k-1}\sigma_{\hat{N}_k\hat{N}_{j|1,\dots,j-1}}^2\sigma_{\hat{N}_{j|1,\dots,j-1}}^{-2}, \tag{3.54}$$

and the covariance between itself and the previous conditional ones

$$\sigma_{\hat{N}_k\hat{N}_{j|1,\dots,j-1}} = \sigma_{\hat{N}_k\hat{N}_j} - \sum_{i=1}^{j-1}\sigma_{\hat{N}_j\hat{N}_{i|1,\dots,i-1}}\sigma_{\hat{N}_{i|1,\dots,i-1}}^{-2}\sigma_{\hat{N}_k\hat{N}_{i|1,\dots,i-1}}, \tag{3.55}$$

with $j \in \{1,\dots,k-1\}$. Moreover, it can be shown from (3.54) that the cross-correlation between the conditional ambiguity estimates is zero, i.e.

$$\sigma_{\hat{N}_{k|1,\dots,k-1}\hat{N}_{j|1,\dots,j-1}} = 0 \quad \forall k \neq l \tag{3.56}$$

For simplicity, the $k$-th fixed conditional ambiguity is denoted by

$$\check{N}_{\mathrm{B}_k} = \left[\hat{N}_{k|1,\dots,k-1}\right]. \tag{3.57}$$

Thus, Eq. (3.54) can be rewritten in matrix-vector form as

$$\begin{bmatrix} \hat{N}_1 - \check{N}_{\mathrm{B}_1} \\ \hat{N}_2 - \check{N}_{\mathrm{B}_2} \\ \vdots \\ \hat{N}_K - \check{N}_{\mathrm{B}_K} \end{bmatrix} = \begin{bmatrix} 1 & 0 & \dots & 0 \\ \sigma_{\hat{N}_2\hat{N}_1}\sigma_{\hat{N}_1}^{-2} & 1 & \dots & 0 \\ \vdots & & \ddots & \vdots \\ \sigma_{\hat{N}_K\hat{N}_1}\sigma_{\hat{N}_1}^{-2} & \sigma_{\hat{N}_K\hat{N}_{2|1}}\sigma_{\hat{N}_{2|1}}^{-2} & \dots & 1 \end{bmatrix} \cdot \begin{bmatrix} \hat{N}_1 - \check{N}_{\mathrm{B}_1} \\ \hat{N}_{2|1} - \check{N}_{\mathrm{B}_2} \\ \vdots \\ \hat{N}_{K|1,\dots,K-1} - \check{N}_{\mathrm{B}_K} \end{bmatrix}. \tag{3.58}$$

Assuming deterministic $\check{N}_{\mathrm{B}_k}$, the covariance matrix $\Sigma_{\hat{N}}$ can be decomposed as

$$\Sigma_{\hat{N}} = \boldsymbol{L}\boldsymbol{D}\boldsymbol{L}^{\mathrm{T}}, \tag{3.59}$$

with

$$\boldsymbol{L} = \begin{bmatrix} 1 & 0 & \dots & 0 \\ \sigma_{\hat{N}_2\hat{N}_1}\sigma_{\hat{N}_1}^{-2} & 1 & \dots & 0 \\ \vdots & & \ddots & \vdots \\ \sigma_{\hat{N}_K\hat{N}_1}\sigma_{\hat{N}_1}^{-2} & \sigma_{\hat{N}_K\hat{N}_{2|1}}\sigma_{\hat{N}_{2|1}}^{-2} & \dots & 1 \end{bmatrix}, \tag{3.60}$$

and the diagonal matrix

$$
\boldsymbol{D} = \begin{bmatrix} \sigma^2_{\hat{N}_1} & & & \\ & \sigma^2_{\hat{N}_{2|1}} & & \\ & & \ddots & \\ & & & \sigma^2_{\hat{N}_{K|1,\ldots,K-1}} \end{bmatrix}.
\tag{3.61}
$$

For correct $\breve{N}_{\mathrm{B}_k}$, Teunissen computed the biases in the conditional ambiguities from the the biases in the float ambiguities [19], i.e.

$$
\begin{bmatrix} b_{\hat{N}_1} \\ b_{\hat{N}_{2|1}} \\ \vdots \\ b_{\hat{N}_{K|1,\ldots,K-1}} \end{bmatrix} = \boldsymbol{L}^{-1} \cdot \begin{bmatrix} b_{\hat{N}_1} \\ b_{\hat{N}_2} \\ \vdots \\ b_{\hat{N}_K} \end{bmatrix}.
\tag{3.62}
$$

The conditional variances and biases are used to compute the success rate of the sequential ambiguity resolution, i.e.

$$
P_s = \prod_{k=1}^{K} \int_{-0.5}^{+0.5} \frac{1}{\sqrt{2\pi\sigma^2_{\hat{N}_{k|1,\ldots,k-1}}}} \cdot \exp\left(-\frac{(\hat{N}_{k|1,\ldots,k-1} - b_{\hat{N}_{k|1,\ldots,k-1}})^2}{2\sigma^2_{\hat{N}_{k|1,\ldots,k-1}}}\right) d\hat{N}_{k|1,\ldots,k-1}
\tag{3.63}
$$

However, the exact evaluation of $\hat{N}_{2|1}$ in (3.41) requires the terms $\sigma_{\hat{N}_1[\hat{N}_1]}$, $\sigma^2_{[\hat{N}_1]}$ and $\sigma_{[\hat{N}_1]\hat{N}_2}$ to be considered in $\gamma_{\mathrm{opt}}$ in (3.43). The derivation of the three terms is shown as follows. First, the errors in the float ambiguity estimates are introduced as

$$
\varepsilon_{\hat{N}_1} = \hat{N}_1 - N_1, \quad \varepsilon_{\hat{N}_2} = \hat{N}_2 - N_2,
\tag{3.64}
$$

which are zero mean Gaussian distributed with the probability density functions $f(\varepsilon_{\hat{N}_1})$ and $f(\varepsilon_{\hat{N}_2})$, and the joint probability density function $f(\varepsilon_{\hat{N}_1}, \varepsilon_{\hat{N}_2})$ being

$$
f(\varepsilon_{\hat{N}_1}, \varepsilon_{\hat{N}_2}) = \frac{1}{2\pi\sqrt{|\Sigma|}} e^{-\frac{1}{2}\begin{bmatrix} \varepsilon_{\hat{N}_1} \\ \varepsilon_{\hat{N}_2} \end{bmatrix}^{\mathrm{T}} \Sigma^{-1} \begin{bmatrix} \varepsilon_{\hat{N}_1} \\ \varepsilon_{\hat{N}_2} \end{bmatrix}},
\tag{3.65}
$$

with

$$
\Sigma = \begin{bmatrix} \sigma^2_{\hat{N}_1} & \sigma_{\hat{N}_1\hat{N}_2} \\ \sigma_{\hat{N}_1\hat{N}_2} & \sigma^2_{\hat{N}_2} \end{bmatrix}.
\tag{3.66}
$$

The three pseudo-covariances are calculated as

$$
\begin{aligned}
\sigma_{\hat{N}_1[\hat{N}_1]} &= \int_{-\infty}^{+\infty} \varepsilon_{\hat{N}_1}[\varepsilon_{\hat{N}_1}] f(\varepsilon_{\hat{N}_1}) d\varepsilon_{\hat{N}_1} \\
&= \sum_{k=-\infty}^{+\infty} k \int_{k-0.5}^{k+0.5} \varepsilon_{\hat{N}_1} f(\varepsilon_{\hat{N}_1}) d\varepsilon_{\hat{N}_1} \\
&= \frac{1}{\sqrt{2\pi}} \cdot \sum_{k=-\infty}^{+\infty} k \left( e^{-\frac{(k-0.5)^2}{2\sigma_{\hat{N}_1}^2}} - e^{-\frac{(k+0.5)^2}{2\sigma_{\hat{N}_1}^2}} \right)
\end{aligned}
\tag{3.67}
$$

$$
\begin{aligned}
\sigma_{[\hat{N}_1]}^2 &= \int_{-\infty}^{+\infty} \left([\varepsilon_{\hat{N}_1}]\right)^2 f(\varepsilon_{\hat{N}_1}) d\varepsilon_{\hat{N}_1} \\
&= \sum_{k=-\infty}^{+\infty} k^2 \cdot \int_{k-0.5}^{k+0.5} f(\varepsilon_{\hat{N}_1}) d\varepsilon_{\hat{N}_1} \\
&= \sum_{k=-\infty}^{+\infty} k^2 \cdot \left( \Phi\left(\frac{k+0.5}{\sigma_{\hat{N}_1}}\right) - \Phi\left(\frac{k-0.5}{\sigma_{\hat{N}_1}}\right) \right)
\end{aligned}
\tag{3.68}
$$

$$
\begin{aligned}
\sigma_{[\hat{N}_1]\hat{N}_2} &= \int_{-\infty}^{+\infty} \int_{-\infty}^{+\infty} [\varepsilon_{\hat{N}_1}] \varepsilon_{\hat{N}_2} f(\varepsilon_{\hat{N}_1}, \varepsilon_{\hat{N}_2}) d\varepsilon_{\hat{N}_1} \\
&= \sum_{k=-\infty}^{+\infty} k \cdot \int_{k-0.5}^{k+0.5} \int_{-\infty}^{+\infty} \varepsilon_{\hat{N}_2} f(\varepsilon_{\hat{N}_1}, \varepsilon_{\hat{N}_2}) d\varepsilon_{\hat{N}_2} d\varepsilon_{\hat{N}_1}.
\end{aligned}
\tag{3.69}
$$

Applying Eq.(3.65) in (3.69) yields

$$
\begin{aligned}
\sigma_{[\hat{N}_1]\hat{N}_2} &= \sum_{k=-\infty}^{+\infty} k \cdot \int_{k-0.5}^{k+0.5} \int_{-\infty}^{+\infty} \varepsilon_{\hat{N}_2} \cdot \frac{1}{2\pi\sqrt{|\Sigma|}} e^{-\frac{1}{2|\Sigma|}\left( \sigma_{\hat{N}_1}^2 \varepsilon_{\hat{N}_2}^2 - 2\sigma_{\hat{N}_1\hat{N}_2} \varepsilon_{\hat{N}_1} \varepsilon_{\hat{N}_2} + \sigma_{\hat{N}_2}^2 \varepsilon_{\hat{N}_1}^2 \right)} d\varepsilon_{\hat{N}_2} d\varepsilon_{\hat{N}_1} \\
&= \sum_{k=-\infty}^{+\infty} k \cdot \int_{k-0.5}^{k+0.5} \int_{-\infty}^{+\infty} \varepsilon_{\hat{N}_2} \cdot \frac{1}{2\pi\sqrt{|\Sigma|}} e^{-\frac{\sigma_{\hat{N}_1}^2}{2|\Sigma|}\left( \varepsilon_{\hat{N}_2} - \frac{\sigma_{\hat{N}_1\hat{N}_2}}{\sigma_{\hat{N}_1}^2} \varepsilon_{\hat{N}_1} \right)^2 + \frac{\sigma_{\hat{N}_1\hat{N}_2}^2 - \sigma_{\hat{N}_1}^2 \sigma_{\hat{N}_2}^2}{2\sqrt{|\Sigma|}\cdot\sigma_{\hat{N}_1}^2}} d\varepsilon_{\hat{N}_2} d\varepsilon_{\hat{N}_1} \\
&= \frac{1}{2\pi\sqrt{|\Sigma|}} \sum_{k=-\infty}^{+\infty} k \cdot \int_{k-0.5}^{k+0.5} e^{-\frac{\varepsilon_{\hat{N}_1}^2}{2\sigma_{\hat{N}_1}^2}} \int_{-\infty}^{+\infty} \varepsilon_{\hat{N}_2} e^{-\frac{\sigma_{\hat{N}_1}^2}{2|\Sigma|}\left( \varepsilon_{\hat{N}_2} - \frac{\sigma_{\hat{N}_1\hat{N}_2}}{\sigma_{\hat{N}_1}^2} \varepsilon_{\hat{N}_1} \right)^2} d\varepsilon_{\hat{N}_2} d\varepsilon_{\hat{N}_1}.
\end{aligned}
\tag{3.70}
$$

By using the expansion

$$
\varepsilon_{\hat{N}_2} = \left( \varepsilon_{\hat{N}_2} - \frac{\sigma_{\hat{N}_1\hat{N}_2}}{\sigma_{\hat{N}_1}^2} \varepsilon_{\hat{N}_1} \right) + \frac{\sigma_{\hat{N}_1\hat{N}_2}}{\sigma_{\hat{N}_1}^2} \varepsilon_{\hat{N}_1},
\tag{3.71}
$$

and simplifying the integral parameter by the substitution

$$
x \triangleq \varepsilon_{\hat{N}_2} - \frac{\sigma_{\hat{N}_1\hat{N}_2}}{\sigma_{\hat{N}_1}^2} \varepsilon_{\hat{N}_1},
\tag{3.72}
$$

the inner integral can be calculated as

$$
\int_{-\infty}^{+\infty} \varepsilon_{\hat{N}_2} e^{-\frac{\sigma_{\hat{N}_1}^2}{2|\Sigma|}\left(\varepsilon_{\hat{N}_2}-\frac{\sigma_{\hat{N}_1\hat{N}_2}}{\sigma_{\hat{N}_1}^2}\varepsilon_{\hat{N}_1}\right)^2} d\varepsilon_{\hat{N}_2} = \int_{-\infty}^{+\infty} x e^{-\frac{\sigma_{\hat{N}_1}^2}{2|\Sigma|}x^2} dx + \int_{-\infty}^{+\infty} \frac{\sigma_{\hat{N}_1\hat{N}_2}}{\sigma_{\hat{N}_1}^2}\varepsilon_{\hat{N}_1} e^{-\frac{\sigma_{\hat{N}_1}^2}{2|\Sigma|}x^2} dx
$$

$$
= 0 + \int_{-\infty}^{+\infty} \frac{\sigma_{\hat{N}_1\hat{N}_2}}{\sigma_{\hat{N}_1}^2}\varepsilon_{\hat{N}_1} \sqrt{2\pi\frac{|\Sigma|}{\sigma_{\hat{N}_1}^2}} \frac{1}{\sqrt{2\pi\frac{|\Sigma|}{\sigma_{\hat{N}_1}^2}}} e^{-\frac{x^2}{2\frac{|\Sigma|}{\sigma_{\hat{N}_1}^2}}} dx
$$

$$
= \frac{\sigma_{\hat{N}_1\hat{N}_2}}{\sigma_{\hat{N}_1}^2} \sqrt{2\pi\frac{|\Sigma|}{\sigma_{\hat{N}_1}^2}} \cdot \varepsilon_{\hat{N}_1}. \tag{3.73}
$$

Thus, (3.70) can be further developed as

$$
\begin{aligned}
\sigma_{[\hat{N}_1]\hat{N}_2} &= \frac{1}{2\pi\sqrt{|\Sigma|}} \sum_{k=-\infty}^{+\infty} k \cdot \int_{k-0.5}^{k+0.5} \frac{\sigma_{\hat{N}_1\hat{N}_2}}{\sigma_{\hat{N}_1}^2} \sqrt{2\pi\frac{|\Sigma|}{\sigma_{\hat{N}_1}^2}} \cdot \varepsilon_{\hat{N}_1} e^{-\frac{\varepsilon_{\hat{N}_1}^2}{2\sigma_{\hat{N}_1}^2}} d\varepsilon_{\hat{N}_1} \\
&= \frac{1}{2\pi\sqrt{|\Sigma|}} \frac{\sigma_{\hat{N}_1\hat{N}_2}}{\sigma_{\hat{N}_1}^2} \sqrt{2\pi\frac{|\Sigma|}{\sigma_{\hat{N}_1}^2}} \sum_{k=-\infty}^{+\infty} k \cdot \int_{k-0.5}^{k+0.5} \varepsilon_{\hat{N}_1} e^{-\frac{\varepsilon_{\hat{N}_1}^2}{2\sigma_{\hat{N}_1}^2}} d\varepsilon_{\hat{N}_1} \\
&= \frac{1}{2\pi\sqrt{|\Sigma|}} \frac{\sigma_{\hat{N}_1\hat{N}_2}}{\sigma_{\hat{N}_1}^2} \sqrt{2\pi\frac{|\Sigma|}{\sigma_{\hat{N}_1}^2}} \sum_{k=-\infty}^{+\infty} k \cdot (-\sigma_{\hat{N}_1}^2) \cdot \left( e^{-\frac{(k+0.5)^2}{2\sigma_{\hat{N}_1}^2}} - e^{-\frac{(k-0.5)^2}{2\sigma_{\hat{N}_1}^2}} \right) \\
&= -\frac{\sigma_{\hat{N}_1\hat{N}_2}}{2\pi\sigma_{\hat{N}_1}^2} \sum_{k=-\infty}^{+\infty} k \left( e^{-\frac{(k+0.5)^2}{2\sigma_{\hat{N}_1}^2}} - e^{-\frac{(k-0.5)^2}{2\sigma_{\hat{N}_1}^2}} \right),
\end{aligned} \tag{3.74}
$$

where the infinite sum can be well approximated by a finite sum over $|k| < 10$. It is noted from the results that, the pseudo-covariance term $\sigma_{[\hat{N}_1]\hat{N}_2}$ is independent from the noise variance $\sigma_{\hat{N}_2}^2$ of the second ambiguity.

Fig. 3.2 shows the optimal weighting $\gamma_{\mathrm{opt}}$ of (3.43) for bootstrapping. The additional consideration of the fixing errors in $[\hat{N}_1]$ results in a smaller weight than the traditional $\gamma = \sigma_{\hat{N}_2\hat{N}_1}\sigma_{\hat{N}_1}^{-2}$, which equals the cross-correlation coefficient $\rho$ if the variances for $\hat{N}_1$ and $\hat{N}_2$ are assumed to be the same. If the fixing error in the first ambiguity is larger, a lower weight of $\gamma$ is necessary, which results in a lower probability of wrong fixing.

After the fixing of the second ambiguity, the exact calculation for the third conditional one can be derived by finding the optimal $\gamma_1$ and $\gamma_2$ in the following equation

$$
\hat{N}_{3|1,2} = \hat{N}_3 - \gamma_1 \cdot \left( \hat{N}_1 - [\hat{N}_1] \right) - \gamma_2 \cdot \left( \hat{N}_{2|1} - [\hat{N}_{2|1}] \right), \tag{3.75}
$$

such that

$$
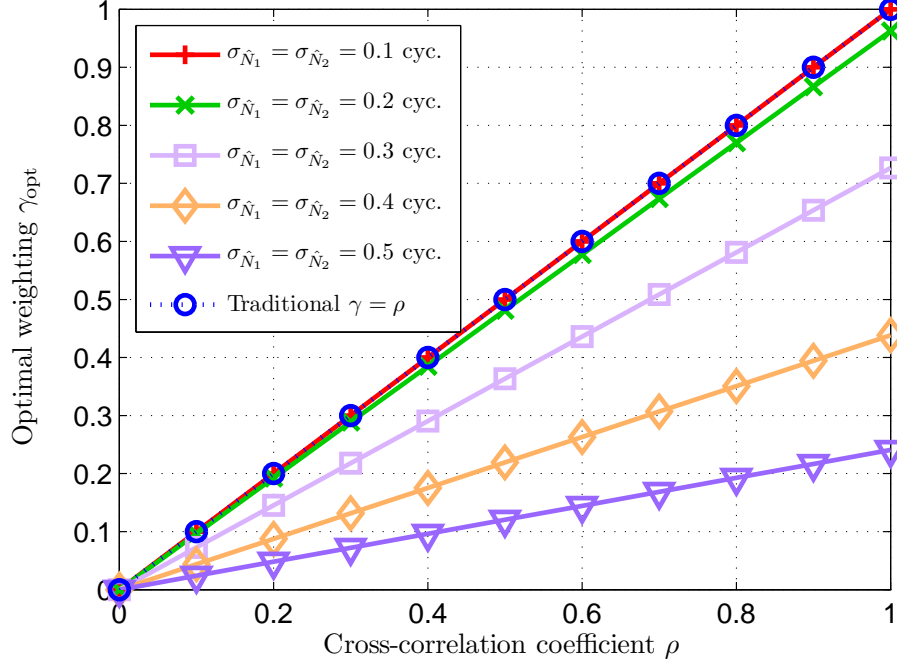\min_{\gamma_1, \gamma_2} \sigma_{\hat{N}_{3|1,2}}. \tag{3.76}
$$

Fig. 3.2: Optimal weighting $\gamma_{\mathrm{opt}}$ for bootstrapping with respect to the cross-correlation coefficient $\rho = \sigma_{\hat{N}_1 \hat{N}_2}/(\sigma_{\hat{N}_1} \sigma_{\hat{N}_2})$: The additional consideration of the fixing errors in $[\hat{N}_1]$ results in a smaller weight than the traditional $\gamma = \sigma_{\hat{N}_2 \hat{N}_1} \sigma_{\hat{N}_1}^{-2}$, which corresponds to the cross-correlation coefficient between $\hat{N}_1$ and $\hat{N}_2$ for equal variances.

Since $\hat{N}_1$ and $\hat{N}_{2|1}$ are uncorrelated, the solution to (3.76) is given by

$$
\begin{aligned}
\gamma_1 &= \frac{\sigma_{\hat{N}_3 \hat{N}_1} - \sigma_{\hat{N}_3 [\hat{N}_1]}}{\sigma_{\hat{N}_1}^2 - 2\sigma_{\hat{N}_1 [\hat{N}_1]} + \sigma_{[\hat{N}_1]}^2}, \\
\gamma_2 &= \frac{\sigma_{\hat{N}_3 \hat{N}_{2|1}} - \sigma_{\hat{N}_3 [\hat{N}_{2|1}]}}{\sigma_{\hat{N}_{2|1}}^2 - 2\sigma_{\hat{N}_{2|1} [\hat{N}_{2|1}]} + \sigma_{[\hat{N}_{2|1}]}^2}.
\end{aligned}
\tag{3.77}
$$

which solves Eq. (3.75), i.e.

$$
\hat{N}_{3|1,2} = \hat{N}_3 - \frac{\sigma_{\hat{N}_3 \hat{N}_1} - \sigma_{\hat{N}_3 [\hat{N}_1]}}{\sigma_{\hat{N}_1}^2 - 2\sigma_{\hat{N}_1 [\hat{N}_1]} + \sigma_{[\hat{N}_1]}^2} \cdot \left( \hat{N}_1 - [\hat{N}_1] \right) - \frac{\sigma_{\hat{N}_3 \hat{N}_{2|1}} - \sigma_{\hat{N}_3 [\hat{N}_{2|1}]}}{\sigma_{\hat{N}_{2|1}}^2 - 2\sigma_{\hat{N}_{2|1} [\hat{N}_{2|1}]} + \sigma_{[\hat{N}_{2|1}]}^2} \cdot \left( \hat{N}_{2|1} - [\hat{N}_{2|1}] \right).
\tag{3.78}
$$

The exact expression for the k-th conditional ambiguity is given by

$$
\hat{N}_{k|1,\ldots,k-1} = \hat{N}_k - \sum_{j=1}^{k-1} \gamma_j \left( \hat{N}_{j|1,\ldots,j-1} - [\hat{N}_{j|1,\ldots,j-1}] \right),
\tag{3.79}
$$

with

$$\gamma_j = \frac{\sigma_{\hat{N}_k \hat{N}_{j|1,\ldots,j-1}} - \sigma_{\hat{N}_k [\hat{N}_{j|1,\ldots,j-1}]}}{\sigma^2_{\hat{N}_{j|1,\ldots,j-1}} - 2\sigma_{\hat{N}_{j|1,\ldots,j-1}[\hat{N}_{j|1,\ldots,j-1}]} + \sigma^2_{[\hat{N}_{j|1,\ldots,j-1}]}}.$$

Eq. (3.79) simplifies to Eq. (3.53) if the pseudo-covariance terms $\sigma_{\hat{N}_k[\hat{N}_{j|1,\ldots,j-1}]}$, $\sigma_{\hat{N}_{j|1,\ldots,j-1}[\hat{N}_{j|1,\ldots,j-1}]}$ and $\sigma^2_{[\hat{N}_{j|1,\ldots,j-1}]}$ are approved by 0.

Integer bootstrapping can be visualized graphically by introducing the concept of pull-in regions. Let the map $S$ represent the mapping from $n$-dimensional float ambiguities to $n$-dimensional integer ambiguities, i.e. $\mathbb{R}^n \mapsto \mathbb{Z}^n$, and therefore the map $S$ is a "many-to-one" map instead of "one-to-one" map. The following subset $S_{\check{\boldsymbol{N}}_k}$ defines a subset of float ambiguities $\hat{\boldsymbol{N}}$ that could be mapped to the integer ambiguity $\check{\boldsymbol{N}}_k$, and the subset is referred to as the pull-in region of $\check{\boldsymbol{N}}_k$ [20].

$$S_{\check{\boldsymbol{N}}_k} = \left\{ \hat{\boldsymbol{N}} \in \mathbb{R}^n \ \middle| \ \check{\boldsymbol{N}}_k = S(\hat{\boldsymbol{N}}) \right\}, \quad \check{\boldsymbol{N}}_k \in \mathbb{Z}^n, \tag{3.80}$$

where $\check{\boldsymbol{N}}_k$ denotes the integer estimator, i.e. $\check{\boldsymbol{N}}_k = S(\hat{\boldsymbol{N}}_k)$.

The integer estimator is said to be admissible [20] when the pull-in regions $S_{\check{\boldsymbol{N}}_k}$ satisfy

$$\begin{aligned}
&(1) \quad \cup S_{\check{\boldsymbol{N}}_k} = \mathbb{R}^n, \quad \forall \check{\boldsymbol{N}}_k \in \mathbb{Z}^n \\
&(2) \quad S_{\check{\boldsymbol{N}}_{k_1}} \cap S_{\check{\boldsymbol{N}}_{k_2}} = \emptyset, \quad \forall \check{\boldsymbol{N}}_{k_1}, \check{\boldsymbol{N}}_{k_2} \in \mathbb{Z}^n, \ \check{\boldsymbol{N}}_{k_1} \neq \check{\boldsymbol{N}}_{k_2} \\
&(3) \quad S_{\check{\boldsymbol{N}}_k} = S_{\boldsymbol{0}} + \check{\boldsymbol{N}}_k,
\end{aligned} \tag{3.81}$$

where the first constraint ensures that the subset $S_{\check{\boldsymbol{N}}_k}$ cover the whole real-valued region, and the second constraint ensures no overlapping of the pull-in regions, i.e. combining the first two constraints ensures that every float vector is mapped to one and only one integer vector. The third constraint is referred to the shifting property i.e. it is sufficient to consider only the fractional part of the float ambiguity estimates.

The simplest integer estimator is instantaneous rounding, which can be used to describe the pull-in regions

$$S_{\text{R},\check{\boldsymbol{N}}_k} = \left\{ \hat{\boldsymbol{N}} \in \mathbb{R}^n \ \middle| \ \left| \hat{\boldsymbol{N}} - \check{\boldsymbol{N}}_k \right| \leq \frac{1}{2} \right\}, \quad \check{\boldsymbol{N}}_k \in \mathbb{Z}^n. \tag{3.82}$$

The pull-in regions of the bootstrapped ambiguity estimator are given by

$$S_{\text{B},\check{\boldsymbol{N}}_k} = \left\{ \hat{\boldsymbol{N}} \in \mathbb{R}^n \ \middle| \ \left| \boldsymbol{c}_i^{\text{T}} \boldsymbol{L}^{-1}(\hat{\boldsymbol{N}} - \check{\boldsymbol{N}}_k) \right| \leq \frac{1}{2}, \ i = 1, \ldots, n \right\}, \quad \check{\boldsymbol{N}}_k \in \mathbb{Z}^n, \tag{3.83}$$

where $\boldsymbol{c}_i = [0, \ldots, 0, 1, 0, \ldots, 0]^{\text{T}}$ having a 1 at its $i$-th entry, and $\boldsymbol{L}$ is given by (3.60).

The first two constraints of (3.81) can be easily verified using the definition of the boot-strapped estimator. To verify the third constraint, Eq. (3.83) can be derived as

$$
\begin{aligned}
S_{B,\check{N}_k} &= \left\{ \hat{N} \in \mathbb{R}^n \;\middle|\; \left| c_i^T L^{-1}(\hat{N} - \check{N}_k) \right| \leq \frac{1}{2}, \; i = 1, \ldots, n \right\} \\
&= \left\{ \hat{N} \in \mathbb{R}^n \;\middle|\; \left| c_i^T L^{-1}\hat{\check{N}} \right| \leq \frac{1}{2}, \; \hat{\check{N}} = \hat{N} - \check{N}_k, \; i = 1, \ldots, n \right\} \\
&= S_{B,0} + \check{N}_k,
\end{aligned}
\tag{3.84}
$$

which indicates that all pull-in regions are shifted copies of $S_{B,0}$ and all of them have the same shape and volume. The volume of the pull-in regions can be shown to be 1. Consider the linear transformation $\hat{\tilde{N}} - \tilde{N} = L^{-1}(\hat{N} - N)$, which provides the set of conditional ambiguity

$$
\begin{aligned}
S_{B,\tilde{N}} &= \left\{ \hat{N} \in \mathbb{R}^n \;\middle|\; \left| c_i^T L^{-1}(\hat{N} - N) \right| \leq \frac{1}{2}, \; i = 1, \ldots, n \right\} \\
&= \left\{ \hat{\tilde{N}} \in \mathbb{R}^n \;\middle|\; \left| c_i^T \left( \hat{\tilde{N}} - \tilde{N} \right) \right| \leq \frac{1}{2}, \; \hat{\tilde{N}} - \tilde{N} = L^{-1}(\hat{N} - N), \; i = 1, \ldots, n \right\},
\end{aligned}
\tag{3.85}
$$

which represents an $n$-dimensional unit cube centered at the origin. Since the volume of the unit cube is 1, and the determinant of the unit lower triangular matrix $L$ is 1, thus the volume of $S_{B,0}$ must also equal 1.

To better understand the shape of the pull-in regions, the two-dimensional case is first considered. The matrix $L$ is simplified to

$$
L = \begin{bmatrix} 1 & 0 \\ l_1 & 1 \end{bmatrix},
\tag{3.86}
$$

with $l_1 = \sigma_{\hat{N}_2 \hat{N}_1} \sigma_{\hat{N}_1}^{-2}$.

Then, only the subset $S_{B,0}$ which is centered at the origin is considered according to the shift property in (3.81), i.e.

$$
\begin{aligned}
S_{B,N} &= \left\{ \hat{N} \in \mathbb{R}^2 \;\middle|\; \left| c_i^T L^{-1}(\hat{N} - N) \right| \leq \frac{1}{2}, \; i = 1, 2 \right\} \\
&= \left\{ \hat{N} \in \mathbb{R}^2 \;\middle|\; \left| (\hat{N}_1 - N_1) \right| \leq \frac{1}{2}, \; \text{and} \; \left| (\hat{N}_2 - N_2) - l_1(\hat{N}_1 - N_1) \right| \leq \frac{1}{2} \right\},
\end{aligned}
\tag{3.87}
$$

which shows the pull-in region is bounded by four lines $\hat{N}_1 - N_1 = \frac{1}{2}$, $\hat{N}_1 - N_1 = -\frac{1}{2}$, $\hat{N}_2 - N_2 = l_1(\hat{N}_1 - N_1) + \frac{1}{2}$, and $(\hat{N}_2 - N_2) = l_1(\hat{N}_1 - N_1) - \frac{1}{2}$. Thus the shape of the

two-dimensional pull-in region is a parallelogram, and its slope is governed by $\sigma_{\hat{N}_2 \hat{N}_1} \sigma_{\hat{N}_1}^{-2}$. If the two ambiguities are uncorrelated, i.e. $\sigma_{\hat{N}_2 \hat{N}_1} = 0$, the parallelogram turns into a unit square, and the bootstrapped estimator becomes simply instantaneous rounding. Fig. 3.3 shows an example of the ambiguity error ellipse and the two-dimensional pull-in regions of instantaneous rounding and integer bootstrapping, the areas of which are both equal to 1.
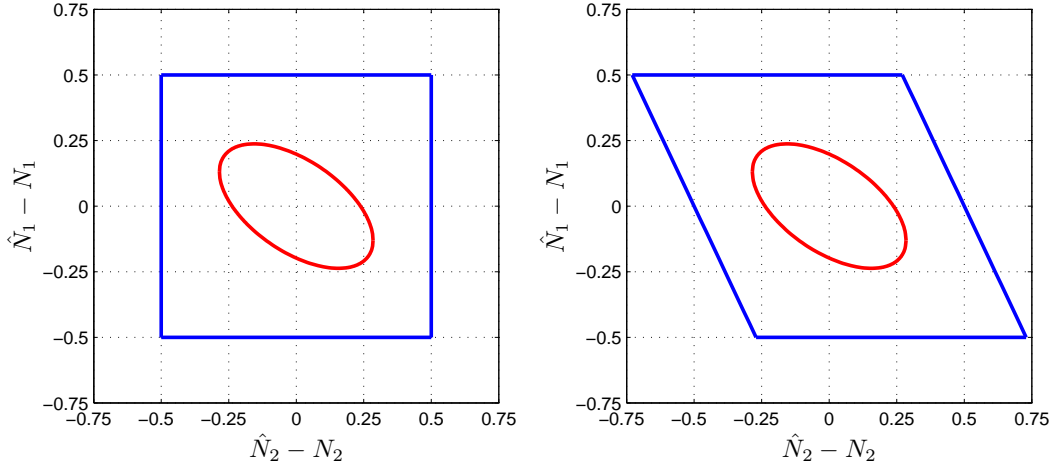


Fig. 3.3: The ambiguity error ellipse and the two-dimensional pull-in regions of instantaneous rounding (on the left) and integer bootstrapping (on the right).

For the three-dimensional case,

$$\boldsymbol{L} = \begin{bmatrix} 1 & 0 & 0 \\ l_1 & 1 & 0 \\ l_2 & l_3 & 1 \end{bmatrix}, \tag{3.88}$$

with

$$l_1 = \sigma_{\hat{N}_2 \hat{N}_1} \sigma_{\hat{N}_1}^{-2}, \quad l_2 = \sigma_{\hat{N}_3 \hat{N}_1} \sigma_{\hat{N}_1}^{-2}, \quad l_3 = \sigma_{\hat{N}_3 \hat{N}_{2|1}}. \tag{3.89}$$

The subset $S_{\mathrm{B},\boldsymbol{N}}$ can be developed as

$$
\begin{aligned}
S_{\mathrm{B},\boldsymbol{N}} &= \left\{ \hat{\boldsymbol{N}} \in \mathbb{R}^3 \;\middle|\; \left| \boldsymbol{c}_i^{\mathrm{T}} \boldsymbol{L}^{-1} \left( \hat{\boldsymbol{N}} - \boldsymbol{N} \right) \right| \leq \frac{1}{2},\; i = 1,2,3 \right\} \\
&= \left\{ \hat{\boldsymbol{N}} \in \mathbb{R}^3 \;\middle|\; \left| \boldsymbol{c}_i^{\mathrm{T}} \begin{bmatrix} 1 & 0 & 0 \\ -l_1 & 1 & 0 \\ l_1 l_3 - l_2 & -l_3 & 1 \end{bmatrix} \left( \hat{\boldsymbol{N}} - \boldsymbol{N} \right) \right| \leq \frac{1}{2},\; i = 1,2,3 \right\} \\
&= \left\{ \hat{\boldsymbol{N}} \in \mathbb{R}^3 \;\middle|\; \left| (\hat{N}_1 - N_1) \right| \leq \frac{1}{2},\; \text{and } \left| (\hat{N}_2 - N_2) - l_1(\hat{N}_1 - N_1) \right| \leq \frac{1}{2},\; \text{and} \right. \\
&\qquad \left. \left| (l_1 l_3 - l_2)(\hat{N}_1 - N_1) - l_3(\hat{N}_2 - N_2) + (\hat{N}_3 - N_3) \right| \leq \frac{1}{2} \right\}, (3.90)
\end{aligned}
$$

which shows that the intersection of the three dimensional pull-in region with the $(\hat{N}_1 - N_1)(\hat{N}_2 - N_2)$-plane remains a parallelogram, while the constraint on the third axis shows the region is bounded by parallel planes, and thus the region becomes a parallelepiped. Fig. 3.4 shows two examples of the three dimensional pull-in regions and the ambiguity ellipsoid. The shape is determined by the covariance matrix $\Sigma_{\hat{N}}$ and the volume is 1. Moreover, the ambiguities are fixed in different orders in the two subfigures. The optimum ambiguity fixing order shall start from the most accurate estimate of ambiguities.
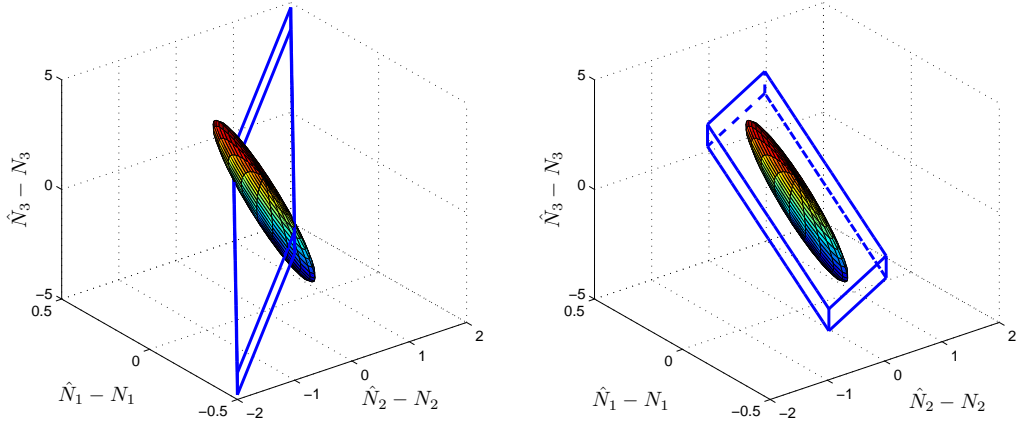


Fig. 3.4: Examples of the ambiguity ellipsoid and the parallelepiped shape of the three-dimensional pull-in regions of integer bootstrapping, which is bounded by six faces of parallelograms. The volumes of the pull-in regions are 1. The optimum ambiguity fixing order shall start from the most accurate estimate of ambiguities.

# 3.3 Simulation Results

## 3.3.1 Benefit of Ambiguity resolution

Fig. 3.5 shows the temporal evolution of the probability of wrong fixing and the achievable accuracies of receiver and satellite phase bias estimates, with simulated E1 and E5 measurements from a network of $R = 20$ reference stations and $K_r = 10$ $(r \in \{1, \ldots, R\})$ visible satellites for each station. The state vector containing ranges, range rates, ionospheric delays, integer ambiguities, receiver and satellite phase biases, is estimated in two steps with Kalman filtering. It is initialized by a least-squares estimation from measurements of two epochs (Henkel et al. [6]). The float ambiguities can be decorrelated and sequentially fixed after 200 epochs, with an error rate of less than $10^{-9}$. The later process of Kalman filtering benefits much from the ambiguity fixing, thus leads to 5 mm accuracy after 1000 epochs, i.e. less than 2 minutes for a 10 Hz receiver. The amplitude of the process noise has been characterized by $S_p = 1((\text{m/s})^2)/s$ for ranges and range rates, and $\sigma_I = 1\text{cm}$ for ionospheric delays, i.e. no process noise is assumed for the biases. It is noted that the achievable accuracy does not depend on satellite geometry, since the bias estimation is performed on range domain.

Fig. 3.6 shows the benefit of a large network of reference stations for bias estimation. The impact of the network size $R$ on the achievable accuracies becomes visible as soon as the integer ambiguities are fixed after 200 epochs. Obviously, the gain in the bias estimation due to fixing depends on $R$ and increases for larger networks due to the additional redundancy. The estimation of E5 satellite biases with 1cm standard deviation requires 325 epochs for 20 reference stations, 750 epochs for 16 stations, and several thousands of epochs for 2 stations.

## 3.3.2 Benefit of a Third Frequency

Fig. 3.7 shows the benefit of measurements on a third frequency for bias estimation. Dual frequency E1-E5a and triple frequency E1-E5a-E5b code and carrier phase measurements of $R = 20$ reference stations and $K_r = 10$ satellites are simulated for the estimation of the ranges, range rates, ionospheric delays, integer ambiguities, receiver and satellite phase biases. If no ambiguities are fixed, the impact of the third frequency for bias estimation remains negligible. However, the redundancy given by the third frequency enables an almost three times earlier ambiguity fixing, and thus, a higher accuracy of
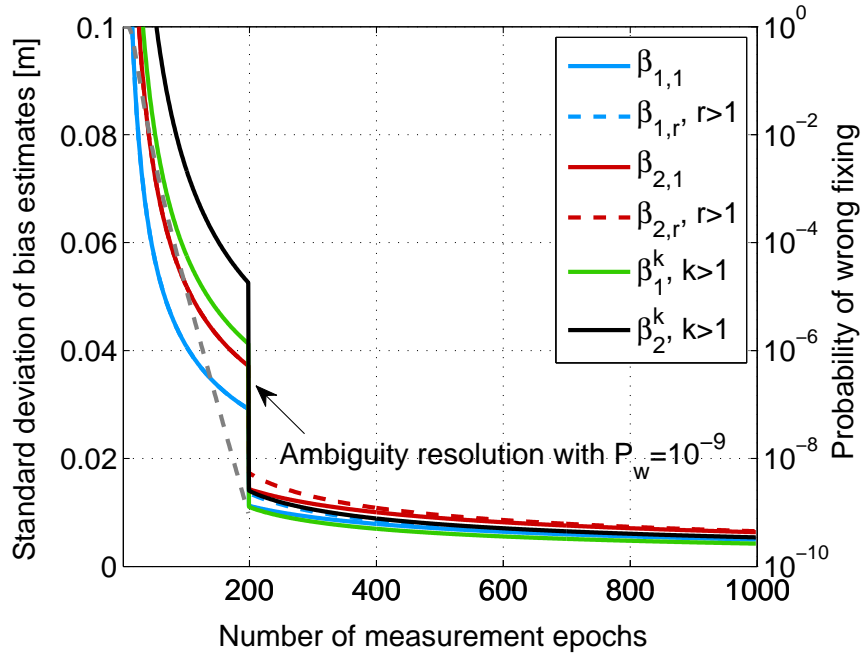
Fig. 3.5: Achievable accuracies of receiver and satellite phase bias estimation with a Kalman filter: A network of $R = 20$ reference stations with $K_r = 10$ satellites has been simulated: The float ambiguities are decorrelated and sequentially fixed after 200 epochs with a probability of wrong fixing of less than $10^{-9}$, which is shown in gray dashed line. The fixing reduces the standard deviations of the bias estimates by a factor between 3 and 4.

the bias estimates. The code biases on the third frequency are estimated with a high accuracy as the code biases on the first two frequencies have been absorbed by the ranges and ionospheric delays.

Fig. 3.8 shows the achievable accuracies for the satellite phase and code bias estimates for the same scenario. The satellite biases can be estimated with a slightly higher accuracy than the receiver biases after the ambiguity fixing due to $R > K$. If no ambiguities are fixed, the receiver bias estimation benefits from the absorption of one satellite bias by the receiver biases.
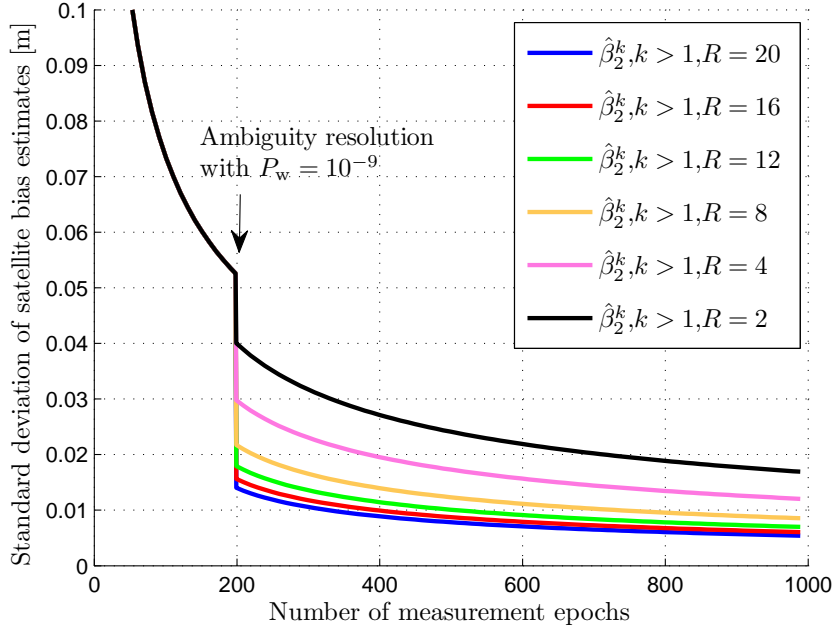
Fig. 3.6: Benefit of large network of reference stations for bias estimation: The fixing of ambiguities enables an improvement of bias estimation by a factor of 4 for $R = 20$. The same scenario has been assumed for Fig. 3.5, i.e. simulated measurements on E1 and E5 from a network of $R$ reference stations and $K_r$ satellites.

## 3.4 Estimation of Satellite Positions and Satellite Clock Offsets

Integer ambiguity resolution for absolute positioning requires not only the estimation of the phase biases $\tilde{\tilde{\beta}}_{m,r}$, $\tilde{\tilde{\beta}}_m^k$, but also of the combined code biases $b_{g_r}$ and $b_g^k$, since they are absorbed in the range term in (2.20) and (2.21). The range term $\tilde{g}_r^k(t_n)$, obtained from the estimate of the first Kalman filter, is rewritten as

$$\tilde{g}_r^k(t_n) = (\boldsymbol{e}_r^k(t_n))^{\mathrm{T}} \cdot (\boldsymbol{r}_r - \boldsymbol{r}^k(t_n)) + c \cdot (\delta\tilde{\tau}_r(t_n) - \delta\tilde{\tau}^k(t_n)) + m_{\mathrm{w}}(E_r^k(t_n)) \cdot T_{\mathrm{z},r}^k(t_n) + \tilde{\eta}_r^k(t_n),$$
(3.91)

where the code biases can not be separated from the clock offsets, i.e.

$$\begin{aligned} c\delta\tilde{\tau}_r(t_n) &= c\delta\tau_r(t_n) + b_{g_r} \\ c\delta\tilde{\tau}^k(t_n) &= c\delta\tau^k(t_n) - b_g^k. \end{aligned}$$
(3.92)

A second Kalman filter is used to estimate the satellite positions $\boldsymbol{r}^k$, the satellite velocities $\dot{\boldsymbol{r}}^k$, as well as the tropospheric zenith delays $T_{\mathrm{z},r}$ and the combined clock/bias terms $c\delta\tilde{\tau}_r$,
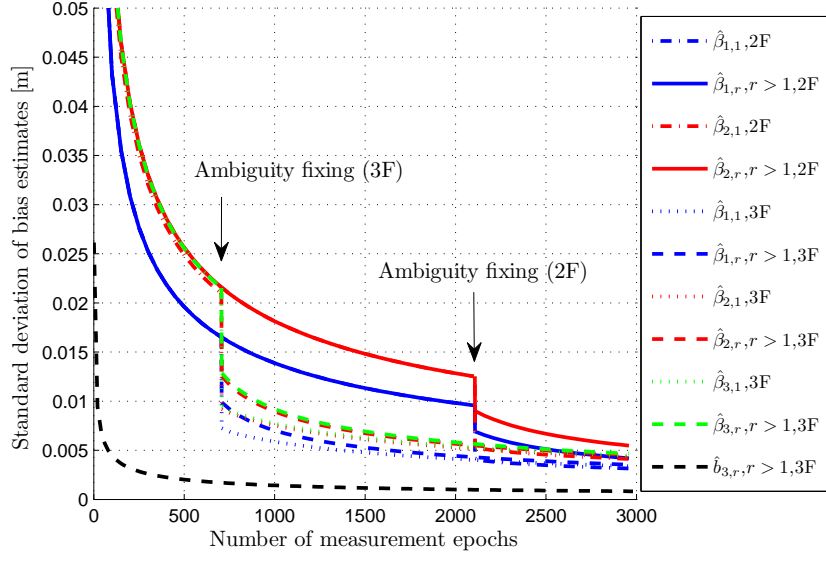
Fig. 3.7: Bias estimation with dual frequency E1-E5a and triple frequency E1-E5a-E5b measurements: The redundancy given by the third frequency enables an almost three times earlier ambiguity fixing, and thus, a higher accuracy of the receiver phase bias estimates. The achievable accuracies are also shown for the code biases on the third frequency which have to be estimated as the ranges and ionospheric delays can absorb the code biases on only two frequencies.

i.e. the state vector becomes

$$\boldsymbol{x}_n = \big[\boldsymbol{r}^{1,\mathrm{T}}(t_n),\ldots,\boldsymbol{r}^{K,\mathrm{T}}(t_n),\dot{\boldsymbol{r}}^{1,\mathrm{T}}(t_n),\ldots,\dot{\boldsymbol{r}}^{K,\mathrm{T}}(t_n),T_{\mathrm{Z}_1}(t_n),\ldots,T_{\mathrm{Z}_R}(t_n),c\delta\tilde{\tau}_1(t_n),\ldots,$$
$$c\delta\tilde{\tau}_R(t_n),c\delta\tilde{\tau}^1(t_n),\ldots,c\delta\tilde{\tau}^K(t_n)\big]^{\mathrm{T}}. \tag{3.93}$$

The model for the measurements is given by

$$\begin{bmatrix} \tilde{g}_1^1(t_n) - (\boldsymbol{e}_1^1)^{\mathrm{T}}(t_n)\cdot\boldsymbol{r}_1 \\ \vdots \\ \tilde{g}_1^{K_1}(t_n) - (\boldsymbol{e}_1^{K_1})^{\mathrm{T}}(t_n)\cdot\boldsymbol{r}_1 \\ \vdots \\ \tilde{g}_R^1(t_n) - (\boldsymbol{e}_R^1)^{\mathrm{T}}(t_n)\cdot\boldsymbol{r}_R \\ \vdots \\ \tilde{g}_R^{K_R}(t_n) - (\boldsymbol{e}_R^{K_R}(t_n))^{\mathrm{T}}\cdot\boldsymbol{r}_R \end{bmatrix} = - \begin{bmatrix} (\boldsymbol{e}_1^1(t_n))^{\mathrm{T}}\cdot\boldsymbol{r}^1(t_n) \\ \vdots \\ (\boldsymbol{e}_1^{K_1}(t_n))^{\mathrm{T}}\cdot\boldsymbol{r}^{K_1}(t_n) \\ \vdots \\ (\boldsymbol{e}_R^1(t_n))^{\mathrm{T}}\cdot\boldsymbol{r}^R(t_n) \\ \vdots \\ (\boldsymbol{e}_R^{K_R}(t_n))^{\mathrm{T}}\cdot\boldsymbol{r}^{K_R}(t_n) \end{bmatrix} +$$
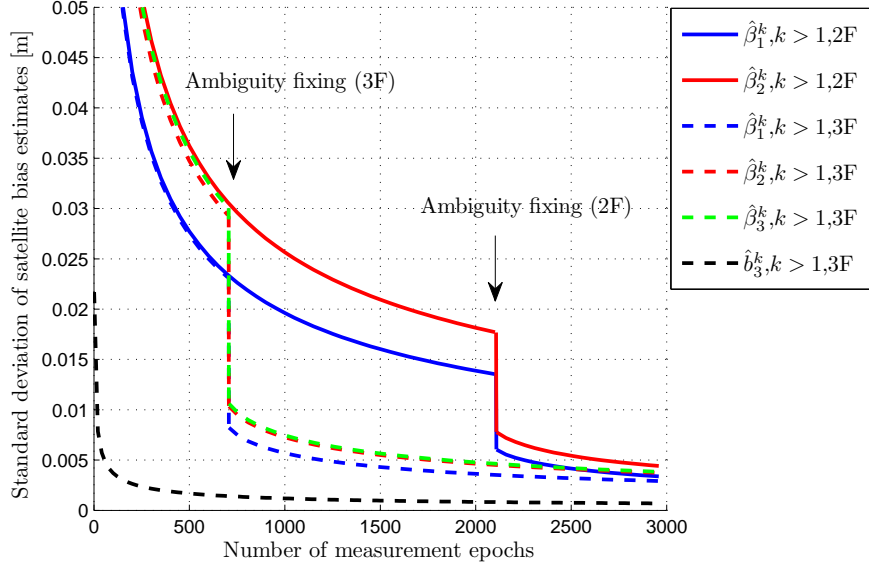
Fig. 3.8: Benefit of measurements on a third frequency for satellite bias estimation. The same scenario as in Fig. 3.7 has been assumed. The redundancy given by the third frequency results in an almost three times earlier ambiguity fixing with $P_\mathrm{w} = 10^{-9}$.

$$
+[\boldsymbol{H}_\mathrm{T} \quad \boldsymbol{H}_{b_r} \quad \boldsymbol{H}_{b^k}] \cdot
\begin{bmatrix}
T_{\mathrm{Z}_1}(t_n) \\
\vdots \\
T_{\mathrm{Z}_R}(t_n) \\
c\delta\tilde{\tau}_1(t_n) \\
\vdots \\
c\delta\tilde{\tau}_R(t_n) \\
c\delta\tilde{\tau}^1(t_n) \\
\vdots \\
c\delta\tilde{\tau}^K(t_n)
\end{bmatrix}
+
\begin{bmatrix}
\tilde{\eta}_1^1(t_n) \\
\vdots \\
\tilde{\eta}_1^{K_1}(t_n) \\
\vdots \\
\tilde{\eta}_R^1(t_n) \\
\vdots \\
\tilde{\eta}_R^{K_R}(t_n)
\end{bmatrix},
\qquad (3.94)
$$

with the unit vectors $\boldsymbol{e}_r^k$ pointing from the satellites to the reference stations, and the tropospheric mapping matrix $\boldsymbol{H}_\mathrm{T}$ for transforming the tropospheric zenith delays into slant delays, i.e.

$$
\boldsymbol{H}_\mathrm{T} =
\begin{bmatrix}
\boldsymbol{m}_{\mathrm{T},1} & & & \\
& \boldsymbol{m}_{\mathrm{T},2} & & \\
& & \ddots & \\
& & & \boldsymbol{m}_{\mathrm{T},R}
\end{bmatrix}, \text{ with } \quad
\boldsymbol{m}_{\mathrm{T},r} =
\begin{bmatrix}
m_\mathrm{T}(E_r^1(t_n)) \\
m_\mathrm{T}(E_r^2(t_n)) \\
\vdots \\
m_\mathrm{T}(E_r^{K_r}(t_n))
\end{bmatrix},
\qquad (3.95)
$$

where the tropospheric mapping function $m_T(E_r^k(t_n))$ was introduced by Niell [22] in Eq. (3.96) and only depends on the latitude, height and day of the year. His functions are accurate to 1 mm for elevations larger than 3° (Niell [22]).

$$m_T(E_r^k(t_n)) = \frac{1 + \dfrac{a}{1 + \dfrac{b}{1 + c}}}{\sin E_r^k(t_n) + \dfrac{a}{\sin E_r^k(t_n) + \dfrac{b}{\sin E_r^k(t_n) + c}}}, \tag{3.96}$$

with the parameters $a$, $b$, and $c$ being determined differently for dry and wet components. The receiver clock/bias generation matrix is given by

$$\boldsymbol{H}_{b_r} = \begin{bmatrix} \mathbf{1}^{K_1 \times 1} & & \\ & \ddots & \\ & & \mathbf{1}^{K_R \times 1} \end{bmatrix}. \tag{3.97}$$

Assume that the set $\mathcal{S}_r$, for $r = \{1, \ldots, R\}$, contains all satellites that are visible from at least one reference station, i.e.

$$\begin{aligned} S_1 &\triangleq \{k_{S_1}^1, \ldots, k_{S_1}^{K_1}\}, \\ &\vdots \\ S_R &\triangleq \{k_{S_R}^1, \ldots, k_{S_R}^{K_R}\}, \end{aligned} \tag{3.98}$$

and the union set $\mathcal{S}$ is given by

$$\mathcal{S} = \{\mathcal{S}_1 \cup \mathcal{S}_2 \cup \ldots \cup \mathcal{S}_R\}, \tag{3.99}$$

Let $\mu(k, \mathcal{S}_r)$ describe the position of the $k$-th satellite of subset $\mathcal{S}_r$, the coefficient matrix for satellite clock/bias is obtained as

$$\boldsymbol{H}_{b_I^k}\left[\sum_{r'=1}^{r-1} K_{r'} + k, j\right] = \begin{cases} 1, & \text{if } j = \mu(k, \mathcal{S}_r). \\ 0, & \text{elsewhere.} \end{cases}, \tag{3.100}$$

The iterative Newton algorithm is integrated into the Kalman filter initialization, to estimate the unknown satellite positions, so as to determine the $\boldsymbol{e}_r^k$ vector. The obtained satellite position estimates $\hat{\boldsymbol{r}}^k$ can be used to verify the satellite ephemeris data from the navigation message.

It is recommended that the estimated biases $\hat{\bar{\bar{\beta}}}_m^k$, $\hat{b}_3^k$ and $\hat{b}_{g^k}$ for all $m$ and $k$ are transmitted by a satellite based augmentation system to enable integer ambiguity resolution for absolute positioning of a multi-frequency user.

# 4 Estimation of Code Biases and Ionospheric Grid

The Wide Area Augmentation System (WAAS) Minimum Operation Performance Standard (MOPS) defines a grid on the ionosphere layer for modeling the vertical ionospheric delay (Chao et al. [23]). WAAS provides the vertical ionospheric delays at the grid points as corrections to the users. Once the users receive the corrections for the ionospheric delays, they will apply the correction values to determine their slant delays, by interpolating the corrections from the four nearest surrounding grid points to the pierce points, as shown in Fig. 4.1.
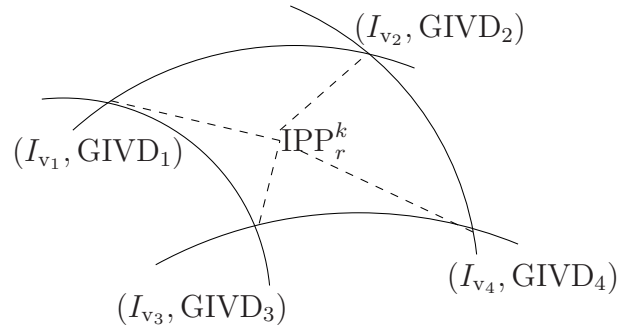


Fig. 4.1: WAAS ionosphere grid model correction for the single-frequency users (Chao et al. [23]).

The code biases and grid ionospheric vertical delays (GIVD) can be estimated also without integer ambiguity resolution. Eq. (2.20) and (2.21) are reconstructed here:

$$
\begin{aligned}
\rho_{1,r}^k(t_n) &= \tilde{g}_r^k(t_n) + \tilde{I}_{1,r}^k(t_n) + \eta_{1,r}^k(t_n) \\
\rho_{2,r}^k(t_n) &= \tilde{g}_r^k(t_n) + q_{12}^2 \tilde{I}_{1,r}^k(t_n) + \eta_{2,r}^k(t_n),
\end{aligned}
\tag{4.1}
$$

where the ionospheric slant delays can be further modeled as

$$
\tilde{I}_{1,r}^k(t_n) = m_I(E_r^k(t_n)) \cdot \tilde{I}_{1,v,r}^k(t_n) + b_{I_r} + b_{I^k} + \tilde{\eta}_{I,r}^k(t_n),
\tag{4.2}
$$

with the mapping function for the vertical ionospheric delays, i.e.

$$m_{\mathrm{I}}(E_r^k(t_n)) = \frac{1}{\sqrt{1 - \frac{\cos^2(E_r^k(t_n))}{(1+h/R_e)^2}}}, \tag{4.3}$$

and $E_r^k$ denoting the elevation angle as seen from the $r$-th receiver to the $k$-th satellite.

By forming a geometry-free, ionosphere-preserving combination of code measurements, the ionospheric slant delays $\tilde{I}_r^k(t_n)$ including the receiver and satellite biases are then given by

$$\tilde{I}_r^k(t_n) = \alpha_1 \rho_{1,r}^k(t_n) + \alpha_2 \rho_{2,r}^k(t_n), \tag{4.4}$$

with

$$\alpha_1 = \frac{-f_2^2}{f_1^2 - f_2^2}, \quad \text{and} \quad \alpha_2 = \frac{f_2^2}{f_1^2 - f_2^2}. \tag{4.5}$$

Moreover, a geometry-free ionosphere-preserving time-differenced combination of carrier phase measurements is introduced to make the ionospheric rates observable, i.e.

$$\dot{\tilde{I}}_r^k(t_n) = \sum_{m=1}^{M} \gamma_m \lambda_m(\phi_m(t_{n+1}) - \phi_m(t_n)), \tag{4.6}$$

where $\gamma_m$ denotes the weighting coefficients of the geometry-free, ionosphere-preserving combination.

In the next few sections, two models for estimating code biases and GIVDs will be presented: The first one is based on the use of a background model. The second model performs a least-squares fitting of a plane through the measurements of the pierce points in a surrounding region. Some simulation results are shown under the estimation of a grid over Europe with the EGNOS network.

## 4.1   Interpolation of Grid Points Delays

The vertical ionospheric delays $I_{\mathrm{v},r}^k$ at the pierce points can be calculated by interpolation of the vertical delays at the surrounding grid points which are weighted differently based on some distance law, i.e.

$$\tilde{I}_r^k(t_n) = m_{\mathrm{I}}(E_r^k(t_n)) \cdot \left( \sum_{l=1}^{L} \Lambda_r^{k,(l)} i_l(t_n) + \tau_r^k + \eta_{I,r}^k(t_n) \right) + b_{I_r} + b_{I^k} + \tilde{\eta}_{I,r}^k(t_n), \tag{4.7}$$

where $L$ denotes the number of grid points, $\tau_r^k$ has the values either 0 or $\mathcal{E}[I_{\mathrm{v},r}^k]$ depending on the background model, and the coefficients $\Lambda_r^{k,(l)}$ is a function of the distance between

pierce points and grid points, i.e.

$$\Lambda_r^{k,(l)} = \frac{\left(\frac{1}{\epsilon_r^{k,(l)}}\right)^2}{\sum_{l=1}^{L}\left(\frac{1}{\epsilon_r^{k,(l)}}\right)^2}. \tag{4.8}$$

The weights $\epsilon_r^{k,(l)}$ are typically assumed to be in the form

$$\epsilon_r^{k,(l)} = \sigma_r^k f(\|\boldsymbol{x}_{\mathrm{IPP}_r^k} - \boldsymbol{x}_{\mathrm{IGP}^{(l)}}\|), \tag{4.9}$$

where $f$ denotes the ionospheric delay distance correlation functions. One model is described in Chao et al. [23], with the experimentally-determined function $f_1$ derived from the National Satellite Test Bed (NSTB) data, and $f_2$ being an empirical function used for the weighted least-squares estimator, i.e.

$$\begin{aligned}
f_1(\|\boldsymbol{x}_{\mathrm{IPP}_r^k} - \boldsymbol{x}_{\mathrm{IGP}^{(l)}}\|) &= 0.2 + 0.6 \cdot e^{-0.4\|\boldsymbol{x}_{\mathrm{IPP}_r^k}-\boldsymbol{x}_{\mathrm{IGP}^{(l)}}\|/D} \\
f_2(\|\boldsymbol{x}_{\mathrm{IPP}_r^k} - \boldsymbol{x}_{\mathrm{IGP}^{(l)}}\|) &= 0.8 \cdot e^{\left(\frac{\|\boldsymbol{x}_{\mathrm{IPP}_r^k}-\boldsymbol{x}_{\mathrm{IGP}^{(l)}}\|}{2D}\right)^2},
\end{aligned} \tag{4.10}$$

where $D$ equals to 556 km for a 5-degree grid spacing.

Another model for weights $\epsilon_r^{k,(l)}$ is described in Conker et al. [24], i.e.

$$\frac{1}{(\epsilon_r^{k,(l)})^2} = \frac{\sin E_r^k}{\|\boldsymbol{x}_{\mathrm{IPP}_r^k} - \boldsymbol{x}_{\mathrm{IGP}^{(l)}}\|}, \tag{4.11}$$

which indicates that a high elevation and a small distance lead to large weights.

Fig. 4.2 shows the geometry for computing the positions of ionosphere pierce points. Applying the cosine law in the triangle (C,$r$,IPP) yields

$$\cos\left(\frac{\pi}{2} + E_r^k\right) = \frac{R_{\mathrm{e}}^2 + (d_r^k)^2 - (R_{\mathrm{e}} + h)^2}{2R_{\mathrm{e}}d_r^k}, \tag{4.12}$$

where $d_r^k$ denotes the distance between the receiver and the pierce point, i.e.

$$d_r^k = -R_{\mathrm{e}}\sin E_r^k + \sqrt{R_{\mathrm{e}}^2\sin^2 E_r^k - (R_{\mathrm{e}}^2 - (R_{\mathrm{e}}+h)^2)}. \tag{4.13}$$

Thus, based on the knowledge of the e-vector from the satellite, the position of the pierce points is obtained by

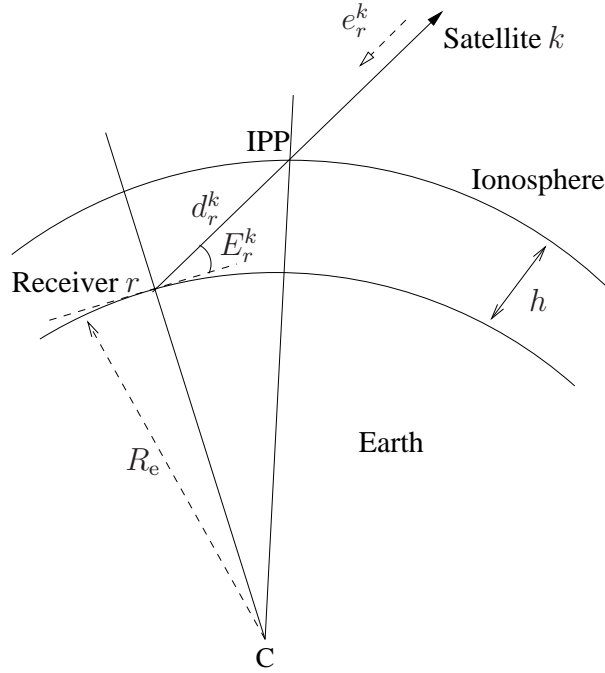$$\vec{x}_{\mathrm{IPP}} = \vec{x}_r - d_r^k \cdot \vec{e}_r^k. \tag{4.14}$$

Fig. 4.2: Geometry for ionosphere pierce point.

## 4.2 Least-squares Fitting

Another method for determining the vertical delays at the grid points is to perform a weighted least-squares fitting of the vertical delays from a set of nearby pierce points, i.e.

$$\min_{\boldsymbol{i}_n^{(l)}, \boldsymbol{b}} \left\| \tilde{\boldsymbol{I}}_n - \boldsymbol{M} \cdot \boldsymbol{H}_{II} \boldsymbol{i}_n^{(l)} - \boldsymbol{H}_b \boldsymbol{b} \right\|_{\boldsymbol{\Sigma}^{-1}}^2 , \tag{4.15}$$

where

$$\begin{aligned}
\tilde{\boldsymbol{I}}_n &= \left[ \tilde{I}_1^1(t_n), \tilde{I}_1^2(t_n), \ldots, \tilde{I}_1^{K_1}(t_n), \ldots, \tilde{I}_R^{K_R}(t_n), \dot{\tilde{I}}_1^1(t_n), \ldots, \dot{\tilde{I}}_R^{K_R}(t_n) \right]^{\mathrm{T}}, \\
\boldsymbol{i}_n^{(l)} &= \left[ i_0^{(l)}(t_n), i_\phi^{(l)}(t_n), i_\lambda^{(l)}(t_n), \dot{i}_0^{(l)}(t_n), \dot{i}_\phi^{(l)}(t_n), \dot{i}_\lambda^{(l)}(t_n) \right]^{\mathrm{T}}, \\
\boldsymbol{b} &= \left[ b_{\mathrm{I}_1}, \ldots, b_{\mathrm{I}_R}, b_{\mathrm{I}^2}, \ldots, b_{\mathrm{I}^K} \right]^{\mathrm{T}},
\end{aligned} \tag{4.16}$$

with $i_0^{(l)}, i_\phi^{(l)}, i_\lambda^{(l)}$ denoting correspondingly the vertical ionospheric delay, the latitudinal gradient and the longitudinal gradient at the ionospheric grid point (IGP) $(\phi^{(l)}, \lambda^{(l)})$, and $\dot{i}_0^{(l)}, \dot{i}_\phi^{(l)}, \dot{i}_\lambda^{(l)}$ denoting the first order derivative over time. The $\tilde{I}_r^k$ represents the slant ionospheric delays at the ionospheric pierce point (IPP) $(\phi_r^k, \lambda_r^k)$.

The mapping function of the vertical delays is given by

$$\boldsymbol{M} = \begin{bmatrix} m_{\mathrm{I}}(E_1^1) & & \\ & \ddots & \\ & & m_{\mathrm{I}}(E_R^{K_R}) \end{bmatrix}. \tag{4.17}$$

The coefficient matrix of the least-squares fitting is given by

$$\boldsymbol{H}_{I\dot{I}} = \boldsymbol{1}^{2\times 2} \otimes \begin{bmatrix} 1 & \phi_1^1 - \phi^{(l)} & \lambda_1^1 - \lambda^{(l)} \\ \vdots & \vdots & \vdots \\ 1 & \phi_R^{K_R} - \phi^{(l)} & \lambda_R^{K_R} - \lambda^{(l)} \end{bmatrix}. \tag{4.18}$$

The bias coefficient matrix $\boldsymbol{H}_b$ is constructed as

$$\boldsymbol{H}_b = [\boldsymbol{H}_{b_{I_r}} \quad \boldsymbol{H}_{b_{I^k}}], \tag{4.19}$$

with the receiver code bias coefficient matrix

$$\boldsymbol{H}_{b_{I_r}} = \begin{bmatrix} \boldsymbol{1}^{K_1 \times 1} & & & \\ & \boldsymbol{1}^{K_2 \times 1} & & \\ & & \ddots & \\ & & & \boldsymbol{1}^{K_R \times 1} \end{bmatrix}, \tag{4.20}$$

and the satellite code bias coefficient matrix

$$\boldsymbol{H}_{b_I^k}\left[\sum_{r'=1}^{r-1} K_{r'} + k, j\right] = \begin{cases} 1, & \text{if} \quad j = \mu(k, \mathcal{S}_r). \\ 0, & \text{elsewhere.} \end{cases}, \tag{4.21}$$

where $\mu(k, \mathcal{S}_r)$ describes the position of the $k$-th satellite of subset

$$\mathcal{S}_r \triangleq \{k_{\mathcal{S}_r}^1, \ldots, k_{\mathcal{S}_r}^{K_r}\} \tag{4.22}$$

within the union set

$$\mathcal{S} = \{\mathcal{S}_1 \cup \mathcal{S}_2 \cup \ldots \cup \mathcal{S}_R\}, \tag{4.23}$$

which contains all satellites that are visible from at least one reference station.

A weighting matrix is introduced into the system to take the elevation angles and distances between the IPPs and the IGP into account, i.e.large contribution is given to the slant delays observed at high elevations and close to the IGP (see Henkel [1]), i.e.

$$\boldsymbol{\Sigma} = \begin{bmatrix} \frac{\sin(E_1^1)}{\|\boldsymbol{x}_{\mathrm{IPP}_1^1} - \boldsymbol{x}_{\mathrm{IGP}(l)}\|} & & \\ & \ddots & \\ & & \frac{\sin(E_R^{K_R})}{\|\boldsymbol{x}_{\mathrm{IPP}_R^{K_R}} - \boldsymbol{x}_{\mathrm{IGP}(l)}\|} \end{bmatrix}, \tag{4.24}$$

where $\boldsymbol{x}_{\mathrm{IPP}_r^k}$ is the position of ionospheric pierce point $\mathrm{IPP}_r^k$ and $\boldsymbol{x}_{\mathrm{IGP}^{(l)}}$ is the position of ionospheric grid point $\mathrm{IGP}^{(l)}$.

It is noted that not all of the measurements from the pierce points should be included into the fitting plane due to the irregularity of the ionosphere. Therefore, a boundary circle around each grid point to include only nearby pierce points for the least-squares fitting. In this section, the radius of the boundary circle is set to a typical value of 2000 km (see e.g. Chao et al. [23]).

Now, simulated measurements from a network of EGNOS RIMS stations in Europe, as shown in Tab. 4.1, shall be considered.

Table 4.1: Approximate locations of the EGNOS RIMS stations in Europe (Arbesser-Rastburg [25]).

| Station | Latitude | Longitude | Station | Latitude | Longitude |
|---|---|---|---|---|---|
| Alberg | 56.8° N | 10.0° E | Mersa Matrouh | 33.1° N | 27.1° E |
| Azores Islands | 38.3° N | 28.0° W | Mourmansk | 68.5° N | 33.0° E |
| Berlin | 52.3° N | 13.2° E | Palma de Mallorca | 40.0° N | 4.0° E |
| Canary Islands | 28.3° N | 14.1° W | Paris | 48.5° N | 2.2° E |
| Catania | 37.0° N | 15.0° E | Reykjavik | 64.1° N | 21.6° W |
| Cork | 52.0° N | 8.0° W | Roma - Fucino | 42.0° N | 14.0° E |
| Cracovie | 50.0° N | 20.0° E | Saint Petersburg | 60.0° N | 30.0° E |
| Djerba | 34.0° N | 11.0° E | Santiago de Compostella | 42.9° N | 8.3° W |
| Feroe Islands | 62.0° N | 6.7° W | Sofia | 43.0° N | 23.0° E |
| Glasgow | 55.7° N | 4.1° W | Stockholm | 59.0° N | 18.0° E |
| Konya | 37.6° N | 32.6° E | Tel Aviv | 31.8° N | 34.8° E |
| Lisboa | 38.5° N | 9.0° W | Toulouse | 43.4° N | 1.3° E |
| London | 52.0° N | 0.0° | Trondheim | 63.3° N | 10.4° E |
| Madere | 32.4° N | 17.1° W | Tromsö | 69.5° N | 19.0° E |
| Melilla | 35.4° N | 3.0° W | Zürich | 47.2° N | 8.3° E |

The vertical ionospheric delays in a 5° × 5° grid over Europe are estimated using a least-squares fitting. Fig. 4.3 shows the map of Europe with EGNOS RIMS stations (red circles), ionospheric pierce points (green circles) and ionospheric grid points (blue squares) for a 5° × 5° grid.

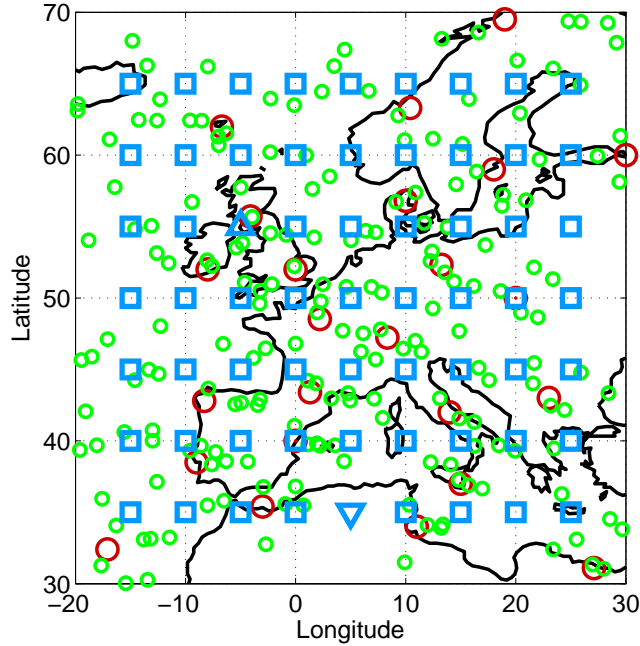Fig. 4.4 shows the achievable accuracies for GIVD estimates, which depend on the

Fig. 4.3: Ionospheric grid: Map of Europe with EGNOS RIMS stations (red circles), ionospheric pierce points (green circles) and ionospheric grid points (blue squares) of a $5° \times 5°$ grid. The grid points for which the ionospheric delay can be estimated most and least accurately are also indicated (blue triangles).

geometry of the pierce points around the grid points. The geometry-free ionosphere-preserving combination of code measurements on E1 and E5, along with the geometry-free ionosphere-preserving time-differenced combination of carrier phase measurements are used in a Kalman filter to estimate the code biases and the GIVD. The most and least accurately computable vertical grid ionospheric delays are also indicated in Fig. 4.3 as blue triangles.

Fig. 4.5 shows the error in receiver bias estimates using a least-squares fitting with simulated E1 and E5 Galileo measurements from a network of 30 EGNOS reference stations. The boundary circle for each grid point has been set to 2000 km. Fig. 4.6 shows the errors in satellite bias estimates for the same scenario. The simulation results show that the code biases and vertical ionospheric delays can be estimated with a 1-cm accuracy.

After the estimation of the code biases and grid ionospheric vertical delays, the GIVDs can then be applied to a single-frequency user to determine its ionospheric slant delay. It has been recommended in Henkel et al. [6] and [7] that the satellite code bias estimates $\hat{b}_{I^k}$ are transmitted by a satellite based augmentation system.
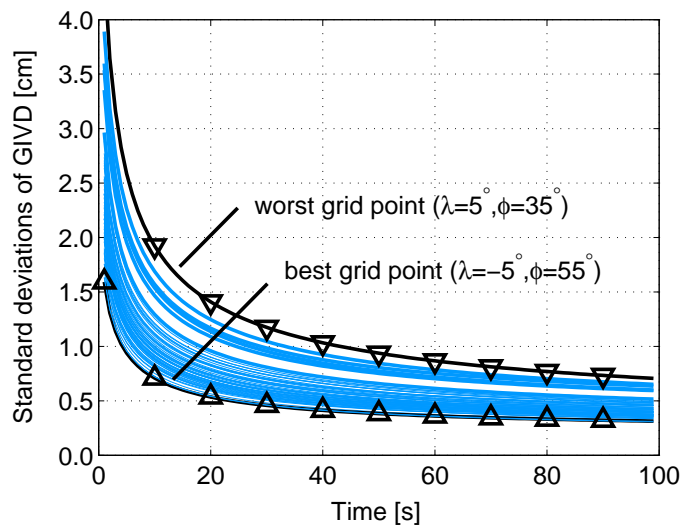
Fig. 4.4: Achievable accuracies for GIVD: A least-squares fitting has been used to estimate the states for each grid point, and the figure shows the accuracy of the estimates, in which the worst and best grid points depended on the geometry of the pierce points around them, as shown in Fig. 4.3.
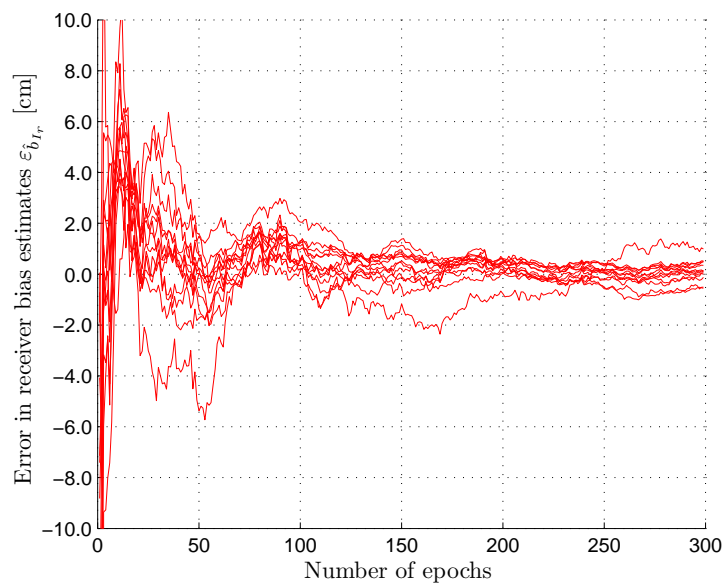


Fig. 4.5: Error in receiver biases with simulated E1 and E5 Galileo measurements from a network of 30 EGNOS stations. After 300 epochs the errors in receiver biases are converged to 1 cm.
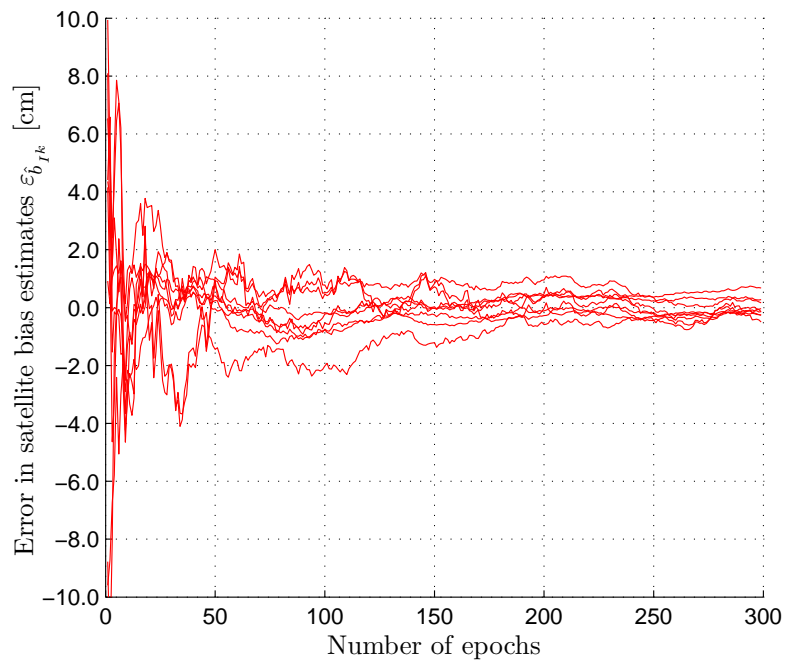
Fig. 4.6: Error in satellite biases estimates using same scenario as in Fig. 4.5. The errors are bounded by 1 cm after 300 epochs.

# 5 Real Data Analysis

## 5.1 Estimation of Receiver and Satellite Phase Biases

Chapter 3 has presented a method to estimate the receiver and satellite phase biases using measurements from a network of reference stations. The proposed method is validated here with real GPS measurements from the SAPOS network. A 1 mm accuracy and a stability between 10 cm/hour and 20 cm/hour are observed in the bias estimates.

The GPS code and carrier phase measurements on frequencies L1 and L2 are taken from the SAPOS stations in Bavaria (Fig. 5.1) on March 1, 2010, 8:00-10:00 UTC. The state vector of the Kalman filter includes the ranges, range rates, second derivatives of ranges (range accelerations), ionospheric slant delays, phase biases and integer ambiguities, i.e.

$$\boldsymbol{x}_n = \left[\tilde{\boldsymbol{g}}^{\mathrm{T}}(t_n),\, \dot{\tilde{\boldsymbol{g}}}^{\mathrm{T}}(t_n),\, \ddot{\tilde{\boldsymbol{g}}}^{\mathrm{T}}(t_n),\, \tilde{\boldsymbol{I}}^{\mathrm{T}}(t_n),\, \tilde{\tilde{\boldsymbol{\beta}}}_{\mathrm{R}}^{\mathrm{T}},\, \tilde{\tilde{\boldsymbol{\beta}}}_{\mathrm{S}}^{\mathrm{T}}, \tilde{\boldsymbol{N}}\right]^{\mathrm{T}}, \tag{5.1}$$

with the range accelerations being

$$\ddot{\tilde{\boldsymbol{g}}}(t_n) = \left[\ddot{\tilde{g}}_1^1(t_n),\ldots,\ddot{\tilde{g}}_1^{K_1}(t_n),\ldots,\ddot{\tilde{g}}_R^{K_R}(t_n)\right]^{\mathrm{T}} \tag{5.2}$$

and other component vectors described in (3.14).

The state transition matrix for predicting the next state for the current one is given by

$$\boldsymbol{\Phi} = \begin{bmatrix} \mathbf{1}^{s\times s} & \Delta t \cdot \mathbf{1}^{s\times s} & \frac{1}{2}\Delta t^2 \cdot \mathbf{1}^{s\times s} & \mathbf{0} \\ \mathbf{0} & \mathbf{1}^{s\times s} & \Delta t \cdot \mathbf{1}^{s\times s} & \mathbf{0} \\ \mathbf{0} & \mathbf{0} & \mathbf{1}^{s\times s} & \mathbf{0} \\ \mathbf{0} & \mathbf{0} & \mathbf{0} & \mathbf{1}^{3s\times 3s} \end{bmatrix}, \tag{5.3}$$

with $s$ defined in Eq. (3.19).

The process noise of the state vector follows a zero mean Gaussian distribution with the noise covariance matrix defined by Eq. (3.28). The parameter $S_p$ has been set to 1
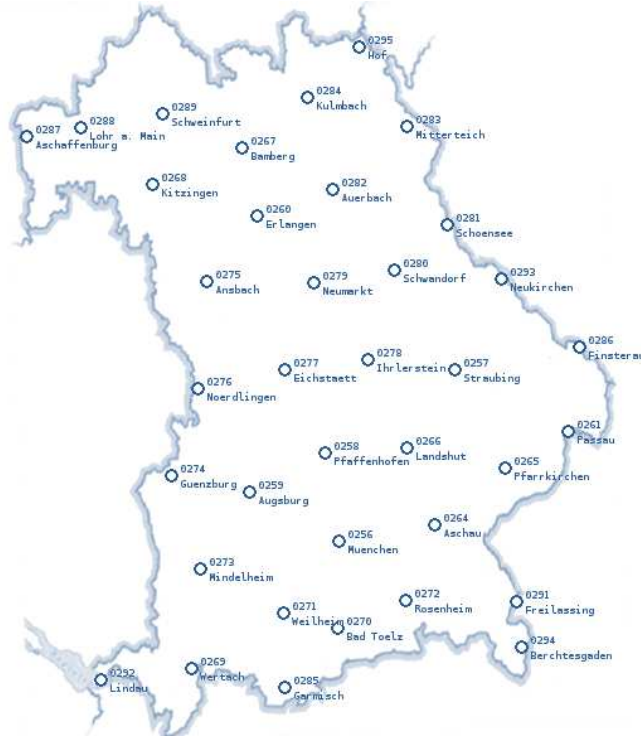
Fig. 5.1: Reference stations of SAPOS network in Bavaria [26].

$(\text{mm/s}^2)^2/s$, thus, the variances of the process noise follow

$$
\begin{aligned}
\sigma_{\tilde{g}}^2 &= \frac{1}{20} S_{\text{p}} \cdot \Delta t^5 = 0.05 \text{mm}^2 \\
\sigma_{\dot{\tilde{g}}}^2 &= \frac{1}{3} S_{\text{p}} \cdot \Delta t^3 = 0.33 \text{ mm}^2/\text{s}^2 \\
\sigma_{\ddot{\tilde{g}}}^2 &= S_{\text{p}} \cdot \Delta t = 1 \text{ mm}^2/\text{s}^4,
\end{aligned} \tag{5.4}
$$

and the standard deviation of the ionospheric process noise has been set to 1 cm.

The code and carrier phase measurement noise is also assumed to be zero mean Gaussian distributed, but with an elevation-dependent standard deviation $\sigma_\rho(E_r^k)$ and $\sigma_\phi(E_r^k)$, which are assumed to be described by an exponential profile, i.e.

$$
\begin{aligned}
\sigma_\rho(E_r^k) &= \sigma_\rho(0°) \cdot e^{-E_r^k/\zeta_\rho} \\
\sigma_\phi(E_r^k) &= \sigma_\phi(0°) \cdot e^{-E_r^k/\zeta_\phi},
\end{aligned} \tag{5.5}
$$

where $E_r^k$ denotes the elevation angle of the $r$-th receiver and $k$-th satellite, and $\zeta_\rho$ and $\zeta_\phi$ are the decay factors of the noise bound. The following parameters are chosen for the exponential profiles:

$$
\begin{aligned}
\sigma_\rho(0°) &= 100.0 \text{cm}, \quad \sigma_\rho(90°) = 25.0 \text{cm} \\
\sigma_\phi(0°) &= 10.0 \text{mm}, \quad \sigma_\phi(90°) = 2.5 \text{mm}.
\end{aligned} \tag{5.6}
$$

Fig. 5.2 shows the elevation-dependent standard deviation of both code and carrier phase measurement noise, with an elevation-mask of 5°.
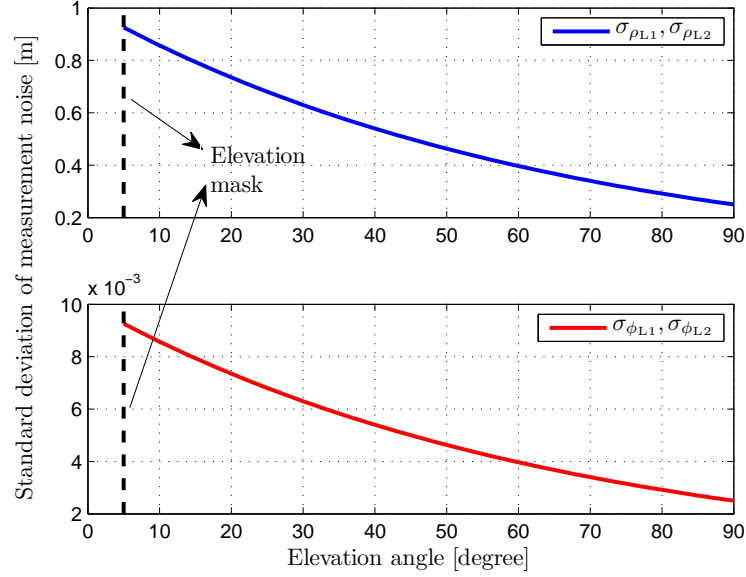


Fig. 5.2: Elevation-dependent standard deviations of code and carrier phase measurement noise.

The least-squares initialization requires at least three measurement epochs to get initial estimates of ranges, range rates and range accelerations, etc:

$$\begin{bmatrix} \hat{\boldsymbol{x}}(t_{n-1}) \\ \hat{\boldsymbol{x}}(t_n) \\ \hat{\boldsymbol{x}}(t_{n+1}) \end{bmatrix} = (\boldsymbol{H}_{\text{comb}}^{\text{T}} \boldsymbol{\Sigma}_{\text{comb}}^{-1} \boldsymbol{H}_{\text{comb}})^{-1} \boldsymbol{H}_{\text{comb}}^{\text{T}} \boldsymbol{\Sigma}_{\text{comb}}^{-1} \cdot \begin{bmatrix} \boldsymbol{z}(t_{n-1}) \\ \boldsymbol{z}(t_n) \\ \boldsymbol{z}(t_{n+1}) \end{bmatrix}, \qquad (5.7)$$

with

$$\boldsymbol{H}_{\text{comb}} = \begin{bmatrix} \boldsymbol{1}^{3\times 3} \otimes \boldsymbol{H}_{\tilde{g}} & \boldsymbol{1}^{3\times 3} \otimes \boldsymbol{H}_{\tilde{I}} & \boldsymbol{1}^{3\times 1} \otimes \begin{bmatrix} \boldsymbol{H}_{\tilde{\tilde{\beta}}_R} & \boldsymbol{H}_{\tilde{\tilde{\beta}}S} & \boldsymbol{H}_{\tilde{N}} \end{bmatrix} \end{bmatrix}, \qquad (5.8)$$

and the combined measurement noise covariance matrix

$$\boldsymbol{\Sigma}_{\text{comb}} = \boldsymbol{1}^{3\times 3} \otimes \boldsymbol{\Sigma}_{\text{R}}. \qquad (5.9)$$

The covariance matrix of the least-squares estimates follows Eq. (5.7) as

$$\boldsymbol{\Sigma}_{\text{ls}} = \boldsymbol{W}_{\text{ls}}^{-1} = (\boldsymbol{H}_{\text{comb}}^{\text{T}} \boldsymbol{\Sigma}_{\text{comb}}^{-1} \boldsymbol{H}_{\text{comb}})^{-1} \qquad (5.10)$$

The high dimensionality of the covariance matrix and its ill-conditioning result in non-negligible errors with matrix inversion. However, the matrix $\boldsymbol{W}_{\text{ls}}$ has a blockwise structure

since the measurements are uncorrelated, i.e. $\boldsymbol{\Sigma}_{\text{comb}}$ consists of blocks of diagonal matrices. Therefore, $\boldsymbol{W}_{\text{ls}}$ can be subdivided into

$$
\begin{bmatrix} \boldsymbol{A} & \boldsymbol{B} \\ \boldsymbol{C} & \boldsymbol{D} \end{bmatrix} \triangleq \begin{bmatrix} \boldsymbol{W}_{\text{ls}}^{2sT_1 \times 2sT_1} & \boldsymbol{W}_{\text{ls}}^{2sT_1 \times 2s} \\ \boldsymbol{W}_{\text{ls}}^{2s \times 2sT_1} & \boldsymbol{W}_{\text{ls}}^{2s \times 2s} \end{bmatrix}, \tag{5.11}
$$

where $T_1$ denotes the number of epochs for least-squares initialization, and $\boldsymbol{A}$ and $\boldsymbol{D}$ are square matrices, which can be inverted. Furthermore, based on the special structure of $\boldsymbol{H}_{\text{comb}}$ and $\boldsymbol{\Sigma}_{\text{comb}}^{-1}$, $\boldsymbol{A}$ contains four diagonal matrices with equal dimensions. If $\boldsymbol{A}$ and $\boldsymbol{D} - \boldsymbol{C}\boldsymbol{A}^{-1}\boldsymbol{B}$ are non-singular, there holds

$$
\begin{aligned}
\boldsymbol{\Sigma}_{\text{ls}} &= \begin{bmatrix} \boldsymbol{A} & \boldsymbol{B} \\ \boldsymbol{C} & \boldsymbol{D} \end{bmatrix}^{-1} \\
&= \begin{bmatrix} \boldsymbol{A}^{-1} + \boldsymbol{A}^{-1}\boldsymbol{B}(\boldsymbol{D} - \boldsymbol{C}\boldsymbol{A}^{-1}\boldsymbol{B})^{-1}\boldsymbol{C}\boldsymbol{A}^{-1} & -\boldsymbol{A}^{-1}\boldsymbol{B}(\boldsymbol{D} - \boldsymbol{C}\boldsymbol{A}^{-1}\boldsymbol{B})^{-1} \\ -(\boldsymbol{D} - \boldsymbol{C}\boldsymbol{A}^{-1}\boldsymbol{B})^{-1}\boldsymbol{C}\boldsymbol{A}^{-1} & (\boldsymbol{D} - \boldsymbol{C}\boldsymbol{A}^{-1}\boldsymbol{B})^{-1} \end{bmatrix}. \tag{5.12}
\end{aligned}
$$

Thus, the inversion of the high dimensional matrix turns into matrix multiplications and the inversion of two matrices $\boldsymbol{A}$ and $\boldsymbol{D} - \boldsymbol{C}\boldsymbol{A}^{-1}\boldsymbol{B}$ with special structure and much smaller dimension, which makes the inversion more accurate and stable.

An example in Fig. 5.3 uses simulated Galileo measurements on E1 and E5 and estimates the ranges, range rates, range accelerations, ionospheric delays, biases and ambiguities. It shows the maximum relative differences between least-squares estimated biases and ambiguities, and their counterparts, i.e.

$$
\begin{aligned}
\Delta\hat{\beta}_{\text{rec}} &\triangleq \max_{m,r}\left(\left|\frac{\hat{\tilde{\tilde{\boldsymbol{\beta}}}}_{m,r} - \tilde{\tilde{\boldsymbol{\beta}}}_{m,r}}{\tilde{\tilde{\boldsymbol{\beta}}}_{m,r}}\right|\right) \\
\Delta\hat{\beta}^{\text{sat}} &\triangleq \max_{m,k}\left(\left|\frac{\hat{\tilde{\tilde{\boldsymbol{\beta}}}}_m^k - \tilde{\tilde{\boldsymbol{\beta}}}_m^k}{\tilde{\tilde{\boldsymbol{\beta}}}_m^k}\right|\right) \\
\lambda_{\tilde{m}}\Delta\hat{N}_{\tilde{m},\tilde{r}}^{\tilde{k}} &\triangleq \max_{m,r,k}\left(\lambda_m \cdot \left|\frac{\hat{\tilde{\boldsymbol{N}}}_{m,r}^k - \tilde{\boldsymbol{N}}_{m,r}^k}{\tilde{\boldsymbol{N}}_{m,r}^k}\right|\right). \tag{5.13}
\end{aligned}
$$

The least-squares initialization in the estimation process is computed based on the two distinctive methods of matrix inversion, i.e. direct inversion and blockwise inversion, which are denoted as "dl" and "bl" in Fig. 5.3 . As the dimension of the covariance matrix is getting higher, the errors in blockwise inversion stay at low values, while the direct inversion introduces significantly higher errors.
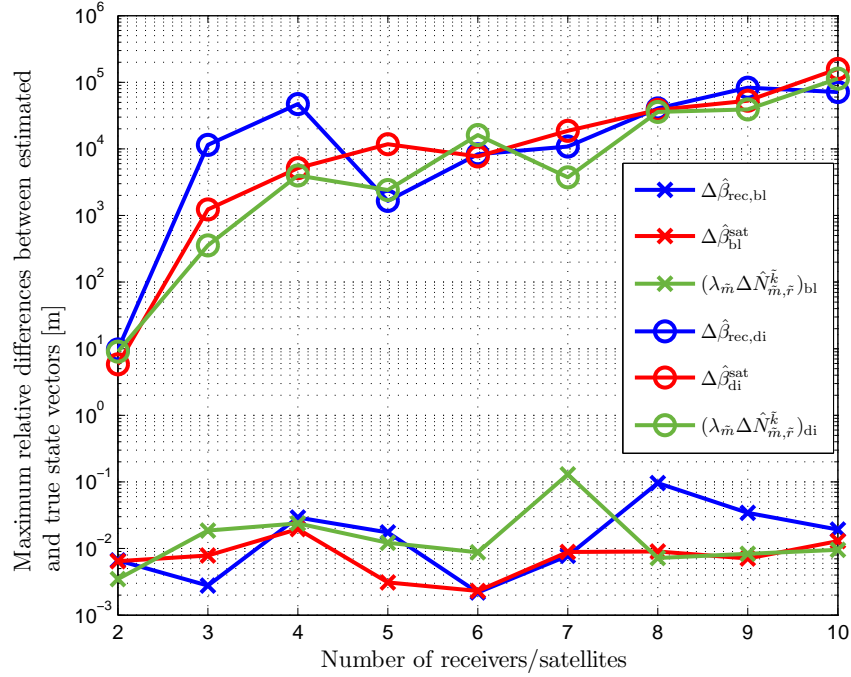
Fig. 5.3: Maximum relative differences between Least-squares estimated and true biases and ambiguities, using two distinctive methods of matrix inversion. The numbers of receivers and satellites are assumed to be the same. As the size of the network increases from $2 \times 2$ to $10 \times 10$, the dimension of the covariance matrix is getting higher, and thus, the direct inversion becomes more inaccurate, while the blockwise inversion remains highly accurate.

The variances and covariances of the state vectors from the least-squares estimates are described in Eq. (3.39).

A sequential ambiguity fixing with integer decorrelation has been performed in the process of Kalman filtering after the least-squares initialization. The decorrelated a posteriori float ambiguities of the Kalman filter can be obtained from Eq. (3.40), and the ambiguity to be fixed is chosen in each step that the cost function below reaches the minimum (see Henkel [1]). Since the standard deviation of the a posteriori estimate can not reveal the modeling errors in the state vectors fully, the real differences between the estimates and true ones are considered to make the modeling errors visible. The cost function combines the a posteriori statistical information $\sigma_{\hat{N}_{m,r}^{',k,+}}$ of the Kalman filter and the actual deviation between the a posteriori estimate $\hat{N}_{m,r}^{',k,+}$ and its rounded value $[\hat{N}_{m,r}^{',k,+}]$, and takes different

weights on the two components, i.e.

$$\min_{\hat{N}_{m,r}^{',k,+}} \left\{ w_1 \cdot |\hat{N}_{m,r}^{',k,+} - [\hat{N}_{m,r}^{',k,+}]| + w_2 \cdot \sigma_{\hat{N}_{m,r}^{',k,+}} \right\}, \tag{5.14}$$

where the coefficients have been set in this work to $w_1 = 2$ and $w_2 = 1$. Additionally, the ambiguity to be fixed shall also fulfill the following constraints on both components

$$\sigma_{\hat{N}_{m,r}^{',k,+}} \leq 0.1 \text{ cycles}, \quad \text{and} \quad |\hat{N}_{m,r}^{',k,+} - [\hat{N}_{m,r}^{',k,+}]| \leq 0.1 \text{ cycles}. \tag{5.15}$$

When one ambiguity is fixed within a step of Kalman filtering, the decorrelated and partially fixed ambiguity is transformed back to the correlated space and subtracted from the measurements, i.e.

$$\hat{N} = Z^{-1} \hat{\dot{N}}' = [\Lambda_1 \quad \Lambda_2] \begin{bmatrix} \hat{N}_A' \\ [\hat{N}_B'] \end{bmatrix}, \tag{5.16}$$

which simplifies the system of equations $\Psi = H\xi + AN + \varepsilon$ to

$$\begin{aligned} \Psi - A\Lambda_2 \left[ N_B' \right] &= H\xi + A\Lambda_1 N_A' + \varepsilon \\ &= [H \quad A\Lambda_1] \cdot \begin{bmatrix} \xi \\ N_A' \end{bmatrix}. \end{aligned} \tag{5.17}$$

It is noted that the ambiguity part of the state vector is then adapted to the decorrelated ones, and thus, the state transition matrix $\Phi$ will be adjusted correspondingly containing the integer transformation matrix $Z$.

Fig. 5.4 and 5.5 show the receiver and satellite phase bias estimates on L1 and L2. The vertical black lines indicate the ambiguity fixings. Totally 125 out of 128 ambiguities have been sequentially fixed. It is obvious that the fixing of the ambiguities improves the stability of the phase bias estimates substantially.

## 5.2 Estimation of Grid Ionospheric Vertical Delays and Satellite Code Biases

Chapter 4 presented two models for estimating grid ionospheric vertical delays and receiver and satellite code biases with a Kalman filter using measurements from a network of
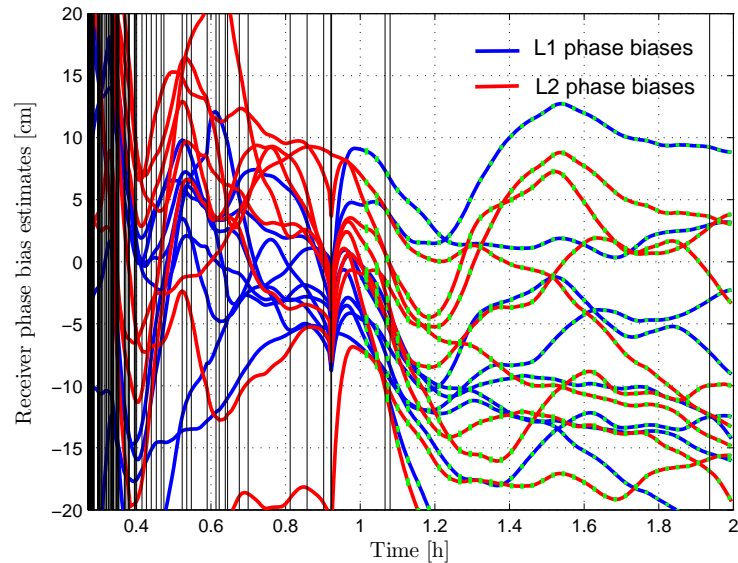
Fig. 5.4: Receiver phase bias estimates on frequencies L1 and L2 of SAPOS reference stations in Bavaria. The GPS measurements are taken on March 1, 2010, 8:00-10:00 UTC. The vertical black lines indicate the ambiguity fixings. The green error bars show the a posteriori standard deviations of the Kalman filter. The small magnitude of these error bars indicate a millimeter accuracy of the bias estimates. The fixing of the ambiguities substantially improves the stability of the bias estimates.

reference stations. The proposed estimation method of performing a weighted least-squares fitting is validated in this section with real GPS measurements from a network of Continuously Operating Reference Stations (CORS) [27] in USA.

A first validation has been made with real GPS data from 7 CORS stations (Tab. 5.1) in Vermont, estimating the grid ionospheric vertical delay and code biases with the optimization problem described in (4.15) for a single grid point. The vectors and matrices in (4.15) are explained further in Eq. (4.16) to (4.24).

Fig. 5.6 shows the map of the 7 CORS station. The GPS code and carrier phase measurements on frequencies L1 and L2 have been chosen. The ionospheric grid point has been set to a longitude of $\lambda = -71°$ and a latitude of $\phi = 43°$.

The following residuals of the ionospheric slant delays, which are obtained from the grid estimation of (4.15), are plotted in Fig. 5.7. Smaller residuals refer to the ionospheric pierce points that are closer to the grid point and have larger elevation angles, while larger residuals can be observed for the pierce points that are farer away. Consequently, these
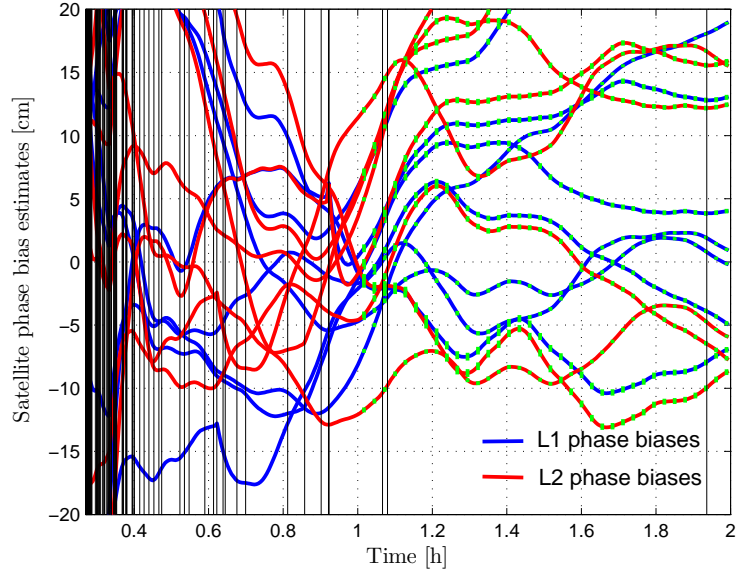
Fig. 5.5: Satellite phase bias estimates on L1 and L2 based on GPS measurements on March 1, 2010, 8:00-10:00 UTC from SAPOS reference stations in Bavaria. The vertical black lines indicate the ambiguity fixings. The green error bars show the a posteriori standard deviations of the Kalman filter. The small magnitude of these error bars indicate a millimeter accuracy of the bias estimates. The fixing of the ambiguities substantially improves the stability of the bias estimates.

Table 5.1: 7 CORS reference stations in Vermont, USA

| Station | Latitude | Longitude |
|---|---|---|
| Middlebury | 44.00° N | 73.15° W |
| Montpelier | 44.26° N | 72.58° W |
| Randolph Center | 43.94° N | 72.60° W |
| Danby | 43.35° N | 73.00° W |
| Bradford | 44.01° N | 72.11° W |
| Derby | 44.95° N | 72.16° W |
| Brighton | 44.82° N | 71.89° W |

ionospheric residuals also indicate irregularities in the ionosphere.

$$
r_I(t_n) = \begin{bmatrix} \hat{\tilde{I}}_1^1(t_n) \\ \vdots \\ \hat{\tilde{I}}_1^{K_1}(t_n) \\ \vdots \\ \hat{\tilde{I}}_R^{K_R}(t_n) \end{bmatrix} - \boldsymbol{M} \cdot \boldsymbol{H}_{I\dot{i}} \begin{bmatrix} i_0^{(l)}(t_n) \\ i_\phi^{(l)}(t_n) \\ i_\lambda^{(l)}(t_n) \\ \dot{i}_0^{(l)}(t_n) \\ \dot{i}_\phi^{(l)}(t_n) \\ \dot{i}_\lambda^{(l)}(t_n) \end{bmatrix} - \boldsymbol{H}_b \begin{bmatrix} b_{I_1} \\ \vdots \\ b_{I_R} \\ b_{I^2} \\ \vdots \\ b_{I^K} \end{bmatrix}. \tag{5.18}
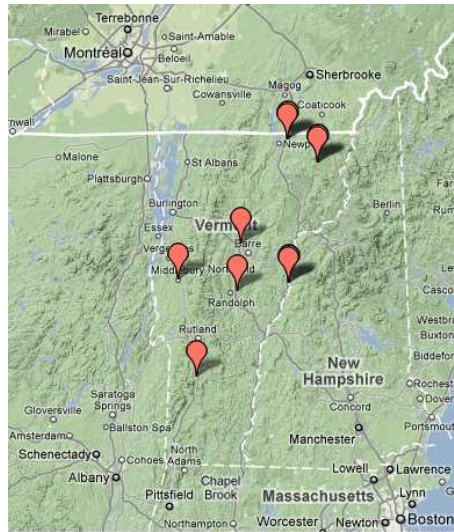$$

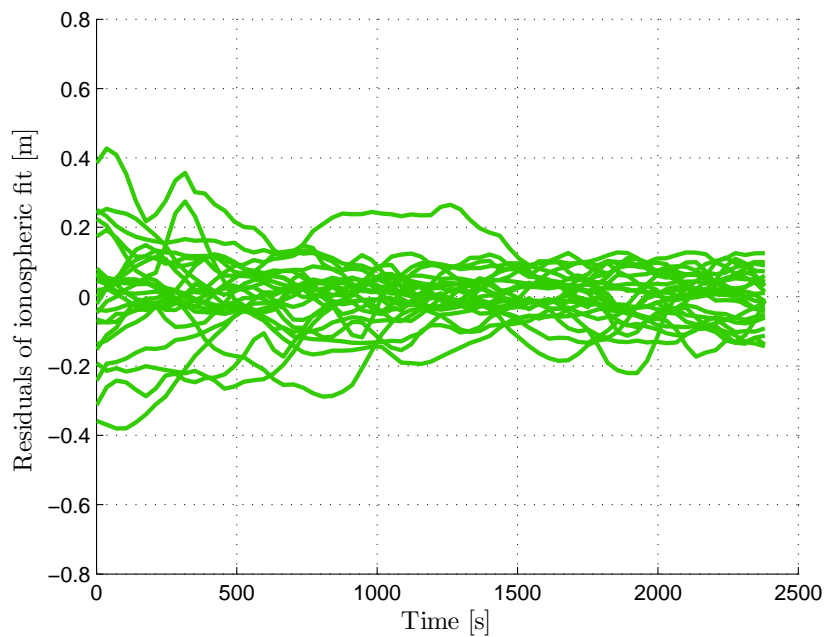Fig. 5.6: Map of the 7 CORS Stations in Vermont.



Fig. 5.7: Residuals of slant ionospheric delays: A least-squares fit has been used to estimate the vertical ionospheric delay for each grid point from the slant delays of the surrounding pierce points. In this work, a radius of 400 km boundary circle is chosen for the grid point.

A second validation used measurements from a larger network of 21 CORS reference stations on April 14, 2010 in USA. The locations of the stations (in Fig. 5.8) are listed in Tab. 5.2. The grid points where the ionospheric vertical delays are estimated have been

set to a 2.5° × 2.5° grid of longitude −82.5° to −77.5° and latitude 37.5° to 40.0°.

Table 5.2: Locations of the 21 CORS stations on April 14, 2010 in USA.

| Station | Latitude | Longitude | Station | Latitude | Longitude |
|---|---|---|---|---|---|
| Kenton, KY | 40.37° N | 83.37° W | Norwalk, OH | 41.10° N | 82.33° W |
| Louisville, KY | 38.16° N | 85.36° W | Wintersville, OH | 40.22° N | 80.43° W |
| Flemingsburg, KY | 38.25° N | 83.46° W | Pittsburgh, PA | 40.26° N | 79.57° W |
| Pikeville, KY | 37.48° N | 82.53° W | Schuylhill Haven, PA | 40.38° N | 76.09° W |
| Lebanon, OH | 39.25° N | 84.17° W | Greensburg, PA | 40.18° N | 79.30° W |
| Lisbon, OH | 40.46° N | 80.48° W | Harriman, TN | 39.54° N | 84.36° W |
| Mount Vernon, OH | 40.23° N | 82.30° W | Huntsville, TN | 36.24° N | 84.31° W |
| Albemarle, NC | 35.20° N | 80.12° W | Dunlap, TN | 35.23° N | 85.22° W |
| Jackson, NC | 36.24° N | 77.26° W | Nashville, TN | 36.10° N | 86.52° W |
| Monroe Township, NJ | 40.18° N | 74.28° W | Morgantown, WV | 39.38° N | 79.58° W |
| Logan, OH | 39.32° N | 82.26° W | | | |



Fig. 5.8: Map of the 21 CORS Stations in USA (listed in Tab. 5.2).

As the satellite and receiver code biases occur in the estimation of several ionospheric grid points, a joint estimation of the grid ionospheric vertical delays and code biases shall be considered.

Fig. 5.9 shows a simplified illustration of 4 ionospheric grid points, 6 receiver stations with each having a boundary circle and 8 visible satellites. The measurements at the

pierce points that are outside the boundary circles have been excluded from the system of equations, while some measurements are included in the overlapping area of multiple boundary circles. In the latter case, a linear combination of several grid point delays is performed

$$I_{\mathrm{v}}(\boldsymbol{x}_{\mathrm{IPP}_r^k}) = \sum_{l \in S_r^k} \alpha_r^{k,(l)} \cdot (i_0^{(l)} + i_\phi^{(l)}(\phi_r^k - \phi^{(l)}) + i_\lambda^{(l)}(\lambda_r^k - \lambda^{(l)})), \qquad (5.19)$$

where $S_r^k$ denotes the set of ionospheric grid points which satisfy the constraint

$$S_r^k = \{l \mid \|\boldsymbol{x}_{\mathrm{IGP}^{(l)}} - \boldsymbol{x}_{\mathrm{IPP}_r^k}\| < r_{\mathrm{bound}}\}, \qquad (5.20)$$

with the radius of the boundary circle $r_{\mathrm{bound}}$, which has been set to 400 km in this work. Different weighting coefficients $\alpha_r^{k,(l)}$ have been chosen by finding the minimum of the following equation, i.e.

$$\min_{\alpha_r^{k,(l)}} \sum_{l \in S_r^k} (\alpha_r^{k,(l)})^2 \cdot \frac{\|\boldsymbol{x}_{\mathrm{IPP}_r^k} - \boldsymbol{x}_{\mathrm{IGP}^{(l)}}\|}{\sin E_r^k}, \quad \text{s.t.} \sum_{l \in S_r^k} \alpha_r^{k,(l)} = 1. \qquad (5.21)$$

The ionospheric slant delays and their rates are modeled in the following equation for the joint estimation of grid ionospheric vertical delays and code biases, i.e.

$$\begin{bmatrix} \tilde{\boldsymbol{I}}_n \\ \dot{\tilde{\boldsymbol{I}}}_n \end{bmatrix} = \boldsymbol{H} \begin{bmatrix} \boldsymbol{i}_n \\ \dot{\boldsymbol{i}}_n \\ \boldsymbol{b}_{I_r} \\ \boldsymbol{b}_{I^k} \end{bmatrix} + \boldsymbol{\eta}, \qquad (5.22)$$

and thus, the ionospheric vertical delays at the grid points can be computed by a weighted least-squares fitting of the ionospheric slant delays from the surrounding pierce points, i.e.

$$\min_{[\boldsymbol{i}_n^{\mathrm{T}}, \dot{\boldsymbol{i}}_n^{\mathrm{T}}, \boldsymbol{b}_{I_r}^{\mathrm{T}}, \boldsymbol{b}_{I^k}^{\mathrm{T}}]^{\mathrm{T}}} \left\| \begin{bmatrix} \tilde{\boldsymbol{I}}_n \\ \dot{\tilde{\boldsymbol{I}}}_n \end{bmatrix} - \boldsymbol{H} \begin{bmatrix} \boldsymbol{i}_n \\ \dot{\boldsymbol{i}}_n \\ \boldsymbol{b}_{I_r} \\ \boldsymbol{b}_{I^k} \end{bmatrix} \right\|_{\boldsymbol{\Sigma}^{-1}}^2 . \qquad (5.23)$$

Let the notation of the ionospheric vertical delay at the grid point $(\lambda^{(l)}, \phi^{(l)})$ be the same as $i_0^{(l)}$ in Chapter 4, and also the latitudinal gradient $i_\phi^{(l)}$ and the longitudinal gradient $i_\lambda^{(l)}$.
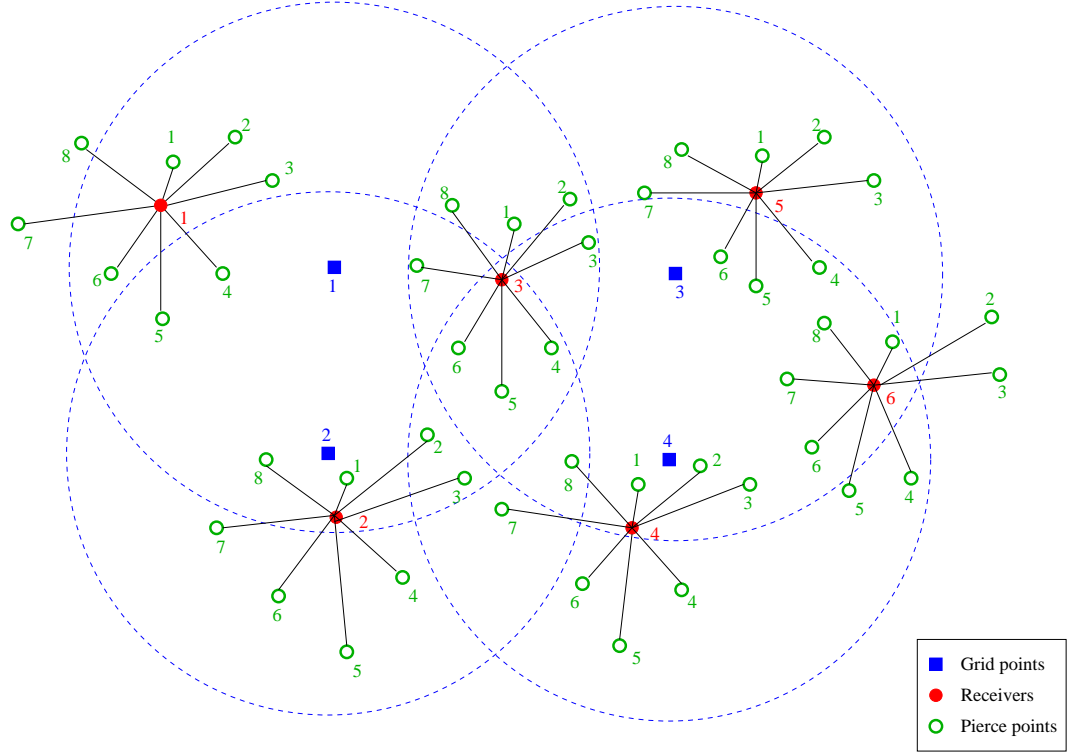
Fig. 5.9: A simplified illustration of 4 ionospheric grid points, 6 receiver stations with each having 8 visible satellites. The measurements at the pierce points which are outside the boundary circles have been excluded from the equations.

The measurement and state vectors are then given by

$$
\tilde{\boldsymbol{I}}_n \;=\; \begin{bmatrix} \tilde{I}_1^1(t_n) \\ \vdots \\ \tilde{I}_1^{K_1}(t_n) \\ \vdots \\ \tilde{I}_R^1(t_n) \\ \vdots \\ \tilde{I}_R^{K_R}(t_n) \end{bmatrix}, \quad
\dot{\tilde{\boldsymbol{I}}}_n = \begin{bmatrix} \dot{\tilde{I}}_1^1(t_n) \\ \vdots \\ \dot{\tilde{I}}_1^{K_1}(t_n) \\ \vdots \\ \dot{\tilde{I}}_R^1(t_n) \\ \vdots \\ \dot{\tilde{I}}_R^{K_R}(t_n) \end{bmatrix},
$$

$$
\boldsymbol{i}_n \;=\; \begin{bmatrix} i_0^{(1)}(t_n) \\ i_\phi^{(1)}(t_n) \\ i_\lambda^{(1)}(t_n) \\ \vdots \\ i_0^{(L)}(t_n) \\ i_\phi^{(L)}(t_n) \\ i_\lambda^{(L)}(t_n) \end{bmatrix}, \quad
\dot{\boldsymbol{i}}_n = \begin{bmatrix} \dot{i}_0^{(1)}(t_n) \\ \dot{i}_\phi^{(1)}(t_n) \\ \dot{i}_\lambda^{(1)}(t_n) \\ \vdots \\ \dot{i}_0^{(L)}(t_n) \\ \dot{i}_\phi^{(L)}(t_n) \\ \dot{i}_\lambda^{(L)}(t_n) \end{bmatrix}, \quad
\boldsymbol{b}_{\mathrm{I}_r} = \begin{bmatrix} b_{\mathrm{I}_1} \\ \vdots \\ b_{\mathrm{I}_R} \end{bmatrix}, \quad
\boldsymbol{b}_{\mathrm{I}^k} = \begin{bmatrix} b_{\mathrm{I}^1} \\ \vdots \\ b_{\mathrm{I}^K} \end{bmatrix}. \quad (5.24)
$$

The $\boldsymbol{H}$ matrix is described as

$$\boldsymbol{H} = \left[ \begin{array}{c} \mathbf{1}^{2\times 2} \otimes \left[ \begin{array}{cccc} \boldsymbol{A}_1^{(1)} \boldsymbol{M}_1 \boldsymbol{H}_{I_1}^{(1)} & \boldsymbol{A}_1^{(2)} \boldsymbol{M}_1 \boldsymbol{H}_{I_1}^{(2)} & \ldots & \boldsymbol{A}_1^{(L)} \boldsymbol{M}_1 \boldsymbol{H}_{I_1}^{(L)} \\ \vdots & & & \vdots \\ \boldsymbol{A}_R^{(1)} \boldsymbol{M}_R \boldsymbol{H}_{I_R}^{(1)} & \boldsymbol{A}_R^{(2)} \boldsymbol{M}_R \boldsymbol{H}_{I_R}^{(2)} & \ldots & \boldsymbol{A}_R^{(L)} \boldsymbol{M}_R \boldsymbol{H}_{I_R}^{(L)} \end{array} \right] & \boldsymbol{H}_{b_{I_r}} & \boldsymbol{H}_{b_{I^k}} \end{array} \right]. \tag{5.25}$$

The linear combination coefficients matrix $\boldsymbol{A}_r^{(l)}$ is computed in Appendix 7.2 by finding the minimization in Eq. (5.21) and has the structure of

$$\boldsymbol{A}_r^{(l)} = \left[ \begin{array}{ccc} \alpha_r^{1,(l)} & \ldots & \alpha_r^{1,(l)} \\ \vdots & \ddots & \vdots \\ \alpha_r^{K_r,(l)} & \ldots & \alpha_r^{K_r,(l)} \end{array} \right]. \tag{5.26}$$

The mapping matrix from ionospheric vertical delays to slant delays is given by

$$\boldsymbol{M}_r = \left[ \begin{array}{ccc} m_{\mathrm{I}}(E_r^1) & & \\ & \ddots & \\ & & m_{\mathrm{I}}(E_r^{K_r}) \end{array} \right], \tag{5.27}$$

with $m_{\mathrm{I}}(E_r^k)$ defined in Eq. (4.3).

The interpolation matrix is obtained from the least-squares fitting method as

$$\boldsymbol{H}_{I_r}^{(l)} = \left[ \begin{array}{ccc} 1 & \phi_r^1 - \phi^{(l)} & \lambda_r^1 - \lambda^{(l)} \\ \vdots & \vdots & \vdots \\ 1 & \phi_r^{K_r} - \phi^{(l)} & \lambda_r^{K_r} - \lambda^{(l)} \end{array} \right]. \tag{5.28}$$

The receiver code bias coefficient matrix is given by

$$\boldsymbol{H}_{b_{I_r}} = \left[ \begin{array}{cccc} \mathbf{1}^{K_1\times 1} & & & \\ & \mathbf{1}^{K_2\times 1} & & \\ & & \ddots & \\ & & & \mathbf{1}^{K_R\times 1} \end{array} \right], \tag{5.29}$$

and the satellite code bias coefficient matrix is written as

$$\boldsymbol{H}_{b_I^k} \left[ \sum_{r'=1}^{r-1} K_{r'} + k, j \right] = \left\{ \begin{array}{ll} 1, & \text{if} \quad j = \mu(k, \mathcal{S}_r). \\ 0, & \text{elsewhere.} \end{array} \right. , \tag{5.30}$$

where $\mu(k, \mathcal{S}_r)$ describes the position of the $k$-th satellite of subset

$$\mathcal{S}_r \triangleq \{k_{\mathcal{S}_r}^1, \ldots, k_{\mathcal{S}_r}^{K_r}\} \tag{5.31}$$

within the union set

$$\mathcal{S} = \{\mathcal{S}_1 \cup \mathcal{S}_2 \cup \ldots \cup \mathcal{S}_R\}, \tag{5.32}$$

which contains all satellites that are visible from at least one reference station.

Fig. 5.10 shows the satellite bias estimates $\hat{b}_I^k$ using GPS L1 and L2 code and carrier phase measurements from 21 CORS stations in USA (listed in Tab. 5.2). The red error bars show the a posteriori standard deviations of the Kalman filter based bias estimates which are in the order of magnitude of a few millimeters. The stability of the bias estimates varies between 10 cm/ hour and 20 cm/ hour.
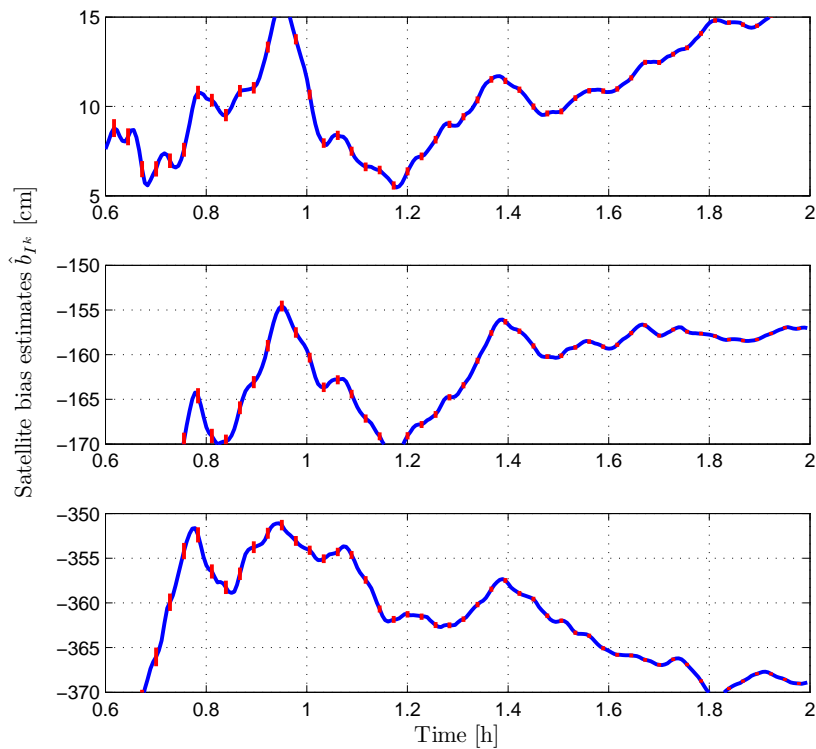


Fig. 5.10: Ionospheric satellite bias estimates $\hat{b}_I^k$ using GPS L1 and L2 code and carrier phase measurements from 21 CORS stations in USA (listed in Tab. 5.2). The red error bars show the a posteriori standard deviations of the Kalman filter based bias estimates which are in the order of magnitude of a few millimeters. The stability of the bias estimates varies between 10 cm/ hour and 20 cm/ hour.

# 6 Conclusion

In this work, the receiver and satellite biases on multiple frequencies were estimated with a Kalman filter and a network of reference stations. The estimation methods were validated with simulated measurements from the global network of Galileo Sensor Stations as well as with real data from a few stations of CORS network in USA as well as from the Bavarian reference stations of SAPOS network. Integer ambiguity resolution is performed during the estimation process, using the bootstrapped estimator which benefits from a higher success rate than instantaneous rounding. Moreover, the grid ionospheric vertical delays were estimated jointly with the satellite and receiver code biases using a Kalman filter and a least-squares fitting.

A set of parameter mappings has been introduced to remove the rank deficiency of the system of equations. Firstly, the receiver and satellite code biases on two frequencies were mapped into ranges and ionospheric delays. Secondly, the satellite phase biases of one satellite were absorbed by the receiver phase biases. A subset of integer ambiguities was combined with phase biases using classical Gaussian elimination. The receiver and satellite phase biases were then estimated by Kalman filtering. Along with the Kalman filtering, integer ambiguity resolution was performed in such a way that it decorrelated the float ones and then sequentially fixed them. The pull-in region of the integer estimator has been included to visualize the integer bootstrapping method. Several simulation results showed that the benefit of ambiguity fixing resulted in a millimeter-level accuracy after thousand epochs, the redundancy of a third frequency enabled a much earlier fixing and thus leaded to a higher accuracy. A second Kalman filter estimated the satellite positions as well as the combined bias/clock offsets.

Moreover, the receiver and satellite phase biases have been estimated with GPS measurements from the SAPOS network. A 1 mm accuracy and a stability between 10 cm/hour and 20 cm/hour have been observed in the bias estimates. It has also been shown that the fixing of the ambiguities improved the stability of the phase bias estimates substantially.

Since some code biases have been mapped into the ionospheric delays, they were estimated

together with GIVDs using the model of weighted least-squares fittings from different sets of surrounding pierce points, which were in the boundary circles centered at the grid points. The least-squares fitting took the vertical delay, the longitudinal and latitudinal gradients of the slant delay at the grid point into accounts, and used the measurements from nearby pierce points to perform a fitting plane for the grid point. Simulation results have been presented with measurements simulated from a network of EGNOS RIMS stations in Europe, and millimeter-level accuracies on bias and vertical delay estimates have been achieved. GPS measurements from the CORS network in USA have been used to validate the estimation method.

The next step will be the estimation of the geometry-dependent code bias $b_{g_r}$ and $b_{g^k}$ with an improved orbital model, as well as the introduce of a background model to improve the accuracies of the bias estimates. The increase of the network will also require more efficient algorithms as the state vector includes several thousand parameters which results in a posteriori covariance matrices of several million elements. The completely reduction would be advised by considering the structure of the state transition of geometry matrices.

# 7 Appendix

## 7.1 Calculation of the Process Noise Covariances for Range, Range Rate, and Range Acceleration

A more accurate model in Fig. 7.1 for the change in range is to introduce the second derivative of the range in the estimation, i.e. range acceleration, which is assumed to follow a random walk process.
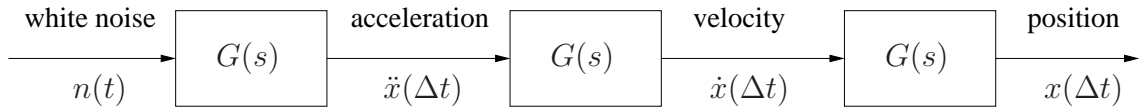


Fig. 7.1: Random walk model on range acceleration.

The transfer functions describe the integration, i.e.

$$
\begin{aligned}
G_1(s) &= G(s) = \frac{1}{s} \quad \xrightarrow{\mathfrak{L}^{-1}} \quad g_1(t) = u(t) \\
G_2(s) &= G(s)^2 = \frac{1}{s^2} \quad \xrightarrow{\mathfrak{L}^{-1}} \quad g_2(t) = t \cdot u(t) \\
G_3(s) &= G(s)^3 = \frac{1}{s^3} \quad \xrightarrow{\mathfrak{L}^{-1}} \quad g_3(t) = \frac{1}{2}t^2 \cdot u(t)
\end{aligned}
\tag{7.1}
$$

The noise variances and covariances can be computed as

$$
\begin{aligned}
\mathrm{E}\{\ddot{x}(\Delta t)\ddot{x}(\Delta t)\} &= \mathrm{E}\{(n(t) * g_1(t)) \cdot (n(t) * g_1(t))\} \\
&= \mathrm{E}\left\{\int_0^{\Delta t} n(w)dw \cdot \int_0^{\Delta t} n(v)dv\right\} \\
&= \mathrm{E}\left\{\int_0^{\Delta t}\int_0^{\Delta t} n(w)n(v) \cdot \delta(w-v)dwdv\right\} \\
&= \int_0^{\Delta t}\int_0^{\Delta t} \mathrm{E}\{n^2(w)\} \cdot \delta(w-v)dwdv \\
&= \int_0^{\Delta t}\int_0^{\Delta t} S_p \cdot \delta(w-v)dwdv = S_p \cdot \Delta t,
\end{aligned}
\tag{7.2}
$$

$$
\begin{aligned}
\mathrm{E}\{\dot{x}(\Delta t)\ddot{x}(\Delta t)\} &= \mathrm{E}\{(n(t) * g_2(t)) \cdot (n(t) * g_1(t))\} \\
&= \mathrm{E}\left\{\int_0^{\Delta t} n(t-w)w\,dw \cdot \int_0^{\Delta t} n(\tau)d\tau\right\} \\
&= \mathrm{E}\left\{\int_0^{\Delta t}\int_0^{\Delta t} n(t-w)n(\tau) \cdot w \cdot \delta(t-w-\tau)dwd\tau\right\} \\
&= \int_0^{\Delta t}\int_0^{\Delta t} \mathrm{E}\{n^2(w)\} \cdot w \cdot \delta(t-w-\tau)dwd\tau \\
&= S_p \cdot \frac{\Delta t^2}{2},
\end{aligned}
\tag{7.3}
$$

$$
\begin{aligned}
\mathrm{E}\{x(\Delta t)\ddot{x}(\Delta t)\} &= \mathrm{E}\{(n(t) * g_3(t)) \cdot (n(t) * g_1(t))\} \\
&= \mathrm{E}\left\{\int_0^{\Delta t} n(t-w) \cdot \frac{1}{2}w^2\,dw \cdot \int_0^{\Delta t} n(\tau)d\tau\right\} \\
&= \mathrm{E}\left\{\int_0^{\Delta t}\int_0^{\Delta t} n(t-w)n(\tau) \cdot \frac{1}{2}w^2 \cdot \delta(t-w-\tau)dwd\tau\right\} \\
&= \int_0^{\Delta t}\int_0^{\Delta t} \mathrm{E}\{n^2(w)\} \cdot \frac{1}{2}w^2 \cdot \delta(t-w-\tau)dwd\tau \\
&= \frac{1}{6} S_p \cdot \Delta t^3,
\end{aligned}
\tag{7.4}
$$

$$
\begin{aligned}
\mathrm{E}\{\dot{x}(\Delta t)\dot{x}(\Delta t)\} &= \mathrm{E}\{(n(t) * g_2(t)) \cdot (n(t) * g_2(t))\} \\
&= \mathrm{E}\left\{\int_0^{\Delta t} n(t-w)w\,dw \cdot \int_0^{\Delta t} n(t-v)v\,dv\right\} \\
&= \mathrm{E}\left\{\int_0^{\Delta t}\int_0^{\Delta t} n(t-w)n(t-v) \cdot w \cdot v \cdot \delta((t-w)-(t-v))dwdv\right\} \\
&= \int_0^{\Delta t}\int_0^{\Delta t} \mathrm{E}\{n^2(t-w)\} \cdot w \cdot v \cdot \delta(v-w)dwdv \\
&= S_p \cdot \frac{\Delta t^3}{3},
\end{aligned}
\tag{7.5}
$$

$$
\begin{aligned}
\mathrm{E}\{x(\Delta t)\dot{x}(\Delta t)\} &= \mathrm{E}\{(n(t) * g_3(t)) \cdot (n(t) * g_2(t))\} \\
&= \mathrm{E}\left\{\int_0^{\Delta t} n(t-w) \cdot \frac{1}{2}w^2\,dw \cdot \int_0^{\Delta t} n(t-v)v\,dv\right\} \\
&= \mathrm{E}\left\{\int_0^{\Delta t}\int_0^{\Delta t} n(t-w)n(t-v) \cdot \frac{1}{2}w^2 \cdot v \cdot \delta((t-w)-(t-v))dwdv\right\} \\
&= \int_0^{\Delta t}\int_0^{\Delta t} \mathrm{E}\{n^2(t-w)\} \cdot \frac{1}{2}w^2 \cdot v \cdot \delta(v-w)dwdv \\
&= \frac{1}{8} S_p \cdot \Delta t^4.
\end{aligned}
\tag{7.6}
$$

$$
\begin{aligned}
\mathrm{E}\{x(\Delta t)x(\Delta t)\} &= \mathrm{E}\{(n(t) * g_3(t)) \cdot (n(t) * g_3(t))\} \\
&= \mathrm{E}\left\{ \int_0^{\Delta t} n(t-w) \cdot \frac{1}{2} w^2 dw \cdot \int_0^{\Delta t} n(t-v) \cdot \frac{1}{2} v^2 dv \right\} \\
&= \mathrm{E}\left\{ \int_0^{\Delta t} \int_0^{\Delta t} n(t-w) n(t-v) \cdot \frac{1}{2} w^2 \cdot \frac{1}{2} v^2 \cdot \delta((t-w)-(t-v)) dw dv \right\} \\
&= \int_0^{\Delta t} \int_0^{\Delta t} \mathrm{E}\{n^2(t-w)\} \cdot \frac{1}{2} w^2 \cdot \frac{1}{2} v^2 \cdot \delta(v-w) dw dv \\
&= \frac{1}{20} S_p \cdot \Delta t^5.
\end{aligned}
\tag{7.7}
$$

Therefore, the covariance matrix for range, range rate, and the second derivatives of range is given by

$$
\mathbf{\Sigma}_{\mathrm{Q}, \tilde{g} \dot{\tilde{g}} \ddot{\tilde{g}}} = S_p \cdot \Delta t \cdot
\begin{bmatrix}
\frac{1}{20} \Delta t^4 & \frac{1}{8} \Delta t^3 & \frac{1}{6} \Delta t^2 \\
\frac{1}{8} \Delta t^3 & \frac{1}{3} \Delta t^2 & \frac{1}{2} \Delta t \\
\frac{1}{6} \Delta t^2 & \frac{1}{2} \Delta t & 1
\end{bmatrix}
\otimes \mathbf{1}^{s \times s}.
\tag{7.8}
$$

## 7.2 Calculation of the Linear Combination Coefficient Matrix

Since some measurements at the pierce points are included in multiple bounding circles from the grid points, at which the vertical delays and the code biases are estimated jointly, a linear combination of grid points for one pierce points is performed and different weighting coefficients are introdwced, i.e.

$$I_{\mathrm{v}}(\boldsymbol{x}_{\mathrm{IPP}_r^k}) = \sum_{l \in S_r^k} \alpha_r^{k,(l)} \cdot (i_0^{(l)} + i_\phi^{(l)}(\phi_r^k - \phi^{(l)}) + i_\lambda^{(l)}(\lambda_r^k - \lambda^{(l)})), \qquad (7.9)$$

where $S_r^k$ denotes the set of ionospheric grid points which satisfy the constraint

$$S_r^k = \{l \mid \|\boldsymbol{x}_{\mathrm{IGP}^{(l)}} - \boldsymbol{x}_{\mathrm{IPP}_r^k}\| < r_{\mathrm{bound}}\}, \qquad (7.10)$$

with the radius of the boundary circle $r_{\mathrm{bound}}$.

The coefficients $\alpha_r^{k,(l)}$ are chosen such that

$$\min_{\alpha_r^{k,(l)}} \sum_{l \in S_r^k} (\alpha_r^{k,(l)})^2 \cdot \frac{\|\boldsymbol{x}_{\mathrm{IPP}_r^k} - \boldsymbol{x}_{\mathrm{IGP}^{(l)}}\|}{\sin E_r^k} \triangleq \min_{\alpha_r^{k,(l)}} \sum_{l \in S_r^k} (\alpha_r^{k,(l)})^2 (\sigma_r^{k,(l)})^{-2}, \qquad (7.11)$$

with the constraints

$$\sum_{l \in S_r^k} \alpha_r^{k,(l)} = 1. \qquad (7.12)$$

The optimization in Eq. (7.11) is performed for every pierce point $\mathrm{IPP}_r^k$. For simplicity, the index $r$ and $k$ are omitted in the following, and the notations $\alpha^{(l)}$, $\sigma^{(l)}$ indicate $\alpha_r^{k,(l)}$ and $\sigma_r^{k,(l)}$.

Assume that the elements in the set $S$ are $l_1, \ldots, l_M$, i.e.

$$S = \{l \mid \|\boldsymbol{x}_{\mathrm{IGP}^{(l)}} - \boldsymbol{x}_{\mathrm{IPP}}\| < r_{\mathrm{bound}}\} = \{l_1, \ldots, l_M\}, \quad \text{and} \sum_{l=l_1}^{l_M} \alpha^{(l)} = 1, \qquad (7.13)$$

Eq. (7.11) becomes

$$\sum_{l=l_1}^{l_M} (\alpha^{(l)})^2 (\sigma^{(l)})^{-2} = (1 - \sum_{l=l_2}^{l_M} \alpha^{(l)})^2 (\sigma^{(l_1)})^{-2} + \sum_{l=l_2}^{l_M} (\alpha^{(l)})^2 (\sigma^{(l)})^{-2}. \qquad (7.14)$$

Setting the derivatives to zero

$$\begin{bmatrix} \frac{\partial}{\partial \alpha^{(l_2)}} \left( (1 - \sum_{l=l_2}^{l_M} \alpha^{(l)})^2 (\sigma^{(l_1)})^{-2} + \sum_{l=l_2}^{l_M} (\alpha^{(l)})^2 (\sigma^{(l)})^{-2} \right) \\ \frac{\partial}{\partial \alpha^{(l_3)}} \left( (1 - \sum_{l=l_2}^{l_M} \alpha^{(l)})^2 (\sigma^{(l_1)})^{-2} + \sum_{l=l_2}^{l_M} (\alpha^{(l)})^2 (\sigma^{(l)})^{-2} \right) \\ \vdots \\ \frac{\partial}{\partial \alpha^{(l_M)}} \left( (1 - \sum_{l=l_2}^{l_M} \alpha^{(l)})^2 (\sigma^{(l_1)})^{-2} + \sum_{l=l_2}^{l_M} (\alpha^{(l)})^2 (\sigma^{(l)})^{-2} \right) \end{bmatrix} = \begin{bmatrix} 0 \\ 0 \\ \vdots \\ 0 \end{bmatrix} \qquad (7.15)$$

yields

$$
\begin{bmatrix}
2 \cdot (1 - \sum_{l=l_2}^{l_M} \alpha^{(l)}) \cdot (-\sigma^{(l_1)})^{-2} + 2\alpha^{(l_2)}(\sigma^{(l_2)})^{-2} \\
2 \cdot (1 - \sum_{l=l_2}^{l_M} \alpha^{(l)}) \cdot (-\sigma^{(l_1)})^{-2} + 2\alpha^{(l_3)}(\sigma^{(l_3)})^{-2} \\
\vdots \\
2 \cdot (1 - \sum_{l=l_2}^{l_M} \alpha^{(l)}) \cdot (-\sigma^{(l_1)})^{-2} + 2\alpha^{(l_M)}(\sigma^{(l_M)})^{-2}
\end{bmatrix}
=
\begin{bmatrix}
0 \\ 0 \\ \vdots \\ 0
\end{bmatrix},
\tag{7.16}
$$

and adding $\alpha^{(l_1)}$ into the vector yields

$$
\boldsymbol{\Gamma} \cdot
\begin{bmatrix}
\alpha^{(l_1)} \\
\alpha^{(l_2)} \\
\vdots \\
\alpha^{(l_M)}
\end{bmatrix}
=
\begin{bmatrix}
1 \\
2(\sigma^{(l_1)})^{-2} \\
2(\sigma^{(l_1)})^{-2} \\
\vdots \\
2(\sigma^{(l_1)})^{-2}
\end{bmatrix},
\tag{7.17}
$$

with

$$
\boldsymbol{\Gamma} =
\begin{bmatrix}
1 & 1 & 1 & \dots & 1 \\
0 & 2\left((\sigma^{(l_1)})^{-2} + (\sigma^{(l_2)})^{-2}\right) & 2(\sigma^{(l_1)})^{-2} & \dots & 2(\sigma^{(l_1)})^{-2} \\
0 & 2(\sigma^{(l_1)})^{-2} & 2\left((\sigma^{(l_1)})^{-2} + (\sigma^{(l_3)})^{-2}\right) & \dots & 2(\sigma^{(l_1)})^{-2} \\
\vdots & \vdots & \vdots & \ddots & 2(\sigma^{(l_1)})^{-2} \\
0 & 2(\sigma^{(l_1)})^{-2} & 2(\sigma^{(l_1)})^{-2} & \dots & 2\left((\sigma^{(l_1)})^{-2} + (\sigma^{(l_M)})^{-2}\right)
\end{bmatrix}
\tag{7.18}
$$

Thus, the coefficients $\alpha^{(l)}$ are solved as

$$
\begin{bmatrix}
\alpha^{(l_1)} \\
\alpha^{(l_2)} \\
\vdots \\
\alpha^{(l_M)}
\end{bmatrix}
= \boldsymbol{\Gamma}^{-1} \cdot
\begin{bmatrix}
1 \\
2(\sigma^{(l_1)})^{-2} \\
2(\sigma^{(l_1)})^{-2} \\
\vdots \\
2(\sigma^{(l_1)})^{-2}
\end{bmatrix}.
\tag{7.19}
$$

Consequently, the linear coefficient matrix $\boldsymbol{A}$ is obtained as

$$
\boldsymbol{A}_r^{(l)} =
\begin{bmatrix}
\alpha_r^{1,(l)} & \dots & \alpha_r^{1,(l)} \\
\vdots & \ddots & \vdots \\
\alpha_r^{K_r,(l)} & \dots & \alpha_r^{K_r,(l)}
\end{bmatrix}.
\tag{7.20}
$$

# Bibliography

[1] P. Henkel, "Reliable Carrier Phase Positioning with Multiple Frequencies", *PhD thesis*, submitted at Technische Universität München, 184 pp., **2010**.

[2] C. Günther, *Satellite Navigation - Lecture Notes*, Technische Universität München, **2009**.

[3] C. Günther, *Differential Navigation - Lecture Notes*, Technische Universität München, **2009**.

[4] J.F. Zumberge, M.B. Heflin, D.C. Jefferson, M.M. Watkins, and F.H. Webb, "Precise point positioning for the efficient and robust analysis of GPS data from large networks", *J. Geophys. Res.*, vol. 102, no. b3, pp. 5005-5017, Mar. **1997**.

[5] P. Henkel, C. Günther, "Joint L/C Band Code and Carrier Phase Linear Combinations for Galileo", *J. of Nav. and Obs.*, Article ID 651437, 8 pp., Jan. **2008**.

[6] P. Henkel, Z. Wen and C. Günther, "Estimation of phase and code biases on multiple frequencies with a Kalman filter", *Proc. of 4-th Workshop on GNSS Signals and Signal Processing*, Oberpfaffenhofen, Germany, Dec. **2009**.

[7] P. Henkel, Z. Wen and C. Günther, "Estimation of satellite and receiver biases on multiple Galileo frequencies with a Kalman filter", *Proc. of ION Int. Techn. Meet. (ITM)*, San Diego, USA, **2010**.

[8] R. Schmid, M. Rothacher, D. Thaller, and P. Steigenberger, "Absolute phase center corrections of satellite and receiver antennas: Impact on global GPS solutions and estimation of azimuthal phase center variations of the satellite antenna", *GPS Solutions*, vol. 9, no. 4, pp. 283-293, Nov. **2005**.

[9] M. Ge, G. Gendt, M. Rothacher, C. Shi and J. Liu, "Resolution of GPS carrier-phase ambiguities in Precise Point Positioning (PPP) with daily observations", *J. of Geodesy*, Springer, pp. 389-399, Oct. **2007**.

[10] M. Gabor and S. Nerem, "Satellite-satellite single difference phase calibration as applied to ambiguity resolution", *J. of the Ins. of Nav.*, vol. 49, no. 4, pp. 223-242, **2002**.

[11] J. Betz, "Binary Offset Carrier Modulations for Radionavigation", *Navigation*, vol. 48, no. 4, pp. 227-246, **2002**.

[12] P. Henkel, V. Gomez and C. Günther, "Modified LAMBDA for absolute carrier phase positioning in the presence of biases", *Proc. of Int. Tech. Meet. (ITM)*, Anaheim, USA, pp. 642-651, Jan. **2009**.

[13] G. Wübbena, "GPS carrier phases and clock modeling", Lecture notes in earth sciences: *GPS techniques applied to geodesy and surveying*, vol. 19, pp. 381-392, DOI: 10.1007/BFb0011350, **1988**.

[14] G.H. Golub, C.F. Van Loan, *Matrix Computations (3rd ed.)*, Johns Hopkins, ISBN 978-0-8018-5414-9, **1996**.

[15] R. Brown and P. Hwang, *Introduction to random signals and applied Kalman filtering*, 3rd edition, John Wiley & Sons, New York, **1997**.

[16] P.J.G. Teunissen, "Success probability of integer GPS ambiguity rounding and bootstrapping", *J. of Geodesy*, vol. 72, pp. 606-612, Springer, **1998**.

[17] G. Blewitt, "Carrier-phase ambiguity resolution for the Global Positioning System applied to geodetic baselines up to 2000 km", *J. Geophys. Res.*, vol. 94, pp. 10187-10203, **1989**.

[18] P.J.G. Teunissen, "A new method for fast carrier phase ambiguity estimation", *Proc. of IEEE Pos., Loc. and Nav. Symp. (PLANS)*, pp. 562-573, Apr. **1994**.

[19] P.J.G. Teunissen, "Integer estimation in the presence of biases", *J. of Geodesy*, vol. 75, pp. 399-407, Springer, **2001**.

[20] P.J.G. Teunissen, "GNSS Ambiguity Bootstrapping: Theory and Application", *Proc. of Int. Symp. on Kin. Syst. in Geod., Geom, and Nav.*, Banff, Canada, pp. 246-254, **2001**.

[21] P.J.G. Teunissen, "The least-squares ambiguity decorrelation adjustment: a method for fast GPS ambiguity estimation", *J. of Geodesy*, vol. 70, pp. 65-82, **1995**.

[22] A.E. Niell, "Global Mapping Functions for the Atmosphere Delay at Radio Wavelengths", *J. Geophys. Res.*, vol. 101, pp. 3227-3246, **1996**.

[23] Y.C. Chao, Y.J. Tsai, J. Evans, C. Kee, T. Walter, P.K. Enge, J.D. Powell, B.W. Parkinson, "Generation of ionospheric correction and confidence estimates for WAAS", *52nd Ann. Meet. of the Ins. of Nav.*, pp. 139-146, Jun. **1996**.

[24] R.S. Conker, M. Bakry El-Arini, T.W. Albertson, J.A. Klobuchar, P.H. Doherty, "Description and Assessment of Real-Time Algorithms to Estimate the Ionospheric Error Bounds for WAAS", *J. of the Ins. of Nav.*, vol. 44, pp. 77-87, **1997**.

[25] B. Arbesser-Rastburg, "Ionospheric corrections for satellite navigation using EGNOS", *Proc. of XXVII-th URSI General Assembly*, Maastricht, **2002**.

[26] "SAPOS Bayern - Referenzstationen" Online: http://www.vermessung.bayern.de/sapos/saposreferenzstationen.html, accessed on: 01.03.2010

[27] "National Geodetic Survey - CORS" Datas available online: ftp://www.ngs.noaa.gov/cors/rinex/2010/, accessed on: 14.04.2010